UNSTEADY HETEROGENEOUS QUASI 1-D COMBUSTION MODEL FOR AP-HTPB BASED COMPOSITE PROPELLANTS

A THESIS

submitted by

VISHAL WADHAI

for the award of the degree

of

MASTER OF SCIENCE

(by Research)

DEPARTMENT OF MECHANICAL ENGINEERING
INDIAN INSTITUTE OF TECHNOLOGY MADRAS.

July 2018

Dedicated to .....

Aai & Baba

THESIS CERTIFICATE

This is to certify that the thesis titled **UNSTEADY HETEROGENEOUS QUASI 1-D COMBUSTION MODEL FOR AP-HTPB BASED COMPOSITE PROPELLANTS** , submitted by **Vishal Wadhai**, to the Indian Institute of Technology, Madras, for the award of the degree of **Master of Science (by Research)**, is a bona fide record of the research work done by him under my supervision. The contents of this thesis, in full or in parts, have not been submitted to any other Institute or University for the award of any degree or diploma.

Research Guide
Dr. Varunkumar S.
Dept. of Mechanical Engineering
IIT-Madras, 600 036

Place: Chennai

Date: 29 July, 2018

ACKNOWLEDGEMENTS

I would like to thank my thesis adviser Dr. Varunkumar S. for giving me the opportunity to work under his valuable guidance. I am grateful to receive life cherishing notes from him regarding the various aspects of carrying out research - especially reading and writing skills. I am indebted to the Head of the department, Prof. N. Ramesh Babu and my Graduate Test Committee members, Prof. P. A. Ramakrishna and Dr. T. N. C. Anand for their valuable comments and suggestions on the research work. I extend my gratitude to the personnel of High Performance Computing Environment (HPCE) facility at IIT Madras for providing access to the computational facility. I am truly grateful to my lab mates Jagan, Zaved, Ajey, Mughees and Kalyani for providing the thoughtful environment and for their contributions towards my thesis. I am also thankful to Priyanka, Shirin and other members of TDCE lab for their valuable support during my research work. I am especially thankful to my friends Arvind I. B., Akaash, Shubham and Vidit for being there and making my stay at IIT, Madras memorable. My heartfelt thank goes to my father and my sister Vaishnavi for their great belief in my capabilities and their moral support.

ABSTRACT

KEYWORDS: acoustic instability; AP/HTPB composite propellants; frequency response; serial burning approach; binder melt dynamics; linear instability; DC shift

This thesis deals with a theoretical framework to predict longitudinal mode acoustic instability in tactical missile solid rocket motors (SRMs). The work reported here consists of the following two principal parts - (1) *unsteady heterogeneous quasi-one-dimensional (UHeQu1-D)* model for predicting the pressure-coupled response (R_p) of low smoke AP/HTPB composite solid propellants (Chapters 2 and 3) and (2) CFD framework coupling the *UHeQu1-D* model to port gas dynamics to predict unsteady flow in a canonical tactical missile rocket (Chapter 4). For the first part, the *HeQu1-D* model for steady combustion of AP/HTPB propellants is extended to the unsteady regime by linear perturbation analysis. Using the serial burning approach, the frequency response of a multi-modal propellant is expressed in terms of that of binder-matrix coated AP particles constituting the statistical particle path. Following the same sequence as in *HeQu1-D*, first closed-form expression is obtained for the frequency response of limiting cases, namely, mono-propellant (pure AP) and homogeneous (fine-AP/HTPB) limits. Then, by perturbation analysis of *quasi 1-D* burn rate model for binder-matrix coated AP particle, closed-form expression is obtained for the frequency response. An important conclusion from the analytical expression is that except for the parameters A_c (heat flux amplification factor) and ϕ_c (phase difference), which quantify the unsteady conduction in condensed phase, all other parameters in the expression for frequency response are steady state variables - this result goes beyond all earlier ones where only the $R_p \to n$ as $f \to 0$ was explicitly imposed, where n is burn rate index and f is frequency. For the binder-matrix coated AP particles (including the limiting cases), the peak response is of the same order as n and occurs at a frequency corresponding to the conduction time scale ($\alpha/\bar{r}^2$, α is thermal diffusivity and $\bar{r}$ is steady-state burn rate). That is, when expressed as R_p/n vs $f_s = f\alpha/\bar{r}^2$ (non-dimensional frequency), the peak

magnitude will be $\mathcal{O}(1)$ and will occur close to $f_s = 1$. From this conclusion follows the well-known result from the literature that the frequency response of conventional propellants (only AP/HTPB) is of the same order as the burn rate index (n). Following this the effects of AP particle size distribution, solid loading, mean pressure and initial temperature on the propellant response are elucidated. Analysis done by varying fractions of particle sizes reveals mainly that frequency of peak response depends on particle size distribution and propellants containing a large fraction of coarse particles burn with higher frequency response. The decrease in solid loading which makes the propellant burn slower is found to increase the propellant response. The increase in mean pressure and initial temperature have been shown to decrease the magnitude of peak frequency response of the propellant - another well-known result from literature. Similar conclusions apply to propellants with burn rate enhancing catalysts (carbon black, for instance).

With $R_{p,max} \sim n$ and given that $n < 1$, tactical SRMs using conventional propellants will be stable. But earlier experimental results obtained from motor firings indicate that propellant R_p values can be as high as 3 (one order more than n) and a distinguishing feature of such propellants is the use of burn rate inhibitors like $SrCO_3$. Such inhibiting agents are known to cause binder-melt flow, which in fact is the mechanism by which the burn rate index is lowered to 0.3, while diffusion effects alone can explain index reduction only up to 0.4. By extending the *UHeQu1-D* framework to account for thermo-chemical and heat flux shielding effects of binder-melt flow, the increase in R_p is explained. Fluctuation in binder-melt cover was introduced as a possible mechanism of R_p enhancement and as a principal contributor to instability in tactical SRMs. The inclusion of this effect reverses the pressure dependence of R_p - it increases with increase in pressure and is consistent with the fact that the SRMs are more prone to instability at higher pressures (beyond the effect of reduced damping at higher pressures). This result is a likely explanation for some conflicting observations on the pressure dependence of R_p found in the literature.

The second part of work is the development of CFD framework for simulating the unsteady flow through the port of a side-burning solid rocket motor to capture the 'longitudinal mode acoustic instability' - initial linear growth and DC shift. The flow is modelled as inviscid and axisymmetric and simulated by solving the Euler equations in ANSYS Fluent®. Propellant gasification is modelled as mass inlet boundary con-

dition and the mass flux is taken as a function of the static pressure at this boundary. Combustion-acoustic coupling in the linear phase is accounted for by a response function formulation in which the burn rate fluctuations is calculated as a product of frequency response and corresponding pressure perturbation amplitude in the frequency domain. This is shown to lead to exponential growth of pressure perturbations in the initial phase as observed in actual motor firings. This then transitions into a limit cycle unlike the DC shift observed in experiments. Accounting for the extinction-re-ignition of propellant subject to high amplitude pressure oscillations which is known to lead to burn rates as high as ten times the mean value for a fraction of the wave time period is shown to capture transition to DC shift - a propellant centric theory which can be a one of the possible explanations for this phenomenon, as opposed to earlier ones based on steep-fronted waves, is demonstrated.

TABLE OF CONTENTS

LIST OF TABLES

LIST OF FIGURES

ABBREVIATIONS

AP	Ammonium Perchlorate
HeQu1-D	Heterogeneous Quasi One Dimensional
HTPB	Hydroxyl-Terminated Polybutadiene
PSD	Particle Size Distribution
$SrCO_3$	Strontium Carbonate
SRM	Solid Rocket Motor
TMO	Transition Metal Oxide
QSHOD	Quasi Steady Homogeneous One Dimensional
UHeQu1-D	Unsteady Heterogeneous Quasi One Dimensional

NOTATION

A_b	Propellant surface area, m^2
A_c	Heat flux amplification factor
A_s	Arrhenius pyrolysis constant, mm/s
A_t	Throat area of nozzle, m^2
B	Transfer number
B_{eff}	effective transfer number
c^*	Characteristic velocity of SRM, m/s
c_p	specific heat capacity, J/kg K
D	Diffusion constant, $\mu m^2/s$
d_0	Diffusion distance, μm
$d_{0,ref}$	Reference diffusion distance, μm
d_i	Diameter of AP particle, i, μm
E_s	Solid phase activation energy, J/kg
E_g	Gas phase energy of activation, J/kg
f	Frequency, Hz
f_{ex}	Burn rate modifier mass fraction
f_{ex}	Extinct AP particle mass fraction
f_{HTPB}	HTPB mass fraction
f_pm	AP mass fraction below premixed cutoff diameter
f_{ll}	Fraction of the surface covered by binder matrix
$f_{ll,amp}$	Amplitude of fluctuation in f_{ll}
f_{nll}	Fraction of the surface not covered by binder matrix
f_s	Non-dimensional frequency
g_f	Geometric factor
H_{AP}	Enthalpy change for AP at surface due to phase change, kJ/kg
H_{bm}	Enthalpy change for binder-matrix at surface due to phase change, kJ/kg
H_{HTPB}	Enthalpy change for HTPB at surface due to phase change, kJ/kg
H_s	Net enthalpy change at surface due to phase change, KJ/kg
k	Thermal conductivity, W/m K
k_g	Thermal conductivity of gas phase, W/m K
K_r	Gas phase reaction rate, s/m^2 atm
$K_{r,eff}$	Effective gas phase reaction rate, s/m^2 atm
l_i	Line average intersection of binder-matrix coated AP particle of diameter, d_i
n	pressure index
n_i	pressure index of binder-matrix coated AP particle of diameter, d_i
p	pressure, atm
p_c	Chamber pressure, atm
$\dot{q}_c$	Solid phase heat flux rate, W/m^2 s
$\dot{q}_g$	Gas phase heat flux rate, W/m^2 s
R	Universal gas constant, J/mol-K
$\dot{r}$	Propellant burn rate, mm/s

$\dot{r}_i$	Burn rate of binder-matrix coated AP particle of diameter, d_i, mm/s
R_p	Pressure coupled frequency response
$R_{p,i}$	Pressure coupled frequency response of AP particle
T_0	Initial temperature of solid propellant, K
t_{bm}	Thickness of binder matrix, μm
T_{eff}	Effective flame temperature, K
T_f	Adiabatic flame temperature, K
$T_{f,ad}$	Adiabatic flame temperature of homogenized binder-matrix coated AP particle, K
T_s	Surface Temperature, K
V_i	Volume fraction
V_{inj}	Velocity of injection of the combustion product, m/s
x^*	Flame stand off distance, μm
x^*_{eff}	Effective flame stand off distance, μm
α	Thermal diffusivity, m^2/s
α_{ND}	Nozzle damping factor, s^{-1}
α_{FT}	Flow turning loss factor, s^{-1}
α_{total}	Total damping factor, s^{-1}
ϵ_T	Amplitude of fluctuation in surface temperature
ϕ_c	Phase difference between q_c and T_s, rad
ϕ_p	Phase difference between $\dot{r}$ and p, rad
ϕ	Homogenized binder-matrix equivalence ratio
ρ_{brm}	Density of burn rate modifier, kg/m^3
ρ_{HTPB}	Density of HTPB, kg/m^3
ρ_{AP}	Density of AP, kg/m^3
ρ_p	Density of propellant, kg/m^3
τ	Non-dimensional time
ξ^*	Non-dimensional flame stand off distance
ξ^*_{eff}	Effective non-dimensional flame stand off distance

CHAPTER 1

Introduction

AP-HTPB based composite propellants with little or no aluminium are preferred in tactical applications to avoid primary smoke. Solid rocket motors (SRMs) using such low-smoke compositions sometimes encounter longitudinal mode acoustic instability leading to significant delays and loss of resources during development. Typical unstable behaviour in tactical missile SRMs includes the initial exponential growth of acoustic waves leading to DC shift - a sudden increase in the mean chamber pressure combined with very high amplitude oscillations (20-30% of the mean) causing catastrophic failures (Blomshield, 2001, 2006). It is not uncommon to see the cause of instability being attributed to the absence of particulate damping associated with condensed Al/Al_2O_3 particles in the port. As shown in Blomshield (2006) the size range of Al/Al_2O_3 particles in the port can only affect waves of frequencies much higher (few thousand Hz) than what is encountered in longitudinal mode instabilities (a few hundred Hz). Also, stable operation in launch vehicle boosters is primarily due to weak pressure coupled response of the propellant to low frequency longitudinal standing modes ($<$ 100 Hz) with aluminium associated particulate damping playing a marginal role if any. Small amplitude limit cycle oscillations in long segmented motors are vortex shedding driven; oscillations in ARIANE 5 P230 booster is a case in point (Vuillot and Casalis, 2004). Therefore the instability in tactical SRMs can be explained only by recognising the strong coupling between propellant combustion and port acoustics. But low-smoke compositions with only AP and HTPB are known to be well behaved - that is, the magnitude of the frequency response of these propellants is of the same order as the steady burn rate index, n (Blomshield *et al.*, 1997). Burn rate index of high solid loading ($>$ 84%) AP/HTPB only propellants in the range of 0.4-0.6 depends on the AP particle size distribution (Varunkumar *et al.*, 2016) and hence the frequency response is usually less than 1 - a strong indicator of stable combustion. This led Varunkumar and Mukunda (2013); Arvind *et al.* (2013) to conclude that the primary factor responsible for instability and the apparently erratic pattern of instability must be related to using of burn rate depressing additives. These additives while lowering the steady burn rate index to less

than 0.3 (a desirable design feature) also seem to increase the frequency response by order of magnitude compared to n. By decreasing the index to as low as 0.3, these additives reduce the burn rate to a level below that of AP at pressures as low as 50 atm. This is an indicator of significant shielding of gas phase heat flux from the surface modulated by binder melt. A lot of qualitative evidence (scanning election micrograph based) for binder melt flow over the AP particle surface is available in literature (Beckstead *et al.*, 1970; Fredrick Jr, 1988; Chakravarthy *et al.*, 1995; Verma and Ramakrishna, 2013; Ishitha and Ramakrishna, 2014). In the case of high binder content propellant ($>$20%), Beckstead *et al.* (1970) and Chakravarthy *et al.* (1995) have observed significant binder melt over AP surface at high pressures ($\sim$ 70 atm). Fredrick Jr (1988) estimated coverage of about 25% over AP particle with binder melt at 68.9 bar for 80% 16 μm AP pocket propellant. Using SEM images of quenched propellants, Verma and Ramakrishna (2013); Ishitha and Ramakrishna (2014) have reported the change in binder melt cover due to the presence of different catalysts (IO, CC, dry and wet AC). Fredrick Jr (1988) recommends the use of X-ray photo-electron spectroscopy as a way to obtain quantitative data on the extent of binder melt cover on the propellant surface. It is pertinent to point out that in the context of the current work binder melt effect is invoked to explain the observed steady and unsteady behaviour of the high energy state of the art propellants. Therefore, qualitative conclusions from propellants with <80% AP are not directly relevant to the current problem. Also, the binder-melt behaviour accounted for by the fraction of the liquid layer (f_{ll}) in Varunkumar *et al.* (2016) is over and above that which is captured by the geometric factor (g_f). Geometric factor (g_f) is the AP part of the surface of the binder-matrix coated AP particles (see Eq. 1.1). This factor accounts for up to 25% coverage of AP particle in propellants with 20% binder as observed by Fredrick Jr (1988) and is consistent with the observation of Beckstead *et al.* (1970); Chakravarthy *et al.* (1995). Therefore quantitative experimental results (perhaps possible with X-ray photo-electron spectroscopy) with the possibility of splitting the measured binder-melt cover into g_f and f_{ll} will help establish the validity of the approach taken here.

$$f_{nll} = g_f - f_{ll}; \quad g_f = \left(\frac{d_{AP}}{d_{AP} + 2t_b} \right)^2 \tag{1.1}$$

In the light of this, the following simple approach was adopted in Varunkumar *et al.*

(2016) - by treating the binder melt coverage as an extreme case of blocking effect, f_{ll} is taken as a function of the decomposition transfer number (B_{ds}). Effect of $SrCO_3$ fraction on f_{ll} is assumed to be linear. The final form is shown in Eq. 1.2.

$$f_{ll} = 2.1 f_{SC}(0.2 + B_{ds})^{-2}; \quad B_{ds} = \frac{T_d - T_s}{T_s - T_0 - H_s/c_p} \tag{1.2}$$

where f_{SC} is the mass fraction of strontium carbonate in the binder-matrix coated AP particle, T_d is the decomposition temperature of $SrCO_3$ (1100 K), T_s is the particle surface temperature, H_s is the surface enthalpy change and c_p is the specific heat. With this approach, it is shown that both low index and less than AP burn rate phenomena can be explained. In the light of this situation, the *blocking effect* based approach adopted in the '*Heterogeneous Quasi One Dimensional (HeQu1D)*' model is extended to the unsteady regime. The validity of such an approach can be evaluated with further experimental evidence in the future.

Another important aspect is the *heterogeneity* associated with wide-distribution AP propellants. The *HeQu1-D* approach has brought out the importance of accounting for this heterogeneity and the need for accurate information on AP particle sizes for good predictive capability. Lack of such a framework till recently is the primary reason why measures adopted to overcome instability in the past appear conflicting - a good example is the list of tactical missiles which have gone into linear instability and DC shift along with the measures adopted to overcome instability compiled by Blomshield (2001). It can be seen that the measures taken to tackle instability were motor specific and cause of instability was never fully understood. There were some efforts to understand the cause of instability - but as brought out earlier, these were severely restricted by the lack of a robust steady state model. Only when the focus is shifted to propellant combustion as the driver of instability, where AP particle size distribution and initial temperature are known to significantly affect the steady behaviour, their effect on the unsteady response can be recognised and captured in a modelling framework. This is in contrast to the earlier approaches of Flandro and group (Malhotra *et al.*, 1997; Flandro *et al.*, 2007; Flandro and Jacob, 2007), where the port gas dynamics is assigned the primary role. Similar considerations also rule out velocity coupling, the unsteady counterpart of erosive burning, in driving instability as its contribution is shown to be negligible or even negative compared to the propellant combustion-acoustic

pressure coupling (Blomshield, 2001). Therefore accurate model for estimating propellant combustion-acoustic pressure coupling (pressure-coupling for short) is of utmost importance to designing of stable tactical missile SRMs and a promising candidate for the same is presented in this thesis.

1.1 Earlier work

Pressure coupling is generally quantified using the so called *frequency response* (R_p) defined as the ratio of percentage fluctuation in mass burn rate of propellant to that of pressure (see Eq. 1.3). Admittance function, which is based on the percentage fluctuation in gas velocity at the propellant surface is also used sometimes and is directly related to the frequency response.

First phenomenological models for unsteady combustion of energetic solids were developed in the 1940s by Zel'dovich (1942) followed by the work of Novozhilov (1973) and group. In these 1-D models, the principal unsteadiness is from the heat transfer in condensed phase (gas phase assumed quasi-steady) and these models were focused more towards homogeneous propellants. Extensive work on unsteady propellant combustion modelling has been done in the US as well. Earlier models for unsteady combustion of solid propellants were inspired by works on liquid propellant rocket instability. They were based on the idea of the time lag between pyrolysis and heat release (Grad, 1949; Cheng, 1961), which translates into a relation between fluctuating velocity and pressure through the admittance function. The inadequacy of such models due to the complex dependence of time lag on propellant composition and frequency, unlike in liquid rockets, are brought out in Culick (1968). It must be recognised here that this difference between liquid and solid propellant rockets stems from the fact that in LP rockets the controlling processes are physical (droplet vaporisation) while in SRMs chemistry plays a significant role in determining burn rates and hence a strong function of the composition. Successive models are consistent with the Russian work where the following assumptions are commonly used - 1) one dimensional homogeneous solid phase; 2) no reaction in the condensed phase; 3) simple Arrhenius type surface pyrolysis law and 4) quasi-steady gas phase. Known as the QSHOD models, Culick (1968) has shown that all of them result in the similar expression for the frequency response

and is given by Eq. 1.3.

$$R_p = \frac{1}{n}\frac{m_s'/\bar{m}}{p'/\bar{p}} = \frac{AB}{\lambda + (A/\lambda) - (1+A) + AB}; \;\; A = \frac{E_s}{R_0}\left(\frac{\bar{T}_s - T_i}{\bar{T}_s^2}\right) \tag{1.3}$$

where A is related to the surface pyrolysis activation energy and B represents the gas phase response to pressure fluctuations. The specific form of B depends on the type of gas phase model chosen. A detailed description of forms taken by B under various gas phase model assumptions, including some cases where the quasi-steady assumption is relaxed can be found in Culick (1968).

The frequencies of dominant longitudinal mode instabilities are less than 2000 Hz since the condensed phase time scales are of the order of few milliseconds. Although this point is adequately addressed in Culick (1968), the need for emphasis on relaxing the quasi-steady approximation in the gas phase, the time scale of which is at least two orders lesser than a solid phase, is not clear. Notwithstanding this, the work reported in Culick (1968) brings out many aspects relevant to the problem of longitudinal instability. These aspects are listed below -

1. The inadequacy of planar flame description without lateral diffusion in understanding unsteady combustion of composite propellants.
2. Absence of connection between the so *intrinsic instability* and the acoustic instability in solid rocket motors.
3. The difficulties in obtaining large frequency response values (~ 3) without having to resort to unrealistically large values for the parameter A and/or including pressure dependence in surface pyrolysis law.

These limitations restrict the connection between QSHOD models and steady state propellant combustion to that of the condition that in the limit of zero frequency, the frequency response value must tend to the pressure index (n), which is trivially satisfied given that the pressure index is taken as an input.

Modern AP/HTPB propellants are highly heterogeneous solids due to the wide multi-modal distribution of particle sizes. Any theory for steady and unsteady combustion of such solids must account for the heterogeneity. This is the reason for the limited applicability of QSHOD based models. Shusser *et al.* (2008) and Spurling (2014) attempted to couple QSHOD approach to simple steady models, like BDP (Beckstead *et al.*, 1971) and BDP based petite ensemble model (Glick, 1974). The results obtained

from these works have limitations due to inherent limitations of the steady state models in accounting for wide AP distributions (Cohen, 1980). These limitations of QHSOD based models led to the development of 3D propellant pack CFD simulation models.

Recently, 2D and 3D propellant pack CFD simulation models (Gross and Beckstead, 2010; Jackson and Buckmaster, 2002; Buckmaster *et al.*, 2005) have been developed to understand the steady and unsteady burn behaviour of AP/HTPB propellants. This is indeed an elegant approach to accurately account for heterogeneity and multidimensional gas phase behaviour. But it is computationally intensive and cannot be considered as a candidate design tool for practitioners. Also, the physical and chemical effects of the ever increasing list of exotic additives used in the propellant design cannot be easily tackled using CFD approach.

Lack of a simple modelling framework for steady state combustion of multi-modal AP/HTPB based composite propellants accounting for heterogeneity, lateral diffusion and binder-melt effects has so far prevented extension of the QSHOD framework to a robust predictive design tool for stability studies. Recently such a steady state model based on the *HeQu1-D* framework has been developed and reported in Varunkumar *et al.* (2016). The work demonstrates the potential use of the serial burning approach based model as a design tool for developing AP/HTPB propellants including the binder-melt effects caused by additives like strontium carbonate ($SrCO_3$). In serial burning approach, each particle coated with the binder is considered as an independent entity for the analysis giving rise to different length scales. The need for length scale small enough to represent the quasi-one-dimensional entity and large enough to treat a change in parameters as perturbations is emphasised by Murphy and Krier (1998). This requirement is fulfilled by binder coated AP particles ranging from 20 to 400 μm. This opens up the possibility for the extension of the *HeQu1-D* framework to the unsteady regime. With this, '*Unsteady Heterogeneous Quasi One Dimensional (UHeQu1-D)*' model is developed by linear perturbation analysis of *HeQu1-D* framework to calculate the frequency response of AP/HTPB based composite propellants.

1.2 Linear instability and DC shift

Another aspect of instability which has received a lot of attention by earlier researchers is the transition of initial exponential growth of acoustic waves into DC shift. The exponential growth of the pressure wave (linear instability) occurs when amplification rate of pressure perturbations due to combustion-acoustics coupling (α_{prop}) exceeds the decay rate (α_{damp}) due to different damping mechanisms present in the motor. The coupling between propellant combustion and chamber acoustics is quantified by the frequency response (R_p) of the propellant as given by Eq. 1.3. Analytical and simulation based approaches have been used in the past to study the phenomenon of linear instability and DC shift in which frequency response of the propellant was considered a known parameter. These efforts were focused on the gas-dynamic aspects of the unsteady port flow assuming a passively responding propellant. De Luca and Summerfield (1992) have first demonstrated the effect of non-linear gas dynamic processes using approximate analysis to explain the limit cycle behaviour. They noticed that amplitude of the bulk waveform matches with the solution obtained from numerical simulation but not the individual modes. An advanced shock capturing finite different scheme was used by Baum and Levine (1986) to model two phase flow through combustion chamber considering a shift in mean pressure as an effect of the steep-fronted weak shock wave. Based on work reported in De Luca and Summerfield (1992), Flandro *et al.* (2007) came up with the approximate model to calculate the change in mean pressure and amplitude of an acoustic wave concluding that DC shift is a result of propagation of steep-fronted shock like waves through the port. In this work, importance was given to modelling nonlinear terms in the energy equation which contribute to losses in the motor. In this the damping due to flow-turning, which is a major damping effect present in the motor containing non-aluminized propellant after nozzle damping, was not considered. Analysis of pressure data from static firings by Arvind *et al.* (2013) shows that in the post DC shift phase, head and aft end clearly shows sinusoidal oscillations of a frequency corresponding to fundamental longitudinal chamber standing mode with clear 180^o difference in phase. This indicates that the spatial gradients in pressure along the length of the motor follows the chamber eigen functions throughout the operation of the motor and hence much less compared to shock like waves. Also, recent analysis of experimental p-t traces by Varunkumar and Mukunda (2013) indicates that as the

amplitude of pressure oscillations grow, the propellant is subjected to increasing levels of pressurisation and de-pressurisation, which, especially beyond the point of DC shift, can be sustained only with peak propellant burn rates as high as 100 mm/s (about 10 times the mean) during pressurisation and quenched conditions (zero burn rate) during de-pressurisation. This indicates the active role of propellant in triggering and sustaining the unsteady flow in the port and not vice-versa. A simple QSHOD based model is developed by Varunkumar and Mukunda (2013) to explain this non-linear propellant burn behaviour and the results of this are reproduced in Fig. 1.1. Here, the burn rate of a typical composite propellant subjected to a high amplitude pressure oscillation is shown to go through cycles of quenching and re-ignition accompanied by sharp burn rate increase up to 10 times the mean for a short duration. Such propellant combustion behaviour can be one of the possible causes of the DC shift.

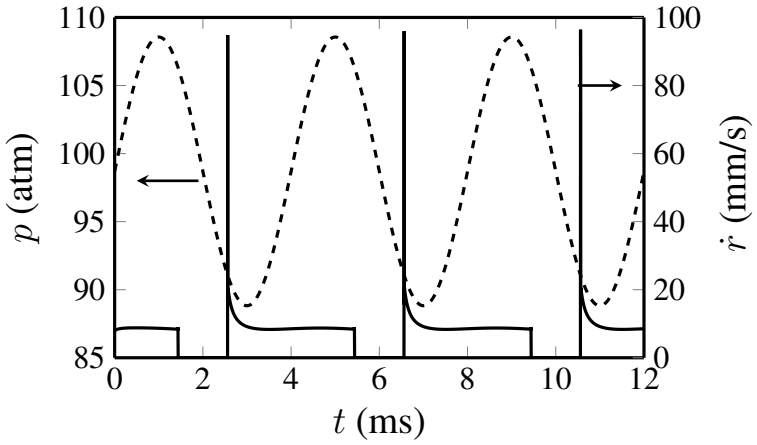

Figure 1.1: Burn rate predicted by unsteady combustion model in Varunkumar and Mukunda (2013) for alternate pressurisation and de-pressurisation cycles.

By coupling the linear perturbation analysis with CFD for port flow and incorporating the cyclic de-pressurisation-pressurisation driven quenching-re-ignition, the exponential growth of oscillations in a rocket chamber and the transition to DC shift are demonstrated in the current work.

1.3 Thesis organisation

Details of the *UHeQu1-D* model, predicted results and their discussions, linear instability and DC shift studies are presented in rest of the thesis and are organised as follows:

Chapter 2 - Unsteady *HeQu1-D* Combustion Model

In this chapter, the three components of the *HeQu1-D*, namely, (1) serial burning approach, (2) pure AP/binder-matrix burn rate equation and (3) quasi 1-D model for binder-matrix coated AP particle are extended to the unsteady regime by perturbation analysis and expression for frequency response is derived.

Chapter 3 - Frequency Response - Results and Discussion

In this chapter, frequency response for conventional propellants and propellants containing burn rate modifier calculated using the derived expression of frequency response are presented. Modified expression of frequency response to incorporate binder melt dynamics is also derived in this chapter and the results are discussed.

Chapter 4 - Linear Instability and DC Shift- a Computational Study

In this chapter, a numerical framework to study linear instability and DC shift which are encountered in tactical missile solid rocket motor is presented.

Chapter 5 - Conclusions and Future Work

This chapter contains important conclusions drawn from the analysis of the unsteady combustion of solid propellants as well as unstable solid rocket motor operations. Aspects which require further explorations are also brought out.

CHAPTER 2

Unsteady *HeQu1-D* Combustion Model

Linear stability analysis of a solid rocket motor requires information about the frequency response of propellant burn rate (R_p) to small pressure perturbations. In this chapter the steady state burn rate model based on the *'Heterogeneous Quasi One Dimensional'* framework is extended to the unsteady regime to derive expressions for the frequency response (R_p). The three components of the *HeQu1-D* model, namely, (1) serial burning approach, (2) pure AP/binder-matrix burn rate equation, (3) quasi 1-D model for binder-matrix coated AP particle are extended to the unsteady regime by perturbation analysis. Aspects of the *HeQu1-D* model are introduced and discussed briefly whenever required. Further details are available in Varunkumar *et al.* (2016); Zaved (2017)

2.1 Serial burning approach to unsteady propellant regression

In the serial burning approach, the burn rate, $\dot{r}$, of a composite solid propellant containing AP particles of diameters d_1, d_2, ..., d_n and corresponding mass fractions of f_1, f_2, ..., f_n are calculated as the inverse of the burning time of a statistically averaged particle path of unit length. Such a line is taken to consist of binder-matrix coated AP particles of various sizes. The line average intersection (l_i), which is the fraction of the statistical particle path composed of binder-matrix coated AP particle of size d_i, is given by,

$$l_i = \frac{V_i(1 + 2t_{bm}/d_i)}{\sum V_i(1 + 2t_{bm}/d_i)}$$

where, V_i is volume fraction of the AP particle, t_{bm} is binder-matrix thickness. Binder-matrix is a homogeneous mixture of HTPB, fine AP (premixed and extinction limit) and burn rate modifiers and it is assumed to be coated over an AP particle with a uniform

thickness of t_{bm}. Using the assumption of uniform thickness the binder-matrix thickness (t_{bm}) is obtained by equating the total volume of the binder-matrix present in the propellant to the volume coated uniformly around the AP particles which are not homogenised with a binder as given in Eq. 2.1. Details of the criterion for homogenisation of AP particles is given in Varunkumar *et al.* (2016); Zaved (2017).

$$\frac{f_{HTPB}}{\rho_{HTPB}} + \frac{f_{pm} + f_{ex}}{\rho_{AP}} + \frac{f_{brm}}{\rho_{brm}} = \sum_i \frac{f_i[(1 + 2t_{bm}/d_i)^3 - 1]}{\rho_{AP}} \tag{2.1}$$

In Eq. 2.1, f_{pm} is the mass fraction of AP particles with size smaller than critical size ($d_{pm} = 16exp(-0.02p)$) and f_{ex} is the mass fraction of quenched AP particles.

The burning time of the line is the sum of the time contribution of each particle size having burn rates, $\dot{r}_1$, $\dot{r}_2$, ..., $\dot{r}_n$. Using this, the propellant burn rate can be calculated by Eq. 2.2.

$$\dot{r}(p) = \left[\sum_i \frac{l_i}{\dot{r}_i(p)}\right]^{-1} \tag{2.2}$$

Pressure index of the propellant (n) can be obtained from index of the individual particle (n_i) by Eq. 2.3. Expression for pressure index of propellant (n) in terms of pressure index of binder-matrix coated AP particles (n_i), is derived using Eq. 2.2, derivation of which is given in Appendix A.1.

$$n = \bar{\dot{r}} \sum_i \frac{l_i}{\bar{\dot{r}}_i} n_i \tag{2.3}$$

Pressure index of particle, n_i is defined as,

$$n_i = \left(\frac{\partial r_i}{\partial p}\right)_{\bar{p}}$$

Introducing the decomposition,

$$\dot{r}_i = \bar{\dot{r}}_i + \dot{r}_i{}', \; \dot{r} = \bar{\dot{r}} + \dot{r}'$$

into Eq. 2.2 and linearizing, the following expression is obtained for the frequency response of propellant in terms of the response of the individual binder-matrix coated

AP particles (see Appendix A.1 for the details of the derivation).

$$R_p = \frac{\dot{r}^{'}/\bar{\dot{r}}}{p^{'}/\bar{p}} = \bar{\dot{r}} \sum_i \frac{l_i}{\bar{\dot{r}}_i} R_{p,i} \tag{2.4}$$

$$R_{p,i} = |R_{p,i}|\, e^{i\phi_{p,i}} = \frac{\dot{r}_i^{'}/\bar{\dot{r}}_i}{p^{'}/\bar{p}}; \quad \phi_{p,i} = cos^{-1}\left(\frac{< r_i^{'}, p^{'} >}{\sqrt{< r_i^{'}, r_i^{'} >< p^{'}, p^{'} >}}\right) \tag{2.5}$$

where, $\bar{\dot{r}}$ and $\bar{\dot{r}}_i$ represent the propellant and individual particle burn rates under the steady conditions respectively, and is obtained using the ***HeQu1-D*** model. Expression (Eq. 2.4) obtained for frequency response of the propellant is similar to that of pressure index of propellant (Eq. 2.3). At zero frequency, when frequency response of the individual particles, $R_{p,i}$ (Eq. 2.5) tends to index of the particles (n_i), the condition of $R_p \sim n$ gets satisfied.

The frequency response, in general, is a complex number, the magnitude ($|R_{p,i}|$) of which represents the amplitude of burn rate fluctuations relative to the imposed pressure fluctuations and the angle (ϕ_p) represents the phase difference between burn rate and pressure fluctuations (Eq. 2.5). The time domain counterpart of frequency response is called the *'burn rate impulse function'*.

Analogous to the steady state model, the current approach begins with the surface heat flux balance equation at the interface between solid and gas phase and proceeds to analyse first, the unsteady behaviour of the two limiting premixed cases namely, pure-AP and homogeneous fine AP/HTPB propellant, and later, that of binder-matrix coated AP particle of size d_i in order to obtain the particle frequency response ($R_{p,i}$).

2.2 Perturbation analysis for pure AP/binder-matrix deflagration

Surface heat flux balance for a pure-AP or homogeneous propellant deflagration is given by Eq. 2.6.

$$k\left[\frac{dT}{dx}\right]_{0^-} = \rho_p \dot{r} H_s + k\left[\frac{dT}{dx}\right]_{0^+} \tag{2.6}$$

where, LHS represents the heat flux transfer from surface into the condensed phase, i.e. condensed phase heat flux ($\dot{q}_c$), the first term on RHS represents the enthalpy change

associated with solid to gas phase transformation and the second term on RHS represents the heat flux transfer from the gas phase flame to the surface ($\dot{q}_g$). Fluctuations in pressure will cause fluctuations in all the three terms. The frequency response can be obtained by calculating the fluctuations in burn rate for an imposed sinusoidal fluctuation in pressure of a range of frequencies of interest. But from the point of view of the perturbation analysis, it is convenient for the algebraic calculations to turn the problem around - that is, calculate the pressure fluctuation corresponding to a known burn rate fluctuation imposed. This is easier due to the direct connection between the burn rate and the surface temperature through the Arrhenius pyrolysis law,

$$\dot{r} = A_s e^{-E_s/RT_s}$$

which enables tabulation of the condensed phase heat flux fluctuations as a function of frequency (more details are given later). This approach has two advantages - first, the reduction in the computational effort and second and most importantly, closed-form expression can be obtained for the frequency response.

Condensed phase

For an imposed sinusoidal fluctuation in surface temperature,

$$T_s = \bar{T_s}(1 + \epsilon_T sin(2\pi ft))$$

the fluctuation in the condensed phase heat flux can be expressed as,

$$\dot{q}_c = \bar{\dot{q}_c}(1 + A_c \epsilon_T sin(2\pi ft + \phi_c)) \tag{2.7}$$

where, ϵ_T is the amplitude and f is the frequency of the fluctuation in T_s, A_c is the flux amplification factor, ϕ_c is the phase difference between T_s and $\dot{q}_c$ and t represents time. Quantities with an over-bar represent steady state values. The condensed phase heat flux under steady condition is $\bar{\dot{q}_c} = \rho_p \bar{\dot{r}} c_p (\bar{T_s} - T_0)$ as given in Varunkumar *et al.* (2016). Framework to calculate quantities, A_c and ϕ_c is reported in Varunkumar and Mukunda (2013) and these are obtained by solution of the unsteady heat conduction

equation for the condensed phase given in Eq. 2.8.

$$\frac{\partial T}{\partial t} + \dot{r}\frac{\partial T}{\partial x} = \alpha\frac{\partial^2 T}{\partial x^2} \tag{2.8}$$

Boundary and initial conditions are given in Eqs. 2.9 and 2.10. Schematic showing boundary conditions for heat transfer at the AP surface during deflagration is given in Fig. 2.1.

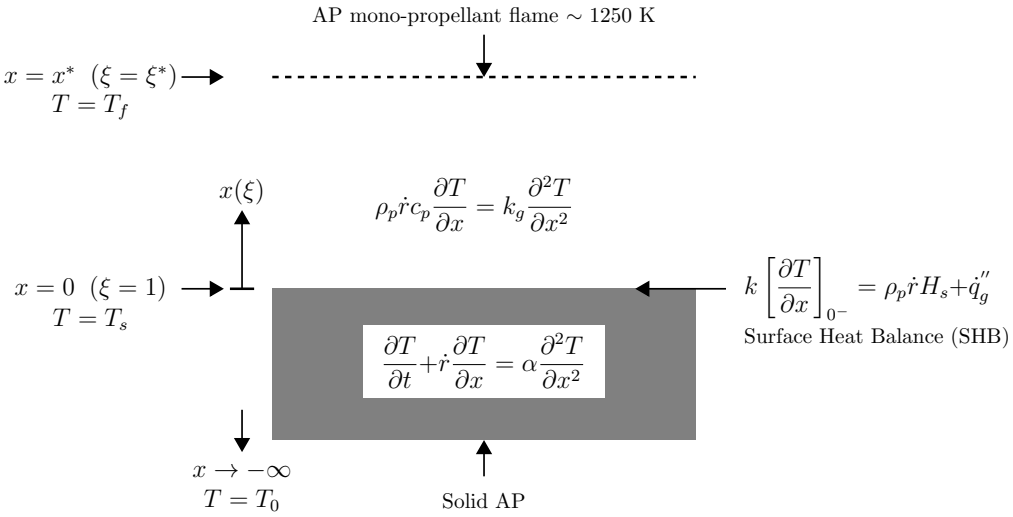

Figure 2.1: Schematic of AP/binder-matrix combustion process.

$$x \to -\infty,\ T \to T_0; \quad x = 0,\ T = T_s = \bar{T}_s(1 + \epsilon_T sin(2\pi f t)) \tag{2.9}$$

$$t = 0, \quad \frac{T(x) - T_0}{\bar{T}_s - T_0} = exp\left(\frac{\bar{\dot{r}}x}{\alpha}\right) \tag{2.10}$$

Since the numerical solution is required for Eq. 2.8, the semi-infinite domain is mapped to a finite domain using the transformation given in Eq. 2.11 along with other non-dimensional variables.

$$\zeta = exp\left(\frac{x\bar{\dot{r}}}{\alpha}\right); \quad \tau = \frac{t\bar{\dot{r}}^2}{\alpha}; \quad f_s = \frac{f\alpha}{\bar{\dot{r}}^2}; \quad \theta = \frac{T}{\bar{T}_0}; \quad R = \frac{\dot{r}}{\bar{\dot{r}}} \tag{2.11}$$

The transformed conduction equation is given by Eq. 2.12.

$$\frac{\partial \theta}{\partial \tau} = \zeta^2\frac{\partial^2 \theta}{\partial \zeta^2} + (1 - R)\zeta\frac{\partial \theta}{\partial \zeta} \tag{2.12}$$

Corresponding boundary and initial conditions are given in Eqs. 2.13 and 2.14.

$$\zeta = 0,\ \theta = \theta_0 = 1; \quad \zeta = 1,\ \theta = \theta_s = \frac{\bar{T_s}}{T_0}(1 + \epsilon_T sin(2\pi f_s \tau)) \tag{2.13}$$

$$\tau = 0, \quad \frac{\theta(\zeta) - \theta_0}{1 - \theta_0} = \zeta \tag{2.14}$$

Solution procedure and other details of numerics are presented later.

Gas phase

The temperature variation in the gas phase is assumed quasi-steady and 1-D with a thin flame at a certain stand-off distance from the surface. The quasi-steady approximation is justified by at least two orders of magnitude difference between the time scales of condensed phase (a few ms) and gas phase (a few microseconds). Gas phase heat flux with quasi-steady assumption, as reported by Varunkumar *et al.* (2016), is given by Eq. 2.15,

$$\dot{q}_g = \frac{\rho_p \dot{r} c_p (T_f - T_s)}{\xi^* - 1} \tag{2.15}$$

where, T_f is the adiabatic flame temperature which depends on the O/F ratio, and ξ^* is non-dimensional flame stand-off distance. Non-dimensional flame stand-off is obtained from dimensional flame stand-off distance by following transformation,

$$\xi^* = exp\left[\frac{\rho_p \dot{r} c_p x^*}{k_g}\right] \tag{2.16}$$

The quasi-steady assumption implies that the gas phase heat flux given by Eq. 2.15 adjusts instantaneously to the fluctuating burn rate ($\dot{r}$) and surface temperature (T_s). Substituting the final flux expressions into Eq. 2.6 we obtain the unsteady flux balance at the surface as shown in Eq. 2.17.

$$\rho_p \bar{\dot{r}} c_p (\bar{T_s} - T_0)(1 + A_c \sin(2\pi f_s \tau + \phi_c)) = \rho_p \dot{r} H_s + \frac{\rho_p \dot{r} c_p (T_f - T_s)}{\xi^* - 1} \tag{2.17}$$

Equation 2.17 connects four fluctuating quantities namely, burn rate, surface temperature, pressure and flame stand-off distance. For an imposed sinusoidal fluctuation in surface temperature, the burn rate fluctuation is calculated using the Arrhenius pyrolysis

law and is given by Eq. 2.18 (Steps to reach this equation are given in Appendix A.2).

$$R = \frac{\dot{r}}{\bar{\dot{r}}} = 1 + e_s \epsilon_T \sin(2\pi f_s \tau); \quad e_s = \frac{E_s}{R\bar{T}_s} \tag{2.18}$$

The remaining two unknowns, pressure (p) and non-dimensional flame stand-off distance (ξ^*) are connected by the mass balance for the thin flame given by Eq. 2.19, where K_r is the overall gas phase reaction rate.

$$\rho_p \dot{r} = K_r p^2 x^* \Rightarrow \xi^* = exp\left[\frac{\rho_p \dot{r} c_p x^*}{k_g}\right] = exp\left[\frac{(\rho_p \dot{r})^2 c_p}{k_g K_r p^2}\right] \tag{2.19}$$

The enthalpy change at the surface for pure AP and homogeneous binder-matrix is given by Eq. 2.20 (Varunkumar *et al.*, 2016),

$$H_{AP} = 0.6p(atm) + 500; \; H_{bm} = \sum_i f_i H_i \tag{2.20}$$

where, H_{AP} is surface enthalpy change for pure AP which is dependent on pressure, and H_{bm} is the enthalpy change associated with binder-matrix decomposition which is taken as a mass fraction weighted average of the constituents enthalpy, namely surface enthalpy of HTPB (-600 kJ/kg), fine AP, and other additives. These values are taken from Varunkumar *et al.* (2016). For AP/HTPB based composite propellants containing no additives, H_{bm} becomes,

$$H_{bm} = f_{HTPB} H_{HTPB} + f_{pm} H_{AP} \tag{2.21}$$

where, f_{HTPB} is mass fraction of HTPB, f_{pm} is mass fraction of premixed AP particles. With all the closure relations in place, we proceed to the linear perturbation analysis of the surface heat balance given by Eq. 2.17.

Linear perturbation analysis of surface heat balance

Under steady conditions, Eq. 2.17 takes the form given in Eq. 2.22.

$$\rho_p \bar{\dot{r}} c_p (\bar{T}_s - T_0) = \rho_p \bar{\dot{r}} \bar{H}_s + \frac{\rho_p \bar{\dot{r}} c_p (T_f - \bar{T}_s)}{\bar{\xi}^* - 1} \tag{2.22}$$

From Eq. 2.22 the following expression for the non-dimensional flame stand-off distance (ξ^*) is obtained (Eq. 2.23).

$$\bar{\xi^*} = 1 + B; \quad B = \frac{T_f - \bar{T_s}}{\bar{T_s} - T_0 - \bar{H_s}/c_p} \tag{2.23}$$

Subtracting Eq. 2.22 from Eq. 2.17 and using the linearized form of all the quantities as shown below,

$$\frac{H_s'}{\bar{H_s}} = \frac{0.6\bar{p}}{\bar{H_s}}\left(\frac{p'}{\bar{p}}\right); \quad \frac{\xi^*}{\bar{\xi^*}} = 1 + \ln\bar{\xi^*}\left(2\frac{\dot{r}'}{\bar{\dot{r}}} - 2\frac{p'}{\bar{p}}\right)$$

the final expression for the frequency response, R_p is obtained as shown in Eq. 2.24.

$$R_p = \frac{2 + h_s/(1-h_s)(0.6\bar{p})/\bar{H_s}(1/g(B))}{2 + (\theta_{fs}(1-h_s) + A_c\cos\phi_c - e_s)/(g(B)(1-h_s)e_s)} \tag{2.24}$$

where,

$$h_s = \frac{\bar{H_s}}{c_p(\bar{T_s} - T_0)}; \quad g(B) = \frac{(1+B)\ln(1+B)}{B}; \quad \theta_{fs} = \frac{\bar{T_s}}{T_f - \bar{T_s}} \tag{2.25}$$

Intermediate steps and other details are given in Appendix A.2. Parameters which are frequency dependent in the expression of the frequency response for pure AP and homogeneous propellants (Eq. 2.24) are A_c and ϕ_c. All other terms are steady quantities and the procedure to estimate these parameters is same as in Varunkumar *et al.* (2016); Zaved (2017). Amplification factor, A_c and phase angle, ϕ_c are calculated using a numerical solution of Eq. 2.12, details of which are discussed in the following section.

2.2.1 Estimation of A_c and ϕ_c

Flux amplification factor, A_c is the ratio of the amplitude of fluctuations in condensed phase heat flux to the amplitude of imposed fluctuations in the surface temperature of the propellant (ϵ_T), and angle, ϕ_c is a phase difference between heat flux fluctuations and surface temperature fluctuations. A_c and ϕ_c as a function of frequency are obtained by solving transformed unsteady diffusion equation (Eq. 2.12) with boundary conditions given in Eqs. 2.13 and 2.14. Crank-Nicholson implicit scheme for time and second order central differencing for space are used to discretise Eq. 2.12 which results in a tridiagonal system of equations. For an imposed surface temperature fluctuation

of a given frequency, the resultant tridiagonal system of equations are solved using TDMA solver to obtain time evolution of temperature profile in the condensed phase. Condensed phase heat flux as a function of time is calculated from the gradient of the obtained temperature profile as $q_c = k[\Delta T/\Delta x]_{x=0}$. Variation in temperature profile in condensed phase with time for 1% fluctuation in surface temperature is shown in Fig. 2.2. Imposed surface temperature fluctuations are having mean of 994 K and frequency of 250 Hz. Figure 2.3 shows percentage fluctuations in condensed phase heat along with surface temperature fluctuations for the case discussed above.

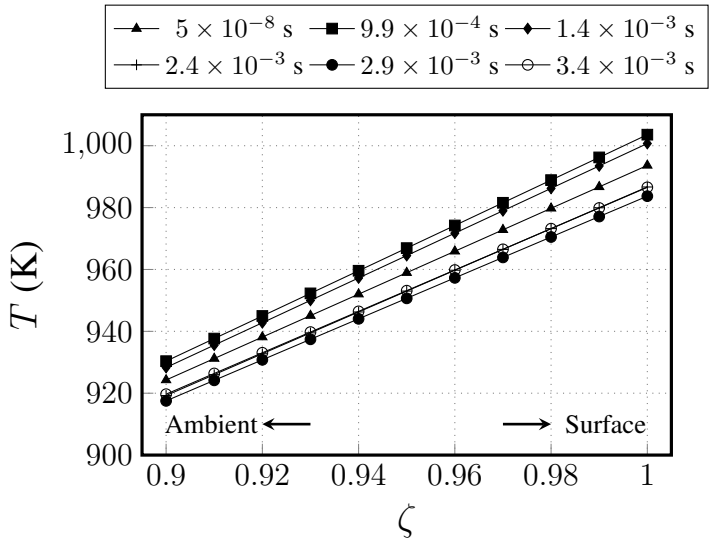

Figure 2.2: Time evolution of temperature profile in condensed phase for 1% fluctuation in surface temperature at 250 Hz.

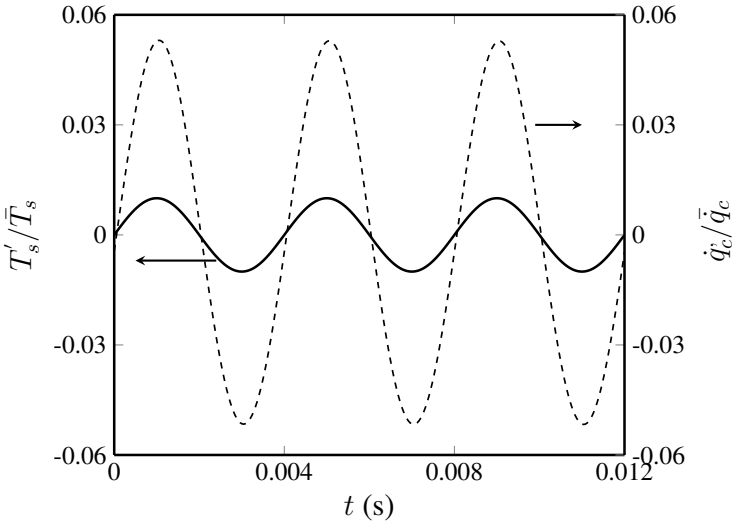

Figure 2.3: Fluctuations in condensed phase heat flux for 1% fluctuation in surface temperature at 250 Hz.

For a given frequency, the flux amplification factor (A_c) and phase difference (ϕ_c)

are obtained from Eq. 2.26, respectively. For the case shown in Fig. 2.3, A_c and ϕ_c are calculated as 5.3 and -0.08 rad, respectively.

$$A_c = \frac{\left|q_c^{'}/\bar{q}_c\right|}{\epsilon_T}; \quad \phi_c = cos^{-1}\left(\frac{< q_c^{'}, T_s^{'} >}{\sqrt{< q_c^{'}, q_c^{'} >< T_s^{'}, T_s^{'} >}}\right) \tag{2.26}$$

Crank-Nicholson scheme used here to discretise Eq. 2.12 is unconditionally stable, but the accuracy of the solution was found to be affected by the size of grid and time steps, particularly at higher frequencies. Grid and time independent studies were carried out to fix grid size and time step to obtain an independent solution. Analysis carried out for grid and time step independence is shown in Fig. 2.4, where A_c and ϕ_c are calculated against non-dimensional frequency f_s. The imposed surface temperature boundary condition is same as shown in Fig. 2.3. For grid independence (Fig. 2.4a), A_c and ϕ_c are calculated for $d\zeta$ of 0.1, 0.02, 0.01 and 0.002 using $d\tau$ of 3.6×10^{-5}. The solution is found to be independent for $d\zeta$ less than or equal to 0.01.

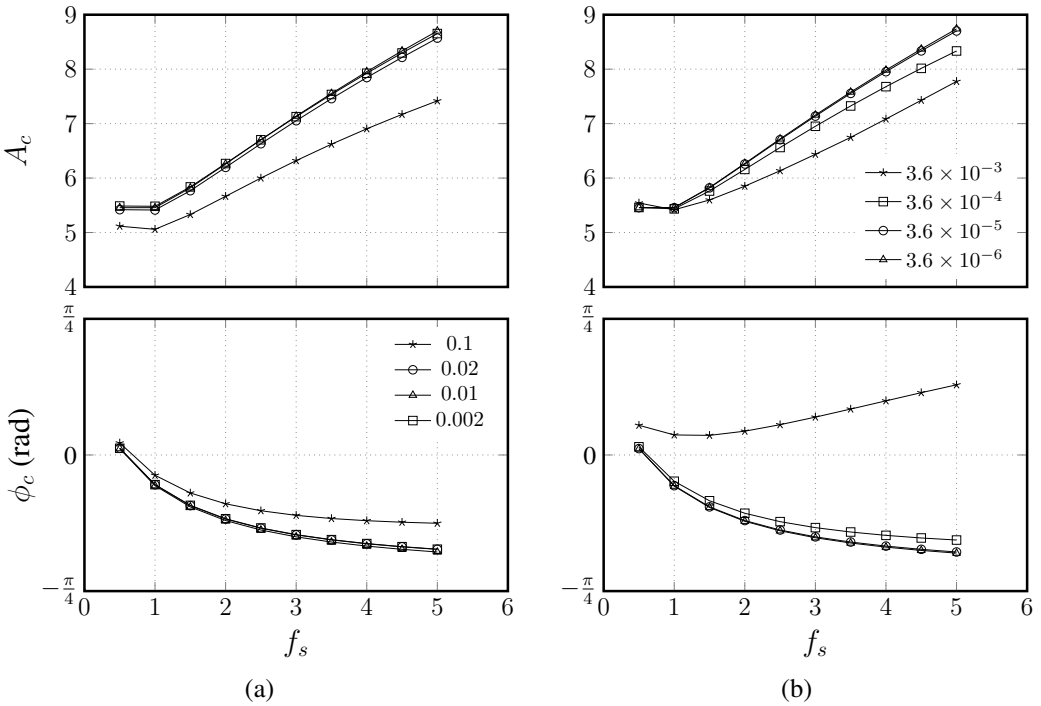

Figure 2.4: A_c and ϕ_c variation with f_s presented for (a) grid independence study (b) time step independence study.

Figure 2.4b shows time independence study where A_c and ϕ_c are calculated for $d\tau$ of 3.6×10^{-3}, 3.6×10^{-4}, 3.6×10^{-5} and 3.6×10^{-6} with $d\zeta$ of 0.01. The solution seems to be time independent below non-dimensional time step ($d\tau$) of 3.6×10^{-4} at

all frequencies. For a given non-dimensional time step ($d\tau$), $dt = d\tau\,\bar{r}^2/\alpha$ varies with particle size. Heterogeneous Propellants contain particles with burn rate ranging from order of one to ten mm/s giving rise to different dimensional time steps (dt). Instead, it is preferred to use a fixed minimum dt which will give a value of $d\tau$ less than 1×10^{-4}. With this constraint, dimensional time step for all computations to calculate frequency response was chosen to be 5×10^{-8} s.

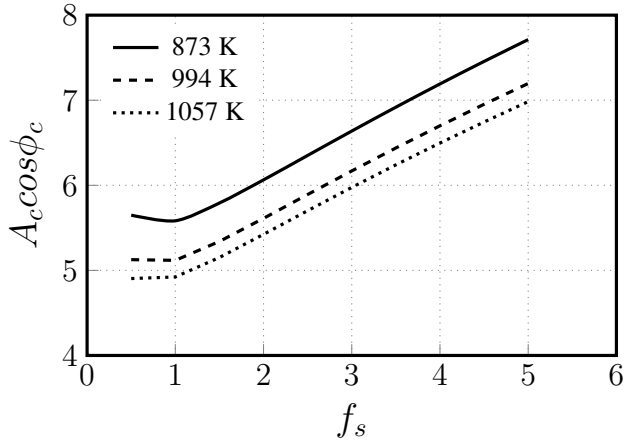

Figure 2.5: Effect of mean surface temperature on $A_c cos\phi_c$ calculated for pure AP.

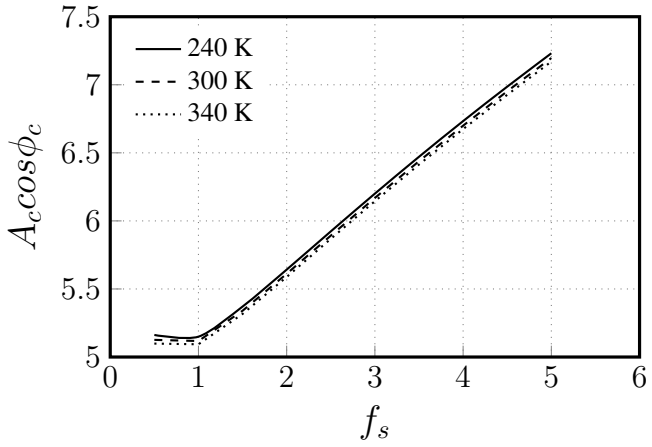

Figure 2.6: Effect of initial temperature on $A_c cos\phi_c$ calculated for pure AP.

The temperature profile in condensed phase responds to any boundary changes with the time scale of the order of $\alpha/\bar{r}^2$. In Fig. 2.4, minimum amplification is obtained at f_s close to 1 which implies that a minimum change in heat flux is required to obtain a given change in surface temperature when both changes take place at same time scale. Figure 2.5 shows effect of mean surface temperature on $A_c cos\phi_c$. It can be seen that the term $A_c cos\phi_c$ decreases with increase in mean surface temperature at all frequencies. This analysis is useful in explaining the change in frequency response in cases where steady state burn rate of propellant changes, for instance, different propellants at same

initial conditions or the same propellant at the different mean pressures. Effect of initial temperature on the term $A_c cos\phi_c$ was examined to see its role in changing the frequency response (R_p) with initial temperature. Values of $A_c cos\phi_c$ calculated for initial temperatures of 240, 300 and 340 K are shown in Fig. 2.6. Pure AP is considered for this analysis and change in mean surface temperature with initial temperature is accounted for. Mean surface temperatures for pure AP at initial temperatures of 240, 300 and 340 K are 984, 994 and 1001 K, respectively at 69 atm. Figure. 2.6 shows $A_c cos\phi_c$ decreases slightly at all frequencies with an increase in initial temperature. This is because AP surface temperature increases with increase in initial temperature and increase in mean surface temperature results in a decrease of $A_c cos\phi_c$ as discussed earlier.

2.2.2 Frequency response for pure AP/binder-matrix

The frequency responses for pure AP and homogeneous propellant (AP/HTPB - 86% /14%) at pressures of 20.7, 68.9 and 120 atm with an initial temperature of 300 K are shown in Figs. 2.7a and 2.7b, respectively. The frequency response is shown in the form of ratio of magnitude of frequency response to pressure index, $|R_p|/n$ and the phase difference, ϕ_p. The magnitude of frequency response is calculated using Eq. 2.24. Steady state parameters required to calculate the magnitude of frequency response are given in Table 2.1. The phase difference, ϕ_p is calculated numerically as given in Eq. 2.4. Pressure index is obtained from the analytical solution (Eq. 2.3). It can, in general, be different from the index which is obtained from curve fitting of pressure-burn rate data. Pressure indexes for pure AP and homogeneous propellant are given in Table 2.1. Frequency responses shown in Fig. 2.7 are calculated against non-dimensional frequency ($f_s = f\alpha/\bar{r}^2$) which is calculated based on mean burn rate. Peak response (R_p) for both pure AP and homogeneous propellant is slightly greater than the index and is obtained at f_s close to 1 where value of $A_c cos\phi_c$ is minimum. This is apparent from the expression of propellant response (Eq. 2.24).

In Fig. 2.7, it can be seen that the magnitude of frequency response of pure AP, as well as homogeneous propellant, decreases with increase in pressure. Pertaining to premixed nature of combustion for both pure AP and homogeneous propellants where the flame temperature remains constant with pressure, mean pressure affects the fluctuations in burn rate with respect to fluctuations in pressure by changing the flame stand-

Table 2.1: Steady state combustion parameters of pure AP and Homogeneous AP/HTPB calculated using *HeQu1-D* model (Varunkumar *et al.*, 2016; Zaved, 2017).

Parameters	AP			Homogeneous Propellant (AP/HTPB-86%/14%)		
	20.7 atm	68.9 atm	120 atm	20.7 atm	68.9 atm	120 atm
$\bar{T}_s$, (K)	873	994	1057	1131	1386	1540
T_f (K)	1250	1250	1250	2862	2862	2862
$\bar{H}_s$ (kJ/kg)	460	487	515	312	334	359
B	3.3	1.2	0.8	3.3	2.0	1.5
h_s	0.80	0.70	0.67	0.37	0.30	0.28
$g(B)$	1.90	1.45	1.32	1.90	1.64	1.52
θ_{fs}	2.3	3.9	5.5	0.7	0.9	1.2
n	0.75	0.73	0.72	0.86	0.86	0.85

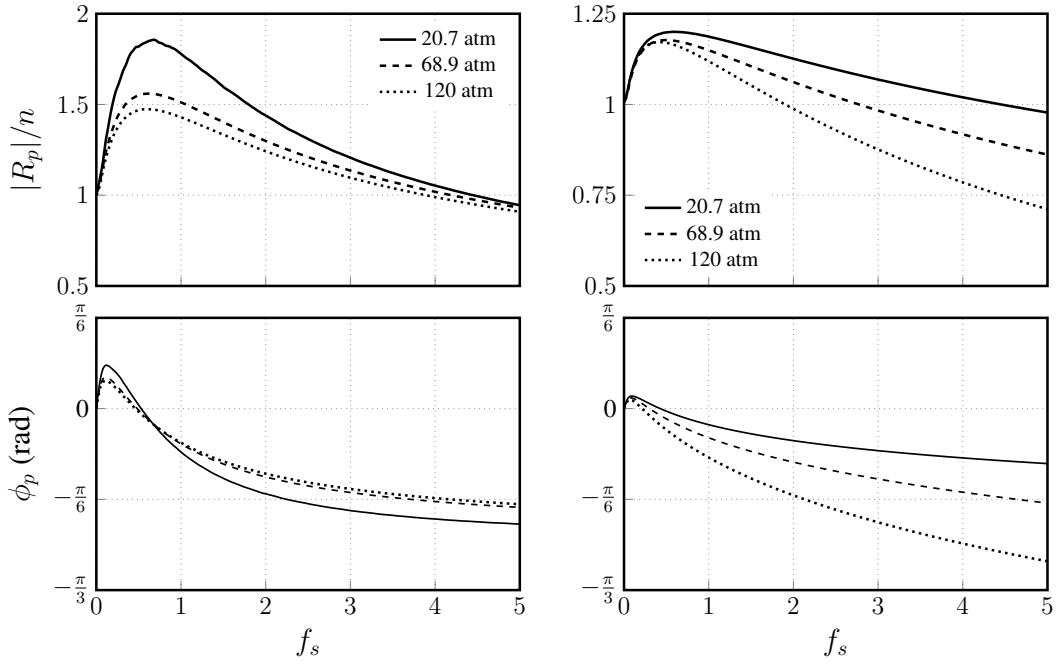

(a) Pure AP

(b) 86% 1-7 μm AP/HTPB

Figure 2.7: Premixed limit pressure coupled frequency responses at an initial temperature of 300 K for different mean pressures.

off distance. Flame stand-off distance is an inverse function of pressure as given in Eq. 2.19, the rate of decrease of which slows down with pressure.

The frequency responses of pure AP at pressure of 68.9 atm for different initial temperatures are shown in Fig. 2.8. There is an increase in the magnitude of frequency response with a decrease in initial temperature. Also, the peak response shifts to lower frequency with a decrease in initial temperature. Effect of initial temperature on the

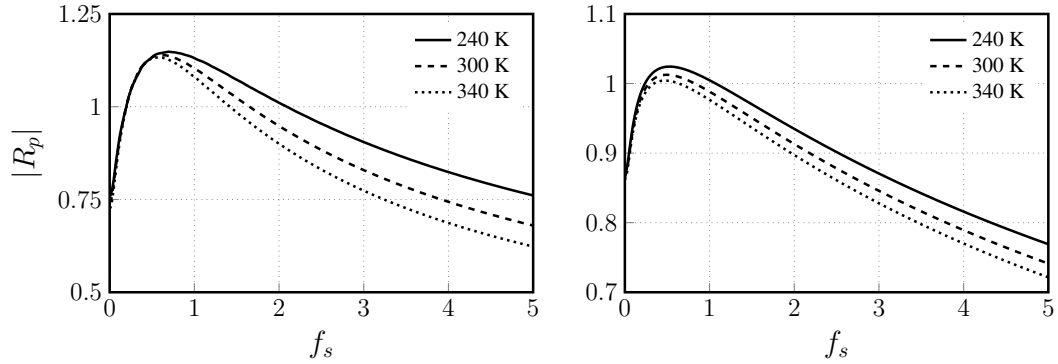

(a) Pure AP (b) 86% 1-7 μm AP/HTPB

Figure 2.8: Premixed limit pressure coupled frequency responses at mean pressure of 68.9 atm for different initial temperatures.

frequency response can be examined through the change in term, $A_c cos\phi_c$ (Fig. 2.6). It is shown in Fig. 2.6 that decrease in initial temperature causes $A_c cos\phi_c$ to decrease at all frequencies. This increases the magnitude of frequency response according to Eq. 2.24.

Comparison of predicted frequency response of pure AP with T-burner results

The frequency responses of ultra pure AP measured using T-burner at different mean pressures are reported in Finlinson *et al.* (1998). Figure 2.9 shows the predicted frequency response of pure AP along with the experimentally measured response at mean pressures of 34.4, 68.9 and 124.4 atm.

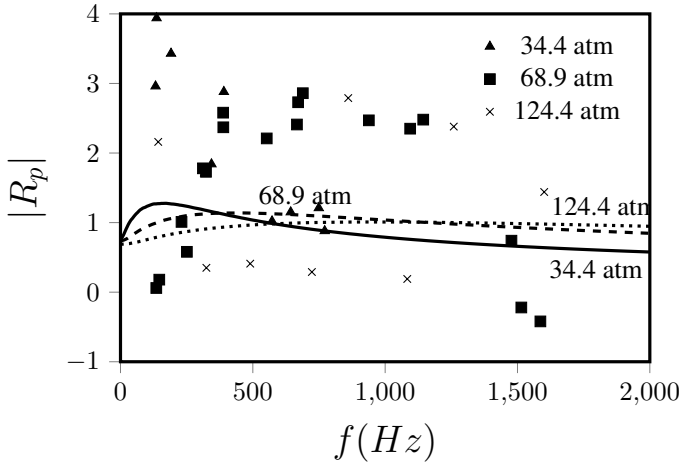

Figure 2.9: Comparison of predicted frequency response (lines) with experimentally obtained one for Ultra pure AP reported in Finlinson *et al.* (1998) (data points).

The magnitude of peak frequency response measured using T-burner is too high

compared to calculated response, but frequencies at which peaks occur are quite close. Calculated peak frequency response decreases as pressure increases from 34.4 to 124.4 bar. A similar trend can be observed from 34.4 to 68.9 bar in case of experimental results. But, due too much scatter in the experimental data at 124.4 bar, a definite conclusion can not be drawn about the mean pressure-peak frequency response trend. Experimentally measured frequency response around 100 Hz is lower than pressure index. This contradicts the expectation from theory that the response should tend to index at zero frequency. T-burner results at low frequencies (< 250 Hz) have inaccuracies arising from the use of long T-burner ($\sim$2 m). There is significant data scatter in the T-burner tests carried out by Perry (1970) for propellant A-13 and scatter is more at higher frequencies. Round-robin test carried out for propellant A-13 using T-burner shows reduced data scatter as reported by Beckstead *et al.* (2002) which is still not justifiable for quantitative comparison. There is a need for measuring frequency response of propellant using alternative measurement techniques. Ultrasonic measurement technique reported in Hafenrichter *et al.* (2004) can be a suitable approach for measurement of frequency response at low frequencies. Another approach of measuring frequency response is introduced in Varunkumar and Mukunda (2017), in which novel approach to measure impulse response instead of frequency response is proposed. Data from these methods are perhaps more suitable for validation of the theory.

2.3 Perturbation analysis for deflagration of binder-matrix coated AP

Perturbation analysis of Quasi-1D framework for binder-matrix coated AP particles remains same as that of AP and homogeneous propellants, except for the linearization of the gas phase heat flux term. The gas phase heat flux term is modified by Varunkumar *et al.* (2016) to account for lateral diffusion of binder-matrix decomposition products. Detailed discussion regarding the implementation of modifications in gas phase heat flux is given in Varunkumar *et al.* (2016); Zaved (2017). Gas phase heat flux, $\dot{q}_g$ for a binder-matrix coated AP particle is given by Eq. 2.27.

$$\dot{q}_g = \frac{\rho_p \dot{r}_i c_p (T_{eff} - T_s) g_f}{\xi^*_{eff} - 1} \tag{2.27}$$

where, g_f is a geometric factor, T_{eff} is an effective flame temperature and ξ^*_{eff} is an effective non-dimensional flame stand-off distance. Geometric factor (g_f) accounts for the fact that gas phase flame directly transfers heat only to a fraction of the total cross-section of coated particle excluding the binder-matrix in a case where binder-matrix can not undergo self-sustained deflagration and it is defined by,

$$g_f = \left(\frac{d_i}{d_i + 2t_{bm}}\right)^2 \tag{2.28}$$

Effective non-dimensional flame stand-off distance is defined by Eq. 2.29, where x^*_{eff} is effective flame stand-off distance which can be obtained from mass flux balance at the propellant surface and $K_{r,eff}$ is effective gas phase reaction rate constant.

$$\xi^*_{eff} = exp\left[\frac{\rho_p \dot{r} c_p x^*_{eff}}{k_g}\right]; \quad \rho_p \dot{r} = K_{r,eff} p^2 x^*_{eff}; \quad K_{r,eff} = A_g exp\left[-\frac{E_g}{RT_{eff}}\right] \tag{2.29}$$

Effective flame temperature, T_{eff} depends on the extent of lateral diffusion of AP and binder decomposition products into each other. Two limiting cases, namely, AP mono propellant which burns with flame temperature of 1250 K and premixed binder-matrix whose flame temperature depends on the O/F ratio, are used to obtain the effective flame temperature (T_{eff}) of a particle as given by Eq. 2.30, where z is a non-dimensional distance defined as the ratio of AP diameter to a diffusion distance (d_0).

$$\frac{T_{eff} - 1250}{T_{f,ad} - 1250} = \frac{1 - e^{-z}}{z}; \quad z = \frac{d_{AP}}{d_o} \tag{2.30}$$

In the Eq. 2.30, effective flame stand-off distance (T_{eff}) depends on the diffusion distance (d_o) which quantifies the extent of diffusion of decomposition products. Diffusion distance (d_o) accounts for the length scale at which diffusion takes place and it is controlled by the diffusion constant (D) and time scale (t_r) of chemical reaction between AP and binder-matrix decomposition products, that is,

$$d_o \sim \sqrt{Dt_r} = \sqrt{\frac{\rho_g D}{K_r p^2}}$$

where, ρ_g is the gas density, K_r is the gas phase reaction rate constant at an adiabatic flame temperature corresponding to the particle O/F and p is pressure in atm. The proportionality constant is accounted for by introducing a reference value for the diffusion

distance ($d_{o,ref}$) corresponding to 20 atm pressure and reaction rate constant of 86% AP loaded particle (30,000 s/m^2). With this, d_0 is expressed as,

$$d_0 = d_{0,ref}(1-\phi)\left(\frac{20}{p}\right)\sqrt{\frac{30000}{K_r}} \tag{2.31}$$

Value of $d_{o,ref}$ = 90 μm taken is validated by Varunkumar *et al.* (2016).

Surface enthalpy change (H_s) for composite propellant is taken as the mass fraction weighted average of the component enthalpy, that is, AP particle and binder-matrix. For AP/HTPB based composite propellant, surface enthalpy change, H_s is given by,

$$H_s = f_{AP}H_{AP} + H_{bm}; \quad H_{bm} = \sum_i f_i H_i \tag{2.32}$$

where H_{bm} is enthalpy of binder-matrix and it is given in Eq. 2.21 for AP/HTPB based composite propellant without any additives.

Perturbation of Eq. 2.27 leads to Eq. 2.33.

$$\dot{q}_g = \bar{\dot{q}}_g\left[1+\left[1-\frac{\theta_{fs,eff}}{e_s}-2g(B_{eff})\right]\frac{\dot{r}_i'}{\bar{r}_i}+\left[z_r\frac{\bar{T}_{eff}}{\bar{T}_{eff}-\bar{T}_s}+g(B_{eff})e_g z_r+2g(B_{eff})\right]\frac{p'}{\bar{p}}\right] \tag{2.33}$$

where,

$$\theta_{fs,eff}=\frac{\bar{T}_s}{\bar{T}_{eff}-\bar{T}_s}; \quad B_{eff}=\frac{\bar{T}_{eff}-\bar{T}_s}{\bar{T}_s-T_s-H_s/c_p}; \quad z_r=\frac{(T_{f,ad}-1250)}{\bar{T}_{eff}}\left[\frac{e^{-\bar{z}}(1+\bar{z})-1}{\bar{z}}\right]; \quad e_g=\frac{E_g}{R\bar{T}_{eff}} \tag{2.34}$$

Using the modified expression for the perturbation of gas phase flux (Eq. 2.33), expression for $R_{p,i}$ for binder-matrix coated AP particle is given by Eq. 2.35.

$$R_{p,i}=\frac{2+h_s/(1-h_s)(0.6f_{AP}\bar{p})/(g_f\bar{H}_s)(1/g(B_{eff}))+z_r[e_g+(1/g(B_{eff}))\bar{T}_{eff}/(\bar{T}_{eff}-\bar{T}_s)]}{2+(g_f\theta_{fs,eff}(1-h_s)+A_c cos(\phi_c)-e_s h_s-g_f e_s(1-h_s))/(g_f g(B_{eff})(1-h_s)e_s)} \tag{2.35}$$

Intermediate steps in obtaining above expression are given in Appendix A.3. Derived expression (Eq. 2.35) for $R_{p,i}$ of binder-matrix coated AP particle is similar to that of pure AP except for the additional term in the numerator. Detailed term-by-term comparison of $R_{p,premixed}$ and $R_{p,i}$ is given in Table 2.2. The additional term t_2 in the expression of $R_{p,i}$ accounts for the effect of diffusion and all other terms are similar to that of $R_{p,premixed}$ but containing modified parameters.

Table 2.2: Comparison of the terms in the expression of magnitude of frequency response of premixed limit and binder-matrix coated AP particle.

$R_p = \frac{2+t_1+t_2}{2+t_3}$	$R_{p,premixed}$	$R_{p,i}$
t_1	$(h_s/(1-h_s))(0.6\bar{p})/(\bar{H}_s g(B))$	$(h_s/(1-h_s))(0.6\bar{p})/(\bar{H}_s g(B_{eff}))$
t_2	-	$z_r[e_g + \bar{T}_{eff}/(g(B_{eff})(\bar{T}_{eff} - \bar{T}_s))]$
t_3	$(\theta_{fs}(1-h_s) + A_c \cos\phi_c - e_s)/(g(B)(1-h_s)e_s)$	$(\theta_{fs,eff}(1-h_s) + A_c cos(\phi_c) - e_s)/(g(B_{eff})(1-h_s)e_s)$

Unsteady terms A_c and ϕ_c are obtained using the procedure outlined earlier. Value of A_c as frequency goes to zero can be calculated by equating expression of magnitude of frequency response (Eq. 2.35) to the expression of pressure index (Eq. 2.36). It should be noted that at zero frequency phase difference will be zero. The expression for the magnitude of frequency response and pressure index look similar, especially numerator of both expressions. Except A_c and ϕ_c, all other parameters appearing in the Eq. 2.24 and Eq. 2.36 are same. A_c and ϕ_c characterise the unsteadiness in condensed phase and all other terms are steady state quantities obtained using *HeQu1-D* model.

$$n_i = \frac{2+h_s/(1-h_s)(0.6 f_{AP}\bar{p})/(g_f \bar{H}_s)(1/g(B_{eff}))+z_r[e_g+(1/g(B_{eff}))\bar{T}_{eff}/(\bar{T}_{eff}-\bar{T}_s)]}{2+\frac{\theta_{fs,eff}(g_f+B_{eff})}{g_f g(B_{eff})e_s}} \tag{2.36}$$

This, hitherto unknown, important connection between the steady and unsteady combustion is critical to using the theory for the design of solid propellants.

2.3.1 Comparison with 2-D CFD model

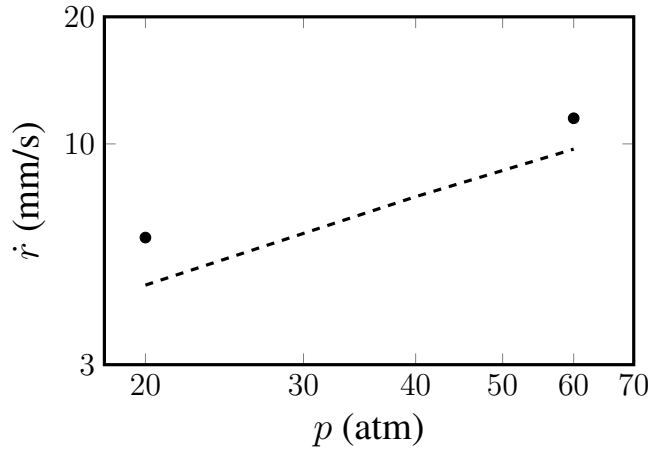

Figure 2.10: Steady state burn rate data. • Buckmaster *et al.* (2005), - - - Current model.

The validity of the assumption of the quasi-one-dimensional behaviour of compos-

ite propellant deflagration is evaluated by Varunkumar *et al.* (2016) by comparing their results with CFD results of Gross and Beckstead (2010). On a similar note, frequency response calculated using current model is compared with frequency response obtained from 2-D numerical simulations by Buckmaster *et al.* (2005) for 74% mono-modal AP (100 μm)/HTPB. In this, the steady state 2-D CFD simulation of a 74% AP (100 μm)/HTPB propellant reported in Jackson and Buckmaster (2002) is extended to the unsteady regime by coupling the gas phase solution (assumed quasi-steady) to the condensed phase using the QSHOD framework. The steady and unsteady burn rate behaviour of the same composition were analysed using the current theory. Using the *HeQu1-D* model, the equivalent statistical particle path for this composition is calculated which consists of 100 μm AP particles coated with 10.1 μm thick HTPB. For this, the predicted steady state burn rate variation with pressure is shown in Fig. 2.10 along with the results from Jackson and Buckmaster (2002). Predicted burn rate from *HeQu1-D* is lower compared to the 2-D CFD simulations by about 20%, while the predicted index is in agreement with CFD. This comparison is taken to be reasonable given the differences in the parameter set used and lack of experimental results for validation. The steady state parameters obtained from *HeQu1-D* are shown in Table 2.3. Negative values of the parameter z_r given in the Table 2.3 indicate that second term (t_2) in the expression of the frequency response of binder coated AP particle (Table 2.2) contributes to the reduction in the magnitude of the frequency response. Parameter z_r is a function of $\bar{z}$ which in turn a function of diffusion distance, d_o (Eq. 2.31). This suggests that the extent of diffusion has the stabilising effect on propellant burning, as expected.

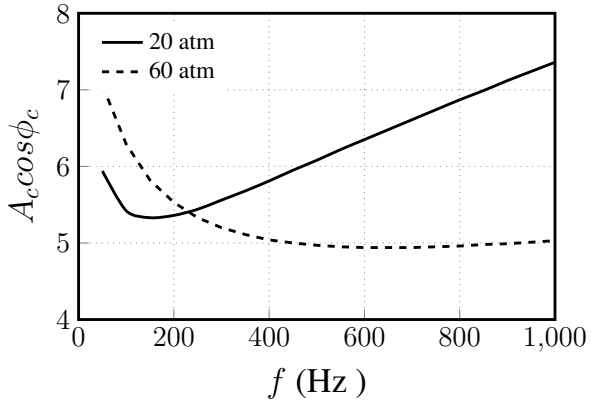

Figure 2.11: Values of $A_c cos\phi_c$ for 74% AP (100 μm)/HTPB propellant at mean pressures of 20 and 60 atm.

Using the steady-state parameters (Table. 2.3) and values of $A_c cos\phi_c$ shown in

Table 2.3: Steady state combustion parameters of 74% AP (100 μm)/HTPB propellant calculated using *HeQu1-D* model.

Parameters	74% AP (100 μm)/HTPB	
	20 atm	60 atm
$\bar{T}_s$, (K)	912	1017
$\bar{T}_{f,ad}$, (K)	2862	2862
$\bar{T}_{eff}$ (K)	1633	1527
$\bar{H}_s$ (kJ/kg)	133	149
B_{eff}	1.5	0.89
h_s	0.21	0.20
$g(B_{eff})$	1.52	1.35
$\bar{z}$	0.51	1.26
z_r	-0.049	-0.067
e_g	4.63	4.95
$\theta_{fs,ef}$	1.26	1.99
e_s	7.13	6.38

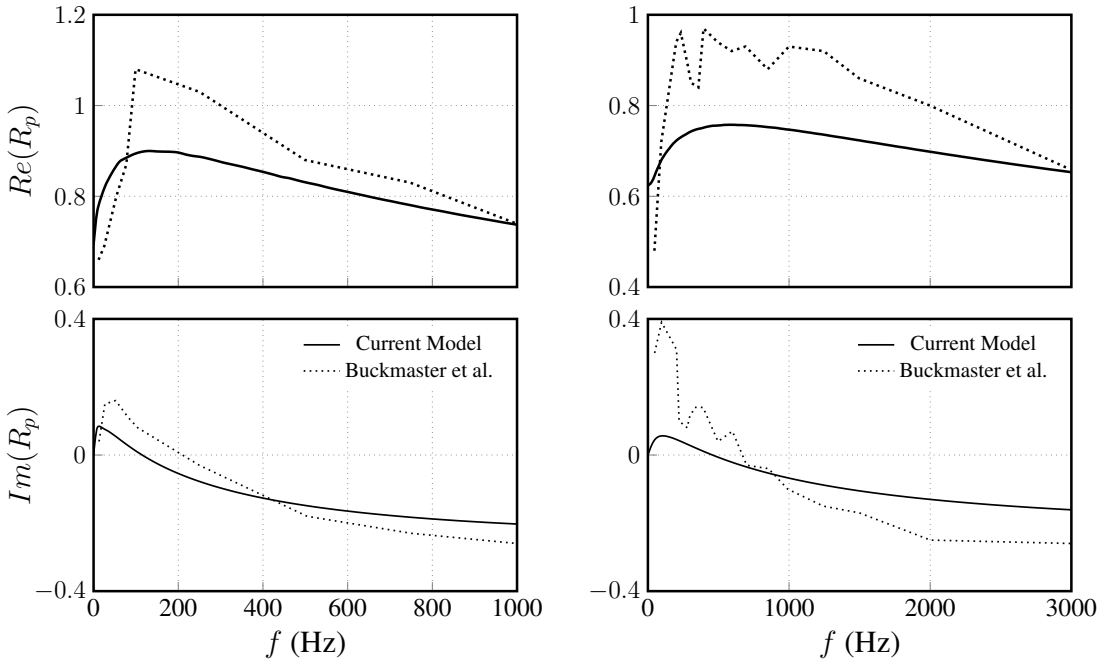

(a) 20 atm (b) 60 atm

Figure 2.12: Real and Imaginary part of frequency response for the mono-modal AP/HTPB propellant containing particles of 100 μm diameter at mean pressures of (a) 20 atm and (b) 60 atm for initial temperature of 300 K.

Fig. 2.11, magnitude of frequency response for propellant discussed above is calculated at pressures of 20 and 60 atm using Eq. 2.35. Real and imaginary part of frequency response obtained from magnitude and phase are shown in Fig. 2.12. Phase is calculated numerically using Eq. 2.5. Comparison of the response obtained by the current model with that obtained from the 2D-CFD simulation shows a similar pattern in case

of both real and imaginary part of frequency response. The frequency at which peak of the real part occurs closely matches at pressure of 20 atm (Fig. 2.12a) as well as 60 atm (Fig. 2.12b). The difference in the magnitude of results can be attributed to the difference in steady state results or the anomalous spikes present in the CFD results. Buckmaster *et al.* (2005) have mentioned that stationary component of mass flux itself fluctuates in time because of the propellant heterogeneity. To eliminate these fluctuations, they have used strategy in which they carry out two burns, one with sine wave pressure fluctuations and other with cosine wave pressure fluctuations and subtract the two mass flux to get fluctuations in mass flux with pressure. Authors have stated that "less careful strategies can lead to questionable results with anomalous spikes (positive or negative) in the frequency response". In case of numerical simulation, the calculated response depends on the generated propellant pack and how accurately the effect of heterogeneity is eliminated. Using one-dimensional analysis with less computational effort without using arbitrary parameters, the current model is capable of obtaining frequency response which conforms well with 2D CFD results.

2.4 Summary

Perturbation analysis of the governing equations resulted in an analytical expression for frequency response. An algorithm is developed to calculate the frequency response which is coded in MATLAB®, the script for which is available on `https://home.iitm.ac.in/varuns/UHeQu1-D_MATLAB_code.zip`. The basic algorithm includes calculation of steady state parameters for all the AP binder-matrix coated particles followed by calculation of A_c and ϕ_c for each particle and finally an overall response. It is important to note that the only additional parameter introduced in the unsteady analysis compared to steady model is the thermal diffusivity (α) — this is to account for the unsteady heat transfer process in the condensed phase. The close connection between the expressions of frequency response and pressure index is clearly brought out. Also, the comparison of frequency response obtained using current model with that of 2D-CFD calculations by Buckmaster *et al.* (2005) shows a reasonable agreement. Next chapter deals with the predictions and analysis of the frequency response for multi-modal AP/HTPB composite propellants.

CHAPTER 3

Frequency Response of Composite Propellants - Results and Discussion

In this chapter, the results of frequency response for various composite propellants obtained using the model discussed in the previous chapter will be presented. Effects of pressure, initial temperature, AP particle size distribution and solid loading will be discussed. Conditions under which the fluctuation of binder-melt becomes important and the related dramatic effects due to additives will also be discussed. Though very limited and scattered, available experimental results will be used to elucidate novel aspects of the model. Table 3.1 contains details of the propellant compositions analysed here along with the available sources for experimental steady and unsteady results. The term conventional propellants used in Table 3.1 is described in Varunkumar *et al.* (2016). Conventional propellants are a category of commonly used composite propellants which do not contain a large fraction of very fine AP (< 20 μm). Although many practical propellants contain additives to modify ballistic properties, propellants with additives are excluded from the conventional category and are treated separately. Note that the experimental results for unsteady response are very limited for state of the art high energy propellants, compared to steady state burn rate results.

Table 3.1: Propellant compositions used in the current study.

Category	Propellant ID	Remarks	Source
Conventional propellants (AP/HTPB only)	SD-III-18,19,21, 25	High SL - 87.4%; detailed distribution available	Miller (1982)[s];
	Thiokol #10	High SL - 88% with DDI as curative in binder; Only mean particle size and proportion	Hafenrichter *et al.* (2004)[us]
Propellants with additives	IR0 (0.5% Carbon black)	SL - 86%; Only mean particle size available	Blomshield *et al.* (1997)[us]
	Thiokol #4,#5 (2% TMO)	-	Hafenrichter *et al.* (2004)[us]
	COM1 (2.5% $SrCO_3$)	SL - 80%; detailed distribution available	Varunkumar *et al.* (2016)[s]; Arvind *et al.* (2013)[us]

[s] - steady results; [us] - unsteady response results.

3.1 Conventional propellants

In this section, the predicted frequency responses of the conventional propellants namely, SD-III-18, SD-III-19, SD-III-21 and SD-III-25 are presented and effects of mean pres-

sure, initial temperature of propellant, AP particle size distribution and solid loading on frequency response are discussed. Comparison of predicted and experimentally measured frequency response of Thiokol #10 (also comes under the conventional category of propellants) is shown at the end of the section.

The frequency response of composite propellants containing only AP and HTPB (termed conventional propellants here) is obtained from the frequency response of individual binder-matrix coated AP particles and corresponding line fractions using Eq. 2.2. Note from Eq. 2.2 that the steady state burn rate of binder-matrix coated AP particles are required as input to this equation. The *HeQu1-D* model is used to obtain the steady state burn rate of binder-matrix coated AP particles and the burn rate of the propellant. The predicted propellant burn rates and pressure indexes are shown in Table 3.2 for conventional propellants. The predicted steady state burn rates are within $\pm$ 10% of experimental results.

Table 3.2: Composition details and predicted steady state results for conventional propellants from Miller (1982).

Propellant	Composition		Burn rate (mm/s)			Index		
	Particle size (μm)	Fraction (%)	20.7 atm	68.9 atm	120 atm	20.7 atm	68.9 atm	120 atm
SD-III-18	90/20	42.12/45.28	10.5	18.0	22.9	0.67	0.53	0.46
SD-III-19	200/20	31.6/55.8	8.4	10.0	20.4	0.65	0.59	0.54
SD-III-21	400/200/50/20	31.6/31.6/10.52/13.69	6.2	10.0	13.8	0.56	0.61	0.62
SD-III-25	400/50/20	42.12/31.6/13.69	6.0	11.0	15.7	0.59	0.62	0.59

Predicted frequency responses for the propellants described in Table 3.1 at three pressures, 20.7, 68.9 and 120 atm, in the form of magnitude ($|R_p|$) and phase difference (ϕ_p) are shown in Figs. 3.1 (SD-III-18, SD-III-19) and 3.2 (SD-III-21, SD-III-25). Propellants from Miller (1982) considered here cover a wide range of particle sizes - bi-modal SD-III-18 (90/20 μm) and SD-III-19 (200/20 μm), tri-modal SD-III-25 (400/95/20 μm) and SD-III-21 is quad-modal (400/200/50/20 μm) propellant.

3.1.1 Effect of mean pressure

Unlike AP (Fig. 2.7a) and homogeneous propellant (Fig. 2.7b), the peak frequency response of a multi-modal AP/HTPB propellant does not always decrease with pressure. Propellant SD-III-21 is a case in point - the magnitude of peak response increases

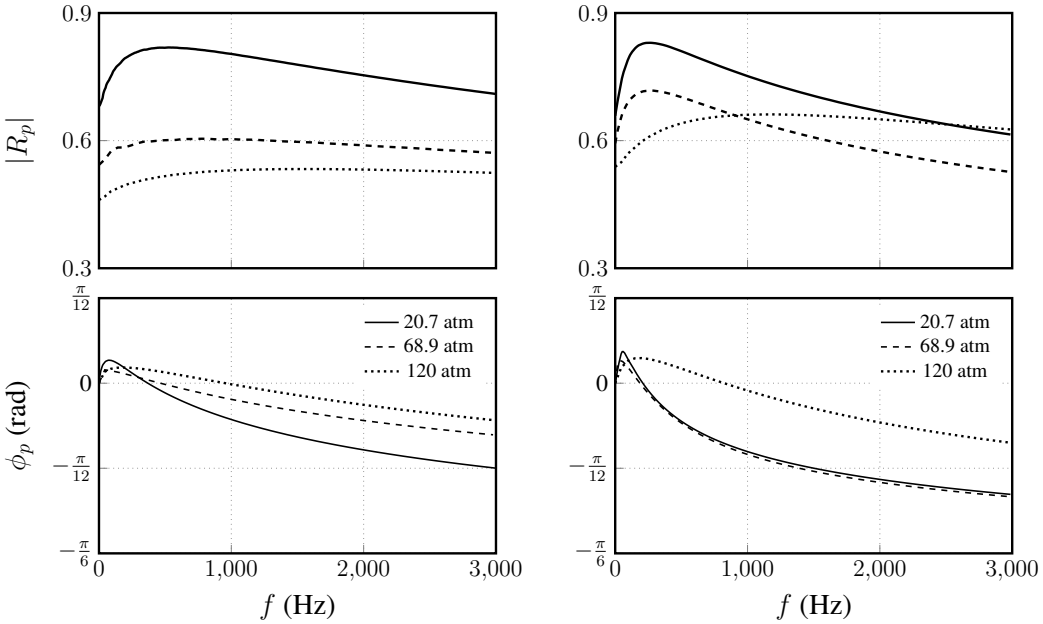

(a) SD-III-18 (b) SD-III-19

Figure 3.1: Frequency response showing $|R_p|$ and ϕ_p vs dimensional frequency, f for propellants SD-III-18 and SD-III-19.

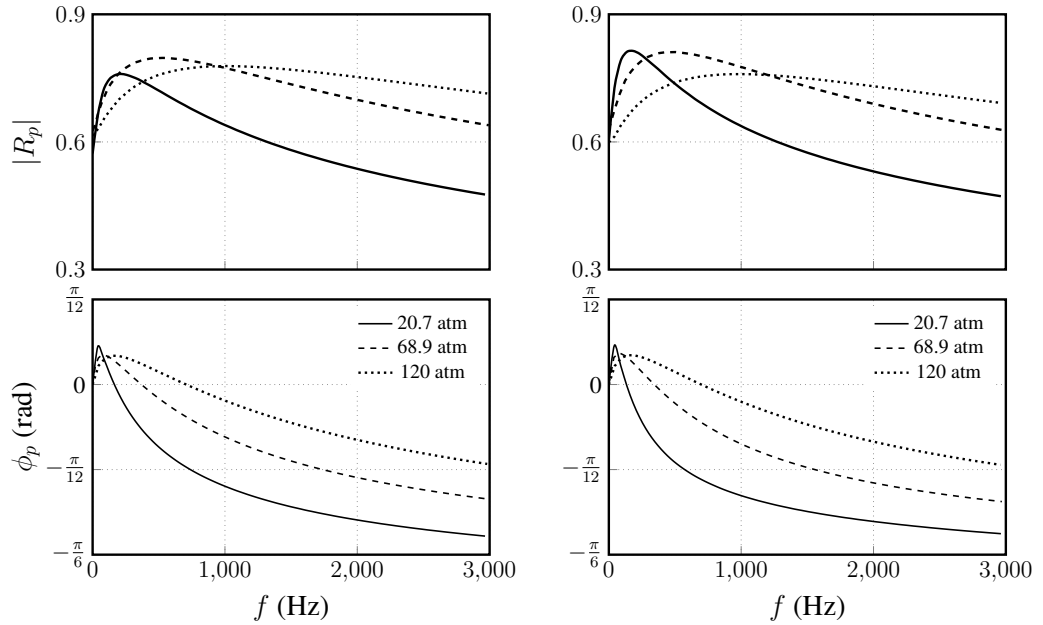

(a) SD-III-21 (b) SD-III-25

Figure 3.2: Frequency response showing $|R_p|$ and ϕ_p vs dimensional frequency, f for propellants SD-III-21 and SD-III-25.

with pressure from 20.7 to 68.9 atm and then decreases. It is also observed for propellants SD-III-19, SD-III-21 and SD-III-25 that magnitude of frequency response at frequencies higher than peak frequency increases as mean pressure increases from 68.9 to 120 atm. Experimental results of Ibiricu (1969) are consistent with these observa-

tions. This complex behaviour is because of the following - the overall response of the composite propellant depends on that of binder-matrix coated AP particles (Eq. 2.35) and unlike pure AP and homogeneous propellants, the effective temperature (T_{eff}) of binder-matrix coated AP particle varies with pressure and O/F. As can be seen from Eq. 2.30, T_{eff} is dependent on $z = d_{AP}/d_0$ and d_0 decreases with pressure (as $1/p$, see Eq. 2.31). Therefore with an increase in pressure, the deflagration of coated AP particles shift towards mono-propellant limit. This, depending on the particle size and O/F can lead to an increase or decrease in response (see Fig. 3.3). Therefore accounting for the heterogeneity due to multi-modal AP distribution is critical to understand the pressure dependence of frequency response.

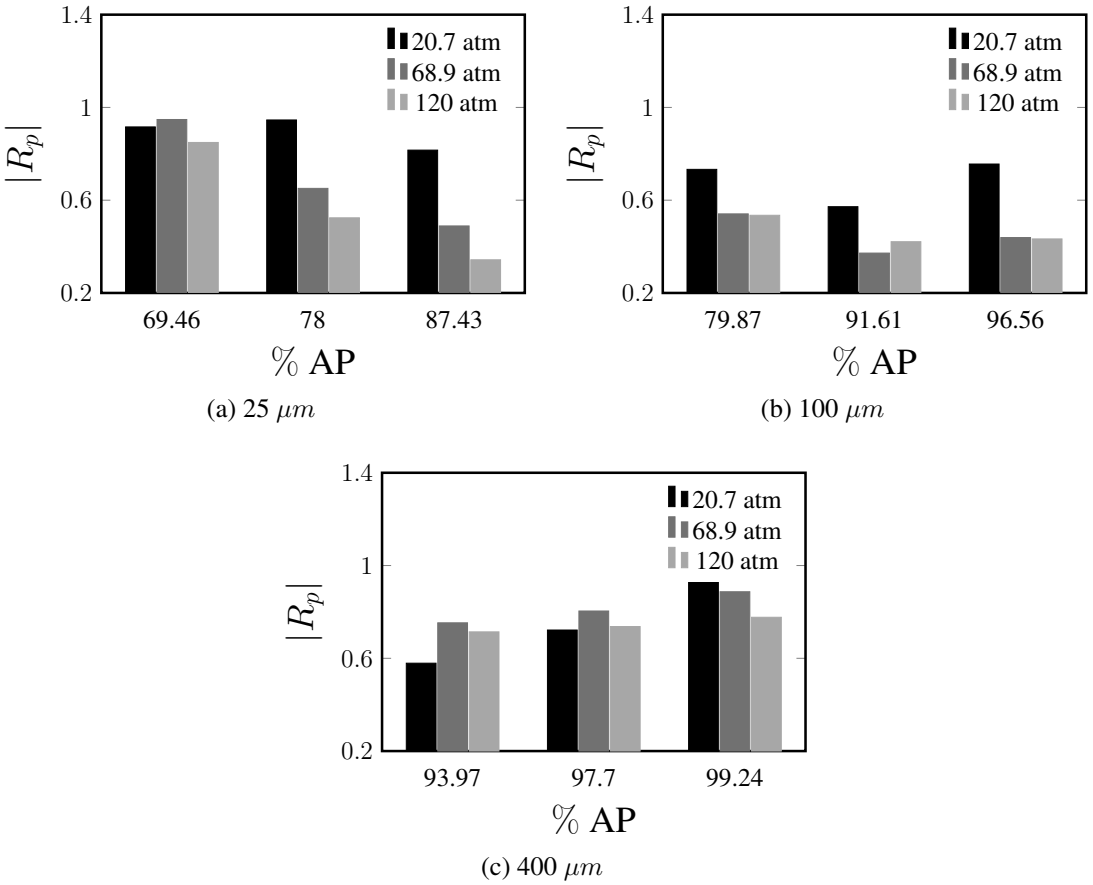

(a) 25 μm

(b) 100 μm

(c) 400 μm

Figure 3.3: Mean pressure effect on frequency response of AP particle of different sizes and O/F at 250 Hz.

To further elucidate the pressure effects, the response is calculated for 25, 100 and 400 μm particles with three different O/F ratios. The choice of O/F ratios is based on the following consideration - in a typical composite propellant mix, 25 μm is fuel rich, 100 μm is close to stoichiometry and 400 μm particles are AP rich as shown in Zaved

(2017). The calculated magnitude of frequency response at 250 Hz for each case at mean pressures of 20.7, 68.9 and 120 atm are shown in Fig. 3.3. There is a monotonic decrease in the magnitude of frequency response with an increase in pressure for the leaner case of all particles considered - 25 μm with 87.43% AP, 100 μm with 96.56% AP and 400 μm with 99.24% AP. In these cases, there is a relatively larger decrease in the magnitude of frequency response with an increase in pressure from 20.7 to 68.9 atm than that from 68.9 to 120 atm. These trends are similar to pure AP. The decrease in the magnitude of response is more in case of particles of size 25 and 100 μm than that of 400 μm particle. This suggests that decrease in the magnitude of frequency response with an increase in mean pressure will be more for propellant containing large fractions of 25 and 100 μm particles than propellant containing large fractions of 400 μm particles. In case of fuel rich particles - 25μm with 69.46% AP and 400 μm with 93.97 AP, there is an increase in the magnitude of frequency response with an increase in pressure from 20.7 to 68.9 atm at 250 Hz. Following this, the presence of higher fractions of richer 400 and 20 μm particles in SD-III-21 can be the reason for the increase in the magnitude of peak response with an increase in pressure from 20.7 to 68.9 atm (Fig. 3.2a).

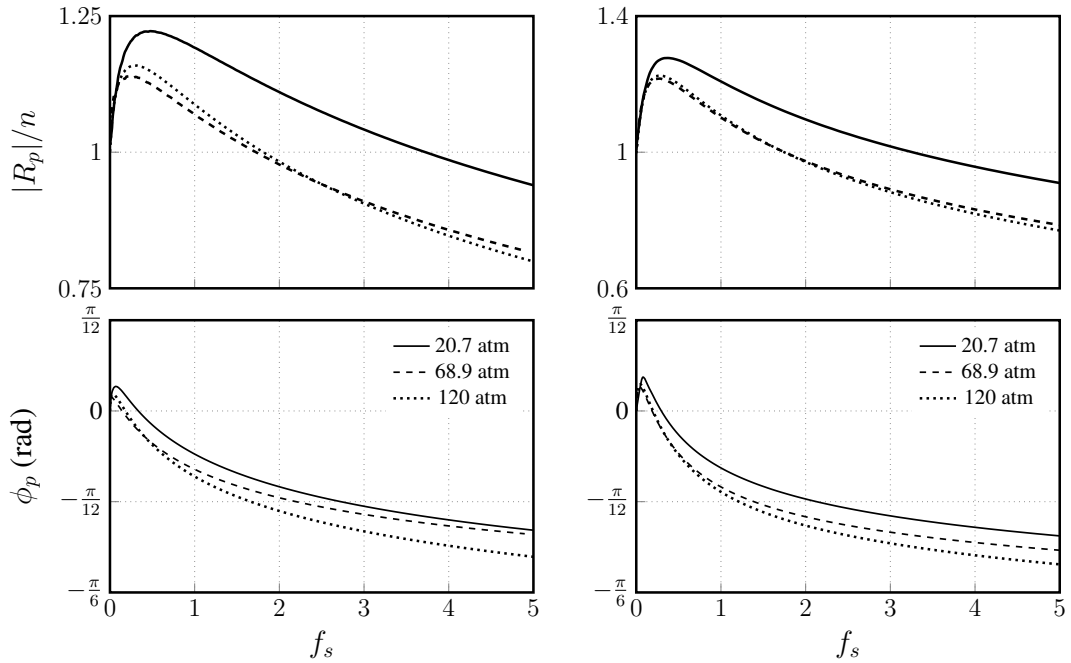

(a) SD-III-18 (b) SD-III-19

Figure 3.4: Frequency response showing $|R_p|/n$ and ϕ_p vs non-dimensional frequency, f_s for propellants SD-III-18 and SD-III-19

Figures 3.4 and 3.5 show variation of scaled response (R_p/n) with non-dimensional

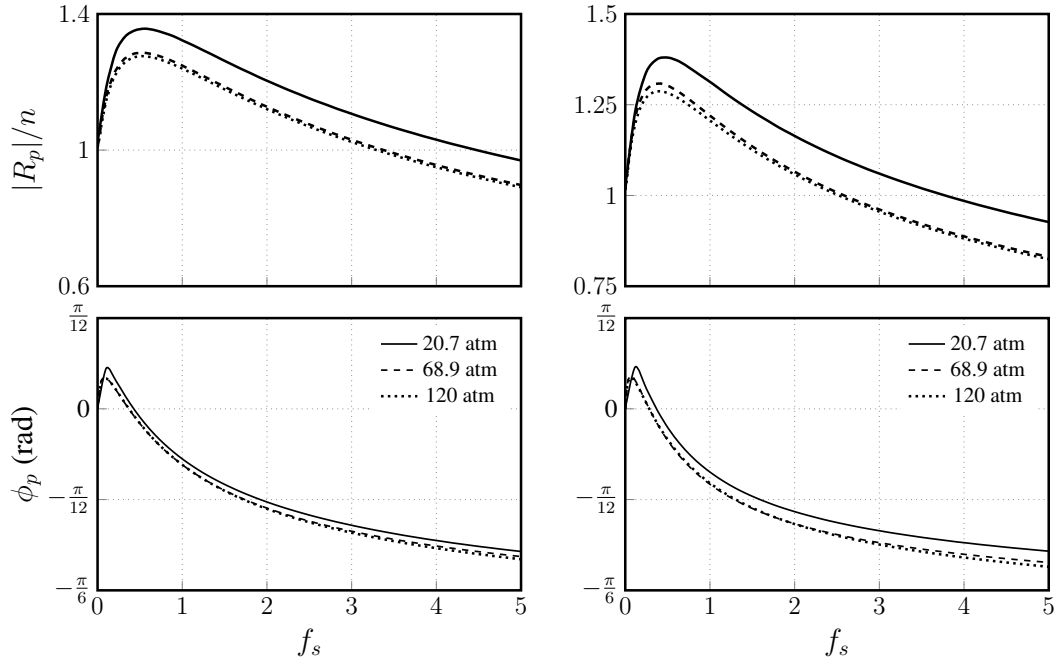

(a) SD-III-21 (b) SD-III-25

Figure 3.5: Frequency response showing $|R_p|/n$ and ϕ_p vs non-dimensional frequency, f_s for propellants SD-III-21 and SD-III-25

frequency, $f_s = f\alpha/\bar{r}^2$. As expected $R_p/n = 1$ at $f_s = 0$ and the peak response is of the same order as n.

3.1.2 Effect of initial temperature

Frequency responses corresponding to initial temperatures of 240, 300 and 340 K for the same four conventional propellants at a pressure of 68.9 atm are given in Fig. 3.6. It shows a slight decrease in frequency response with an increase in the initial temperature. The unsteady behaviour of composite propellant with respect to the initial temperature of condensed phase is expected to be same as that of pure AP as the condensed phase is modelled similarly to pure AP. Frequency responses of the propellant SD-III-19 obtained using T-burner for different initial temperatures are reported in Spurling *et al.* (2010). Responses are measured at initial temperatures of 244, 300 and 355 K and the mean pressure of 68.9 atm to study the effect of initial temperature of the propellant on frequency response. Predicted responses for all three cases are shown along with measured responses in Fig. 3.7. At about 800 Hz, the data indicate that the response decreases with increase in initial temperature in agreement with theory. In no other aspect, the data can be claimed to agree with theory. It is pertinent to point out

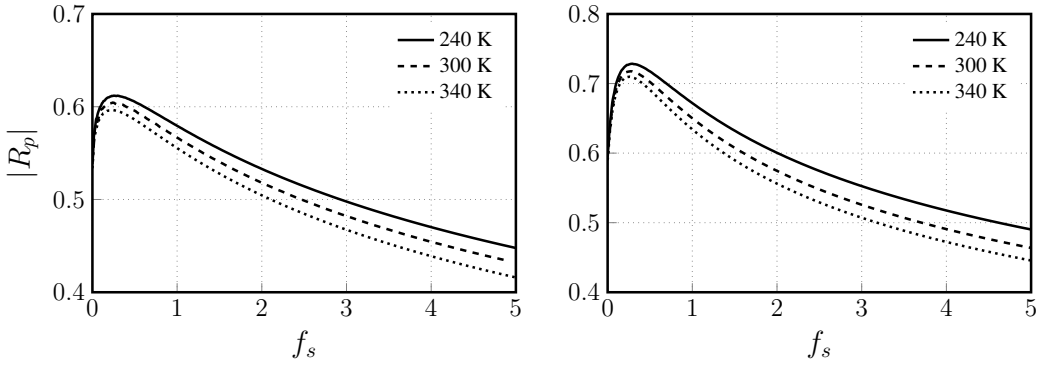

(a) SD-III-18 (b) SD-III-19

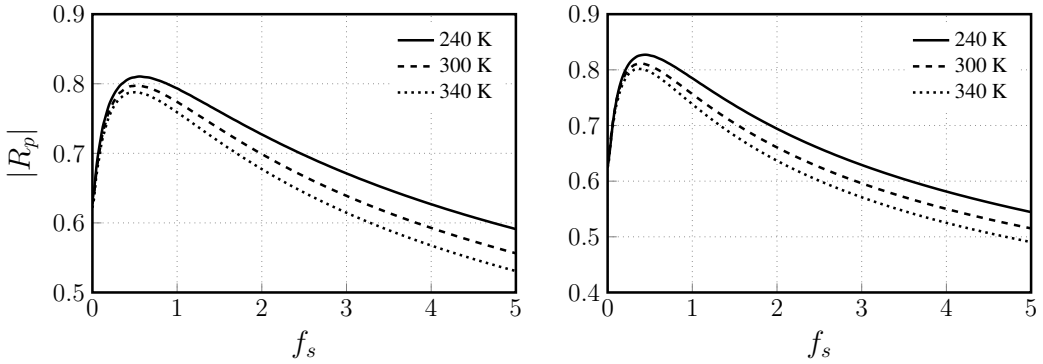

(c) SD-III-21 (d) SD-III-25

Figure 3.6: Effect of initial temperature on frequency response of propellants SD-III-18, SD-III-19, SD-III-21 and SD-III-25 at pressure of 68.9 atm.

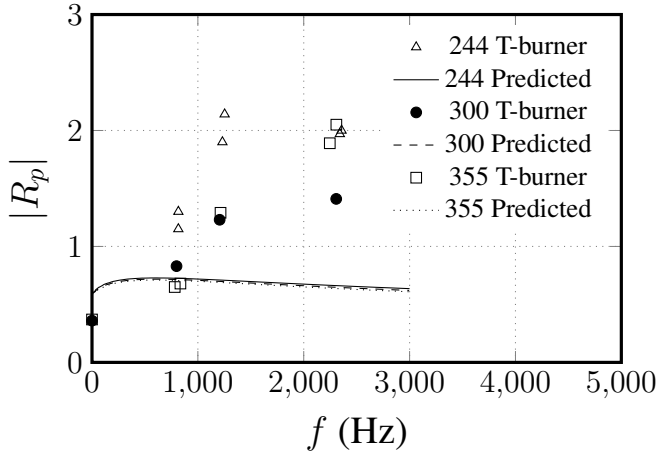

Figure 3.7: Comparison of predicted response of SD-III-19 with experimentally measured response using T-burner.

that these results were obtained using T-burner technique. Yet the experimental results were included along with the predictions to bring out the need for better techniques for response measurement.

3.1.3 Effect of AP particle size distribution

Ballistic properties (burn rate, pressure and temperature sensitivity) of AP based composite propellants are primarily controlled by the AP particle size distribution (PSD). State of the art high-energy propellants contain $\geq 84\%$ AP usually in bi- or tri-modal distribution, with nominal particle sizes ranging from as small as 20 to 400 μm. Such wide distribution of particle sizes is shown to lead to a wide O/F distribution in Varunkumar *et al.* (2016) with the burning of fine and large AP particles controlled by close to premixed conditions and diffusion playing a role for intermediate particle sizes. Therefore large and small particles tend to have a higher index (n > 0.7) while intermediate particle sizes have a lower index (n $\sim$ 0.4 - 0.6). Similarly, the magnitude of the frequency response of the propellant depends on the size distribution of AP particles.

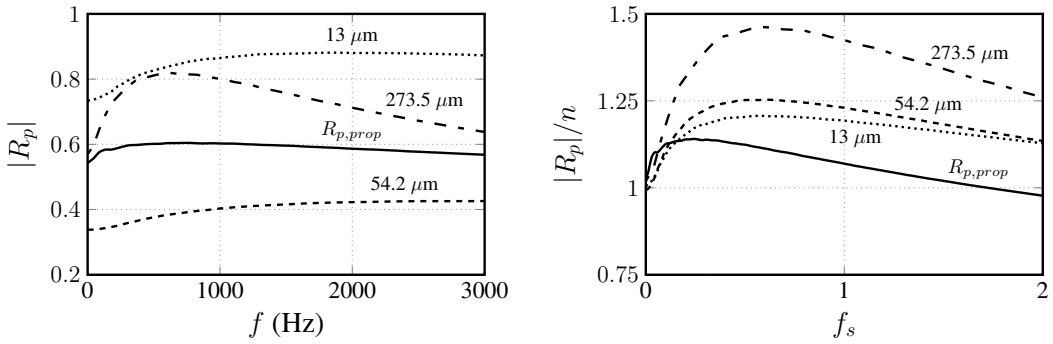

(a) R_p vs Frequency (b) R_p/n vs Non-dimensional Frequency

Figure 3.8: Frequency response for the select particles of propellant SD-III-18 at pressure of 68.9 atm.

To analyse the effect of AP particle size distribution on the frequency response of the propellant, frequency responses for the select particles of the propellant SD-III-18 along with overall response calculated at a mean pressure of 68.9 atm and an initial temperature of 300 K are shown in Fig. 3.8. Figure 3.8a shows $|R_p|$ vs f for particles considered and Fig. 3.8b shows same information in the form of $|R_p|/n$ vs f_s. In Fig. 3.8a, it can be seen that the magnitude of peak frequency response for particles of sizes 273.5 and 13 μm is higher than that of 54.2 μm particle. The response being high for the finer particles like 13 μm particle is due to the higher pressure index - similar result from experiments for fine particles is reported by Ibiricu (1969). A comparison of responses of these particles with that of pure AP and 82.7% solid loaded homogeneous binder is shown in Fig. 3.9. Pure AP and fine-AP/HTPB propellants

represent the two premixed limits. The general expectation is that particles which burn close to these premixed limits should have similar unsteady behaviour as that of pure and homogeneous propellant - large and fine binder-matrix coated AP particles. In line with this, the responses obtained for particles of sizes 273.5 μm (Fig. 3.9a) and 13 μm (Fig. 3.9b) are similar to that of pure AP and homogeneous binder, respectively, while the response of particle of size 54.2 μm (Fig. 3.9c) is lower due to diffusional effects.

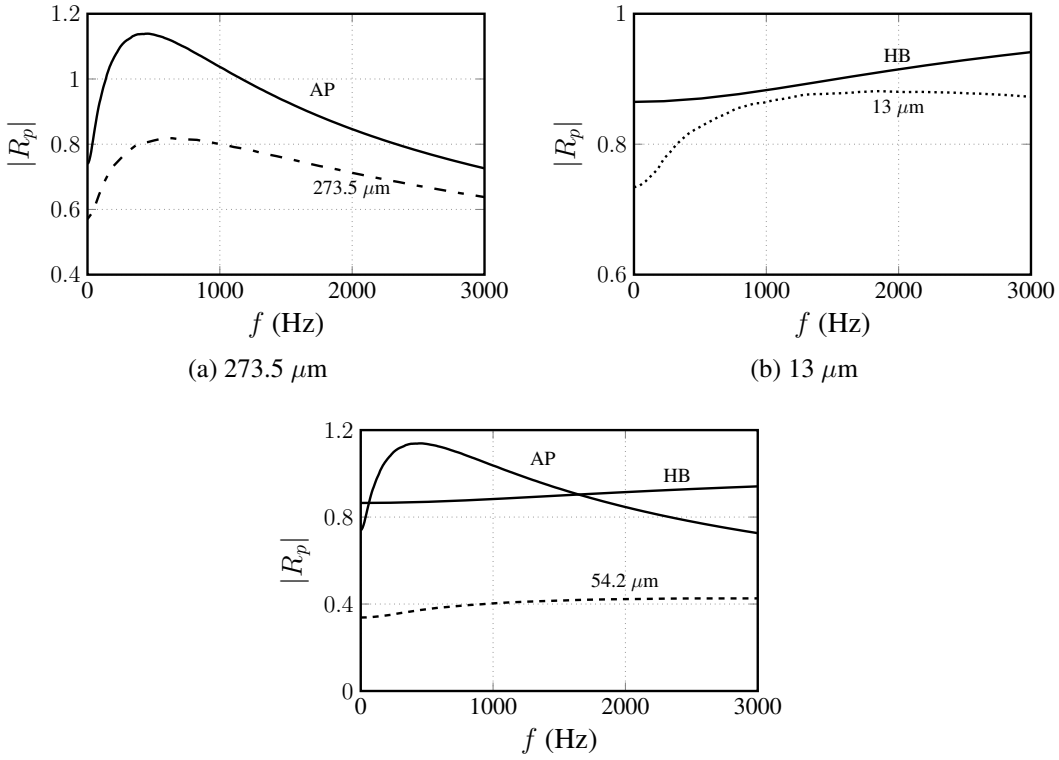

(a) 273.5 μm

(b) 13 μm

(c) 54.2 μm

Figure 3.9: Comparison of frequency response of the select particles of propellant SD-III-18 with that of AP and homogeneous binder (HB).

Along with magnitude of peak frequency response, PSD also affects the frequency at which the peak response occurs. In Fig. 3.8a, it can be seen that peak frequency responses of AP particles of sizes 273.5 and 13 μm occur at lower frequencies compared to a particle of size 54.2 μm. Wide O/F variation in the particles of different size implies that the individual particle burn at very different rates and the corresponding to this each particle has a response peak at its distinct frequency ($f \sim \bar{\dot{r}}^2/\alpha$). At a particular frequency, the overall response becomes a statistical representation of the responses of all particles (Fig. 3.8a). Figure 3.8b shows that peak of $|R_p|/n$ for all particles occurs close to $f_s = 1$ similar to pure AP and homogeneous propellant. The corresponding dimensional frequencies for particles will cover a wide range ($f = f_s \bar{\dot{r}}^2/\alpha$).

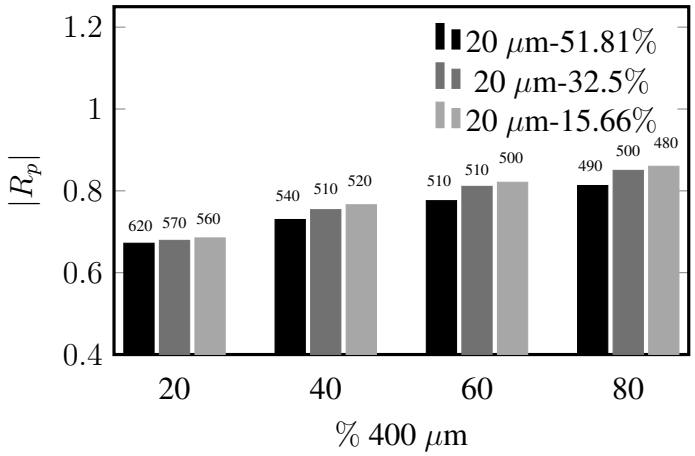

Figure 3.10: Effect of Particle size distribution on overall peak response of the propellant and corresponding frequency which is shown at the top of each bar.

Based on above discussion, different combinations of particle sizes will result in different magnitudes and frequencies of peak response. To further elucidate this, the analysis was carried out for the cases considering nominal sizes of 20, 50 and 400 μm with the total solid loading of 87%. From 87% AP, the proportion of 20 μm nominal size AP particle was fixed and relative proportions of other two nominal sizes were varied. This was repeated for three different fixed proportions of 20μm nominal size. The magnitude of peak frequency response of the different combinations obtained by above procedure are plotted in Fig. 3.10 and corresponding frequencies are shown on the top of each bar. It can be seen that magnitude of peak frequency response increases with increase in the proportion of the particles of 400 μm and there is a shift in the peak of frequency response to the lower frequencies. This is because coarse particles burn with the highest peak response and peaks are observed at lower frequencies (see frequency response of 273.5 μm particle from Fig. 3.8a). At a fixed relative proportion of 50 and 400 μm particles, there is an increase in the peak response with a decrease in the amount of 20 μm size particles and peak response shifts to the lower frequencies. This is due to lower response of 20 μm particles than that of 400 μm particles at all combinations. Thus peak frequency response of the multi-modal composite propellants can be altered by changing the proportion of particular particle size in the propellant.

3.1.4 Effect of solid loading

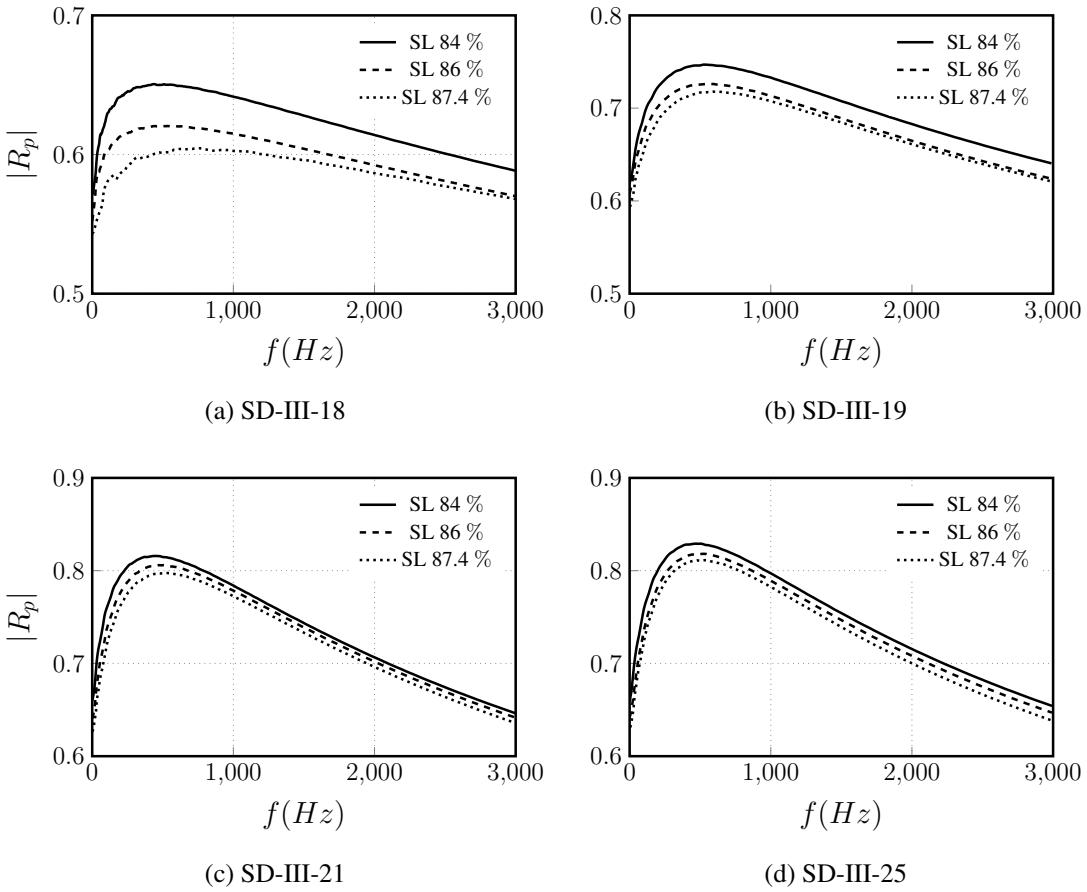

(a) SD-III-18

(b) SD-III-19

(c) SD-III-21

(d) SD-III-25

Figure 3.11: Effect of solid loading on the frequency response of the propellant at pressure of 68.9 atm.

To examine the effect of solid loading, the frequency responses of SD-III-18, SD-III-19, SD-III-21 and SD-III-20 were calculated at an initial temperature of 300 K and mean pressure of 68.9 atm for solid loadings of 84, 86 and 87.4% by keeping same proportion of mean particle sizes in each case. Figure 3.11 shows the magnitude of frequency response, in which, the magnitude at all frequencies is increasing slightly with a decrease in solid loading for all the propellants considered. Reducing solid loading of propellant and keeping the same AP proportion will increase the amount of binder coated over AP particles (see Eq. 2.1). It can be seen from the Figs. 3.3a and 3.3b that there is an increase in the magnitude of frequency response with an increase in the proportion of binder-matrix (only HTPB) for the particles of sizes 25 and 100 μm. Presence of particles of this size range can increase the overall response of the propellant. Notably, all the propellants considered here contain particles of sizes 25 to 100 μm and hence the response is found to increase with a decrease in solid loading for

same mean pressure and initial temperature. Measured response values of propellants reported in Crump (1977) as reported by Beckstead *et al.* (2002) are of the order of one and peak response value decreases from 1.2 to 0.8 for increasing solid loading from 84 to 88 %. These observations are consistent with the current model.

Large changes in mean pressure, initial temperature of propellant, particle size distribution and solid loading have marginally affected the magnitude of peak response for conventional propellant. Mean pressure, initial temperature and particle size distribution mainly affect the frequency of peak response. Owing to a smaller magnitude of response, conventional propellants are stable under all conditions.

3.1.5 Comparison of calculated response with experimentally measured response of Thiokol #10

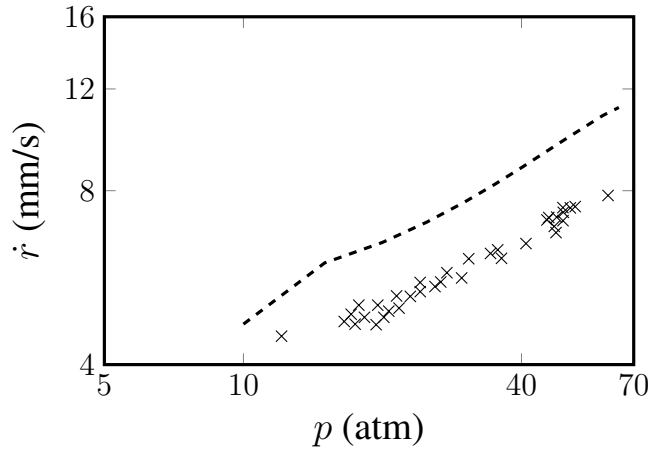

Figure 3.12: Steady state behavior of Thiokol #10. × Experimental, - - - Predicted.

Thiokol #10 is a conventional propellant with AP loading of 88% (200/2-20μm - 55%/33%). The steady state burn rate and frequency response data of Thiokol #10 obtained using an oscillatory burner with an ultrasonic measurement technique are reported in Hafenrichter *et al.* (2004). Thiokol #10 contains DDI as a curative agent in HTPB binder matrix. Notably, predictions for conventional propellants reported in Varunkumar *et al.* (2016) are obtained considering IDPI as a curative agent. The burn rate of 86% solid loaded premixed AP/HTPB (used as a known parameter in calculations) for the case with DDI as a curative agent is chosen as 16 mm/s as against 18 mm/s for the case with IDPI, as DDI is known to reduce the burn rate compared to IPDI (Fredrick Jr, 1988). Predicted results for Thiokol #10 shown in Fig. 3.12 are about 25%

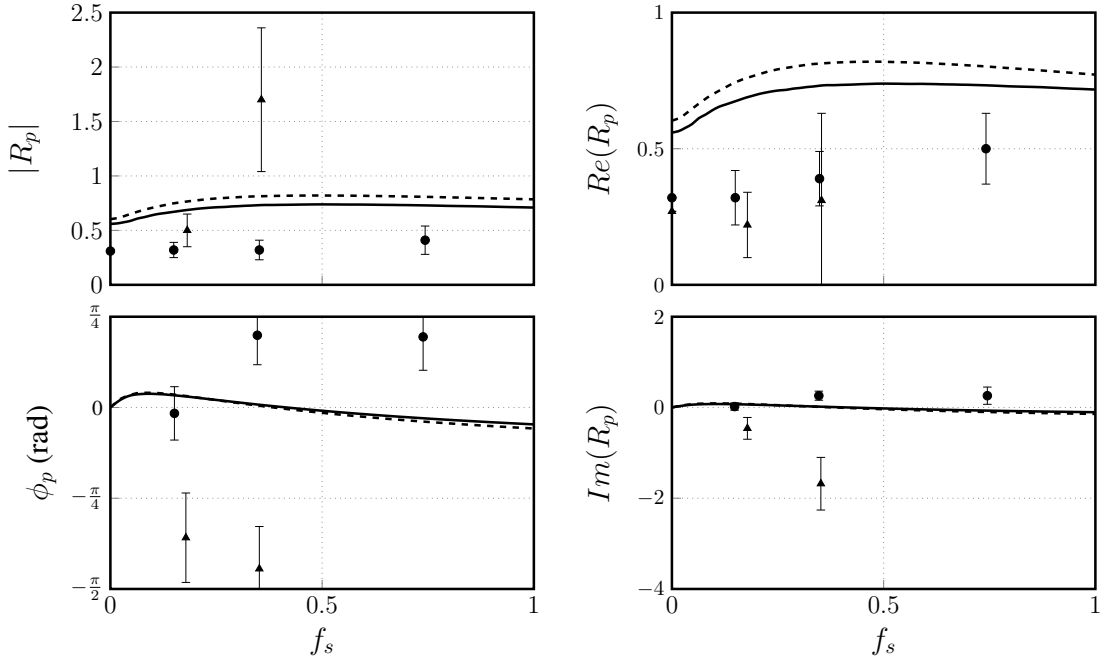

(a) Magnitude of frequency response and phase difference

(b) Real and Imaginary part

Figure 3.13: Comparison of the frequency response of Thiokol #10 predicted at pressures of 19.7 and 49.3 atm with the experimentally measured response using oscillatory burner. • Experimental 19.7 atm, ▲ Experimental 49.3 atm, — Predicted 19.7 atm, - - - Predicted 49.3 atm.

higher at all pressures compared to experimental results from Hafenrichter *et al.* (2004). One reason for this difference is the assumed AP distribution as this information is not available. Also, the decrease in the magnitude of burn rate due to the replacement of IPDI with DDI might be larger than what is assumed here. The experimental and calculated magnitude of frequency response and phase difference along with real and imaginary part of frequency response at mean pressures of 19.7 and 49.3 atm are shown in Fig. 3.13. Error bars shown for experimental results account for uncertainty associated with the calculation of web thickness of propellant from the ultrasonic measurement and uncertainty for a response data increases with frequency. The experimentally measured as well as predicted magnitude of the frequency response of Thiokol #10 are of the order of the propellant index. This is similar to the predictions of earlier discussed conventional propellants. Figure 3.13a shows an increase in the magnitude of response from the pressure of 19.7 to 40.3 atm in case of the experimentally measured and predicted frequency response of Thiokol #10 - similar to SD-III-21 (Fig. 3.2a). This can be due to the presence of richer particles of mean sizes of 200 and 20 μm in Thiokol #10 - similar to SD-III-21 case (see section 3.1.3).

3.2 Propellants with burn rate modifier

Burn rate modifiers are added to a propellant in very small quantities to meet the specific ballistic requirement. Burn rate modifiers can either be the catalyst that enhances the burn rate or inhibitors. Boggs *et al.* (1988) has done an experimental investigation on the effect of additives like oxides of copper and chromium, Iron oxide, MnO_2, TiO_2 and SnO_2 on AP combustion. In general, with the addition of Copper Chromite and Iron oxide, there was an increase in deflagration rate while MnO_2, TiO_2 and SnO_2 decreased the deflagration rate below that of pure AP. Iron oxide (IO), Copper Chromite (CC) and Activated carbon are most commonly used catalysts. Catalyst primarily increases the rate of reaction between the decomposition products of AP and HTPB by reducing the activation energy of gas phase reaction (Handley, 1976). Similarly, instead of reducing the activation energy, inhibitor increases the activation energy thereby reducing the gas phase reaction rate. Titanium dioxide (TiO_2), Lithium fluoride (LiF), etc are common inhibitors. The extent of change in activation energy depends on the concentration of the burn rate modifier in the propellant.

In *HeQu-1D* model, for only AP/HTPB composite propellant, activation energy (E_g) is calculated from the measured burn rate of 86% solid loaded fine AP/HTPB propellant using $\rho_p \dot{r} = \sqrt{\frac{k}{c_p} K_r p^2 ln(1 + \frac{T_f - T_s}{T_s - T_0 - H_s/c_p})}$ and $K_r = A_g exp(-E_g/RT_f)$. Following procedure is used to calculate the activation energy of gas phase reaction with the addition of burn rate modifier. In this case, burn rate of 86% fine AP/HTPB propellant containing $x\%$ burn rate modifier is assumed to be changed by $\pm\Delta\dot{r}$. With a new burn rate of fine AP/HTPB propellant, the activation energy is calculated as stated earlier. The fraction of burn rate modifier will be different for different binder-matrix coated AP particles depending on the diameter of the AP particle. The gas phase activation energy for each AP particle is obtained by considering the linear variation in activation energy between the case with no burn rate modifier and with $x\%$ burn rate modifier. Saturation of activation energy with respect to the amount of burn rate modifier is also taken into consideration. The calculated activation energy is calibrated by comparing the predicted burn rate of propellant in question with the experimentally measured burn rate.

Analysis of frequency response of the propellant affected by the addition of the burn rate modifier will be presented in this section.

3.2.1 Effect of catalyst

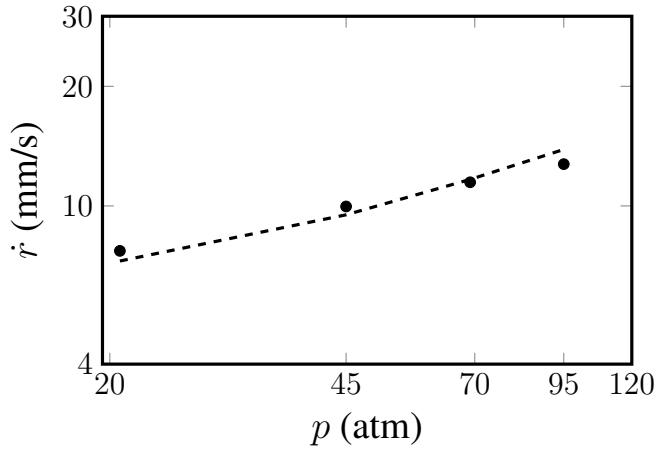

Figure 3.14: Comparison of predicted steady state burn rate with experimentally obtained one for propellant IR0 reported in Blomshield *et al.* (1997). • Experimental, - - - Predicted.

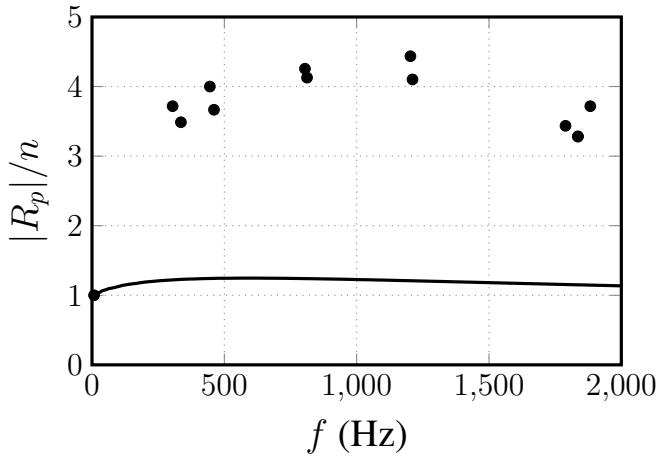

Figure 3.15: Comparison of predicted frequency response with experimentally measured response of propellant IR0 reported in Blomshield *et al.* (1997). • Experimental, — Predicted.

Propellant IR0 which contains 0.5% carbon black is considered for analysis to bring out the effect of the catalyst on the frequency response of the propellant. The frequency response of this propellant measured using T-burner is reported in Blomshield *et al.* (1997). Propellant IR0 is 86% solid loaded AP-HTPB composite propellant comprises of AP particles of mean sizes of 200, 50 and 20 μm. Since fractions of each particle sizes of AP for IR0 were not reported by the author, the proportions of the given particle sizes were fixed based on steady state burn rate (11.43 mm/s) and index (0.33) reported by author at pressure of 68.9 atm. Decrease in activation energy due to the addition of

0.5% carbon black is calculated using the procedure described earlier. In this case, the burn rate of 86% solid loaded AP/HTPB with 2% carbon black was increased by 2 mm/s and corresponding gas phase activation temperature, i.e. E_g/R is calculated as 7531 K. Comparison of predicted burn rate with experimentally measured burn rate is shown in Fig. 3.14. The predicted results are obtained with following AP distribution - 200/50/20 - 60%/16.5%/10%. The magnitude of the frequency response of IR0 is calculated using *UHeQu1-D* framework with modified activation temperature. Comparison of experimentally measured response with the predicted response for propellant IR0 shown in Fig. 3.15 shows a poor agreement. The response measured using T-burner are always found to be on higher side, for instance in case of ultra pure AP as discussed earlier (see Fig. 2.9). Also, an investigation by Perry (1970) shows measured stability margins using T-burner are lower than that obtained from motor firing - implies response values obtained from T-burner are at higher side than that one can obtain from motor firings. Pertaining to reporting of frequency response from experimental measurement techniques, it is of utmost importance to report complete information regarding the propellant composition to the validate predicted response with an experimentally obtained one.

3.2.2 Effect of inhibitor

Propellants Thiokol #4, Thiokol #5, and COM1 are considered for analysis to bring out the effect of the inhibitors on the frequency response of the propellant.

Thiokol #4 and #5

Propellants Thiokol #4 and Thiokol #5 reported in Hafenrichter *et al.* (2004) contain 2% TMO with the following AP distribution - 200μm/20μm - 52%/33%. The difference between Thiokol #4 and Thiokol #5 is a curative agent used - Thiokol #4 contains DDI whereas Thiokol #5 contains IDPI.

Similar to IR0, a framework to calculate frequency response for these propellants remains same as that of conventional propellants except the use of modified activation energy. The activation energy for gas phase with the addition of 2% TMO is calculated by similar procedure described earlier. Here, the burn rate of 86% solid loaded fine

AP/HTPB propellant with 2% TMO was reduced by 2 mm/s for Thikol #4 as well as Thiokol #5 and corresponding gas phase activation temperatures (E_g/R) are 7799 and 8290 K.

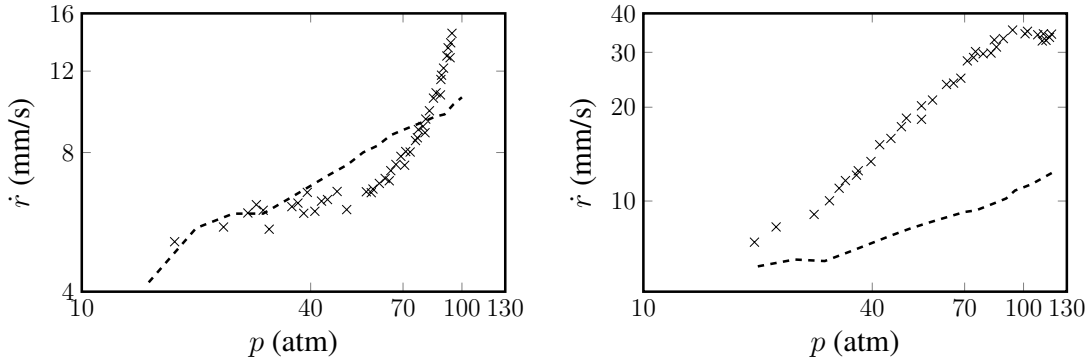

(a) Thiokol #4 (b) Thiokol#5

Figure 3.16: Steady state behaviour of Thiokol #4 and Thiokol #5. × Experimental, - - - Predicted.

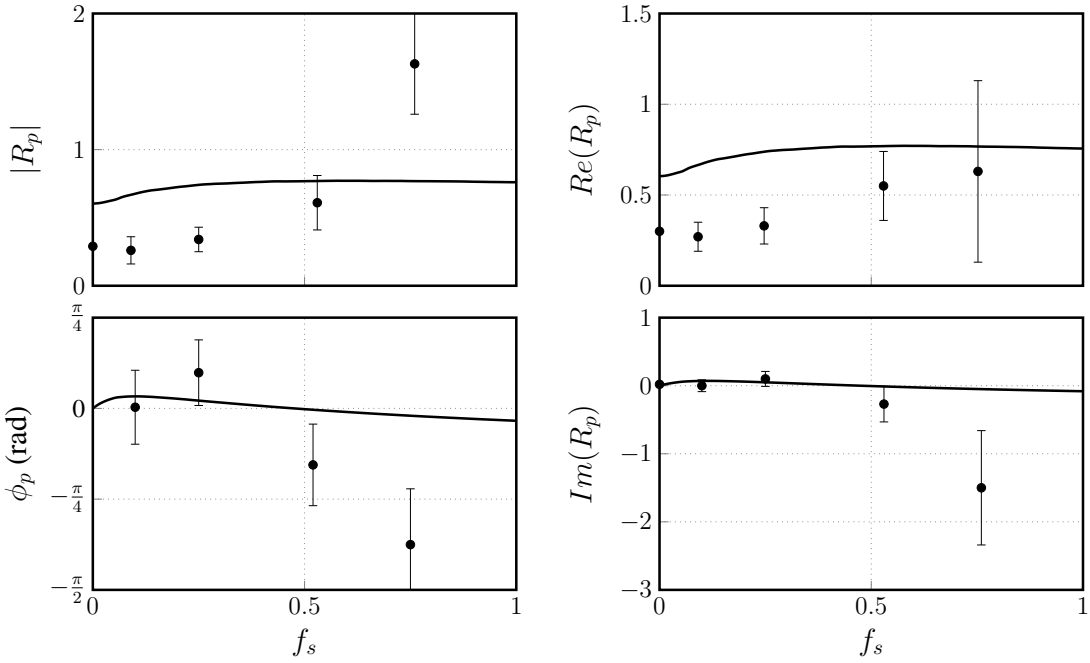

(a) Magnitude of response and phase (b) Real and Imaginary part

Figure 3.17: Comparison of predicted frequency response of Thiokol #4 at pressure of 19.7 atm with experimentally measured response using oscillatory burner. • Experimental, — Predicted.

Predicted steady state burn rates of Thiokol #4 along with experimentally measured burn rates are shown in Fig. 3.16a. Predicted burn rates are close to experimentally measured burn rates in the pressure range of 20 to 40 atm but experimentally measured

burn rates are spread around predicted burn rate data leading to different pressure index. Comparison of predicted response with the experimentally measured response for Thiokol #4 at a pressure of 19.7 atm is shown in Fig. 3.17. Predicted frequency response is higher than the experimentally measured response for frequencies - f_s <0.5. Experimental data show enhancement in the magnitude of the frequency response compared to base propellant Thikol #10 (see Fig. 3.13) at higher frequencies with the addition of TMO. The predicted response does not show this enhancement. A claim of an increase in response at higher frequencies with the addition of TMO is not justifiable owing to following reasons. First, the changes in experimentally measured steady state burn rate and pressure index are not significant compared to Thiokol #10 (Fig. 3.12) with the addition of 2% TMO (especially in the range of pressures at which response is measured). Secondly, the increase in frequency response with the addition of TMO is reported only at higher frequencies where there are increased errors in ultrasonic measurements.

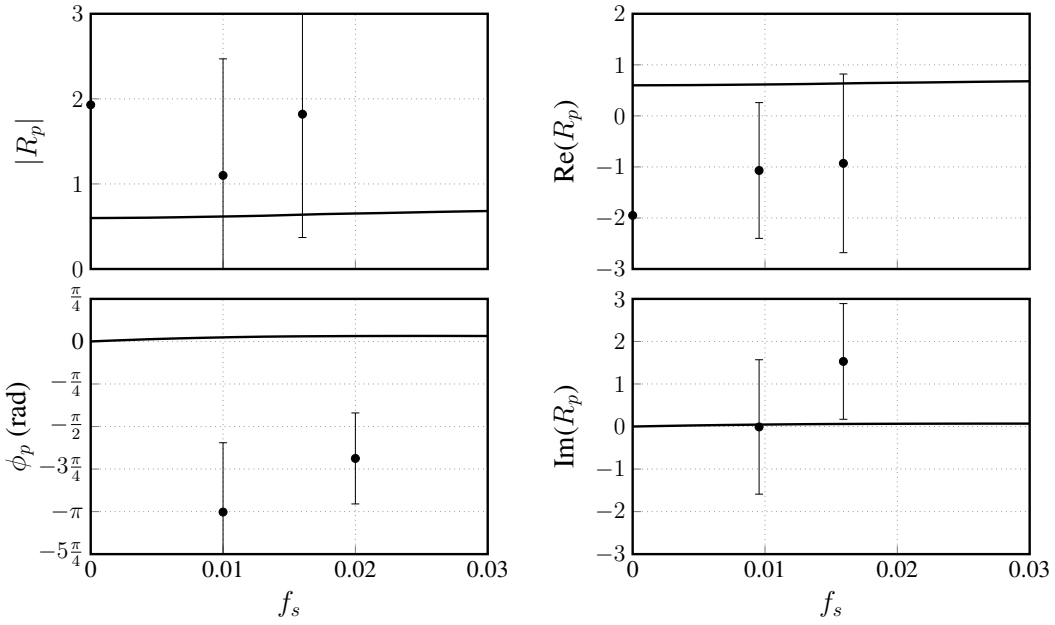

(a) Magnitude of response and phase

(b) Real and Imaginary part

Figure 3.18: Comparison of predicted frequency response of Thiokol #5 at pressure of 118.4 atm with experimentally measured response using oscillatory burner.
- Experimental, — Predicted.

The predicted and experimentally measured burn rates of Thiokol #5 are shown in Fig. 3.16b. Experimental burn rates for Thiokol #5 are very high with the index as high as 2 in spite of not having high fine fractions of AP and containing 2% TMO which is an inhibitor. Predicted as well as an experimentally obtained response for Thiokol #5 at a pressure of 118.4 atm are shown in Fig. 3.23. Frequency response values predicted for

Thiokol #5 excluding zero frequency response are within the error bars provided with experimental results.

Notwithstanding the differences between the predicted and experimental steady state burn rates, the comparison is sought with experimental values of $|R_p|/n$ vs f_s. Figure 3.19 shows a comparison of predicted and experimental $|R_p|/n$ data for Thiokol #10 and Thiokol #4 which closely match at lower frequencies.

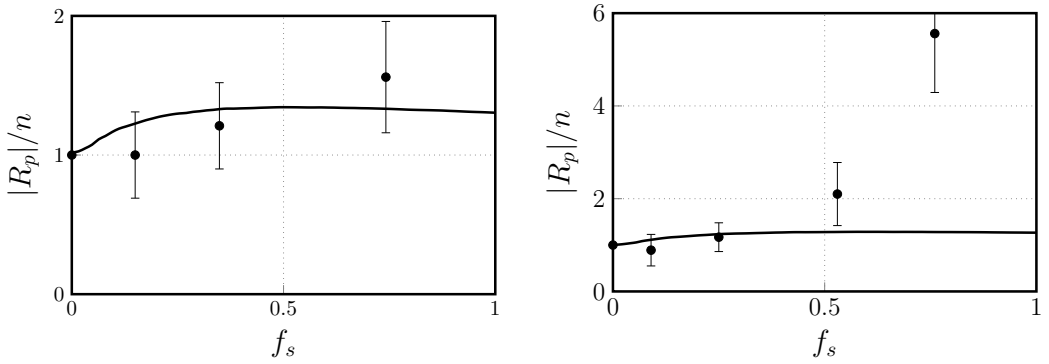

(a) Thiokol #10 (b) Thiokol #4

Figure 3.19: Comparison of predicted frequency response of Thiokol #10 and Thiokol #4 with experimentally measured response using oscillatory burner. Response plotted here is in the for of R_p/n. • Experimental, —Predicted.

COM1

Propellant engineers generally believe that compositions with low index will be relatively stable compared to high index compositions. This is valid in a limited sense - propellants with high AP loading ($\geq$ 84%) and no special additives tend to have frequency response comparable to the pressure index due to the dominance of gas phase fluctuations on burn rate. Therefore while dealing with such propellants in applications, it is reasonable to choose a composition with as low index as possible. The minimum index achievable with only AP and HTPB is about 0.4, but modern applications demand an index lower than 0.3. Such low index can only be achieved with special burn rate suppressing additives, $SrCO_3$ is one of those. Since these additives act by significantly modifying the surface behaviour leading to coverage of AP particle surface by binder melt, it is very important to account for the unsteady dynamics of the melt while determining the stability of rockets employing the propellant. Experimental evidence based on full motor tests clearly shows that the frequency response of these propellants can

be as high as ten times its index (Arvind *et al.*, 2013), a feature not found in high SL AP/HTPB only propellants.

The steady state behaviour of binder melt (statics) is explained using an extension of blocking effect (see Eq. 1.2), which is essentially a thermodynamic/heat transfer based description (Varunkumar *et al.*, 2016). Propellant response calculated after including binder melt effect using this approach in perturbation analysis is shown in Fig. 3.20. It can be seen that blocking effect approach to fluctuations in heat flux feedback because of binder melt dynamics when subjected to perturbation is inadequate to capture frequency response ten times higher than the propellant index.

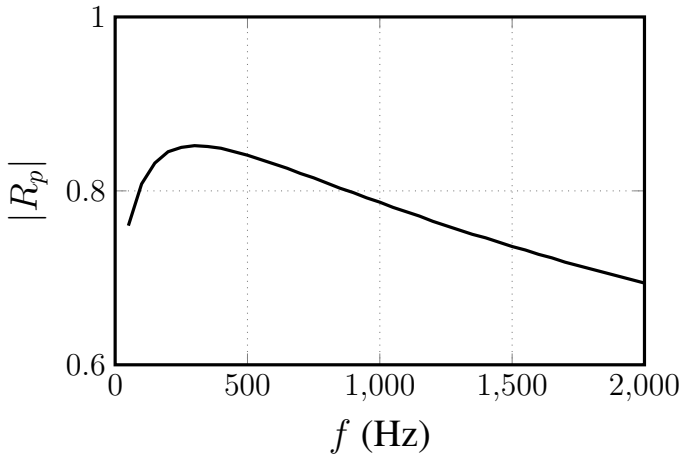

Figure 3.20: Frequency response for COM1 at pressure of 68.9 atm calculated without using extra dynamics.

The unsteady behaviour can be possibly explained by invoking certain mechanical/dynamic aspects, like for instance, fluctuation of melt layer due to pressure oscillations. These additional fluctuations in the area covered by binder melt are brought with the introduction of $fll^{'}$ which is defined as,

$$\frac{f_{ll}^{'}}{\bar{f}_{ll}} = -f_{ll,amp}\frac{p^{'}(f)}{\bar{p}} \tag{3.1}$$

where $f_{ll,amp}$ is a function of frequency. With this, total area covered by liquid layer becomes $f_{ll} = \bar{f}_{ll} + f_{ll}^{'}$ which is obtained using calibrated value of $f_{ll,amp}$. The negative sign in Eq. 3.1 indicates the out-of-phase relationship between the fluctuations in pressure and melt layer on the based on following consideration - there will be a decrease in area covered by liquid layer as pressure starts to increase in a particular cycle of oscillation and vice-versa. This will result in an increase of the amplitude of burn rate

oscillations and hence the frequency response. Due to inadequate experimental data, it is an attempt to model the additional fluctuations in heat flux feedback responsible for the increase in frequency response. Linearizing governing equations in limiting condition of decomposition of $SrCO_3$ happening at the propellant surface, the expression for the frequency response of binder-matrix coated AP particle is derived as follow,

$$R_{p,i} = \frac{2 + \frac{h_d}{1-h_d}\frac{c_1\bar{p}}{g(B_{eff})\bar{f}_{nll}(\bar{H}_s + f_{SC}H_d)} + z_r\left[e_g + \frac{1}{g(B_{eff})}\frac{\bar{T}_{eff}}{\bar{T}_{eff}-\bar{T}_s}\right] + f_{ll,amp}\frac{\bar{f}_{ll}}{\bar{f}_{nll}}}{2 + \frac{\bar{f}_{nll}\theta_{fs,eff}(1-h_d) + A_c sin(2\pi f_s \tau + \phi_c) - e_s h_d - \bar{f}_{nll}(1-h_d)e_s}{\bar{f}_{nll}g(B_{eff})(1-h_d)e_s}} \tag{3.2}$$

The derived expression for frequency response (Eq. 3.2) includes a parameter $f_{ll,amp}$ which can be obtained only by calibration with a known frequency response value. Predictive capability of the derived expression (Eq. 3.2) requires a physics based model for $f_{ll,amp}$. Calibrated frequency function of $f_{ll,amp}$ to obtain peak response of 3 at 250 Hz is shown in Fig. 3.21 and the corresponding frequency response is shown in Fig. 3.22. Frequency response for COM1 is dominated by frequency function of $f_{ll,amp}$ and it is dependent on the value of $\bar{f}_{ll}/\bar{f}_{nll}$ (Eq. 3.2).

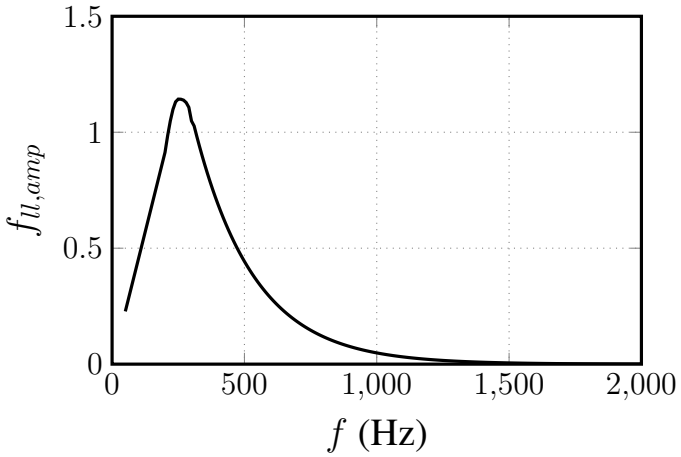

Figure 3.21: Frequency function of $f_{ll,amp}$.

Figures 3.23a and 3.23b show effect of mean pressure and initial temperature on the magnitude of frequency response. Unlike conventional propellants, the magnitude of peak frequency response of COM1 increases with increase in mean pressure. This is because the ratio $\bar{f}_{ll}/\bar{f}_{nll}$ from the expression of frequency response (Eq. 3.2) increases with increase in mean pressure. This result is a likely explanation for some conflicting observations on the pressure dependence of R_p found in literature and it is consistent with the fact that the SRMs are more prone to instability at higher pressure (beyond the effect of reduced damping at higher pressure). There is no significant change in

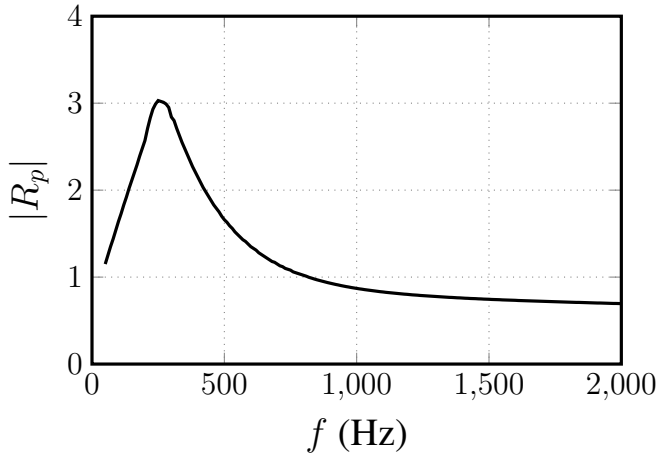

Figure 3.22: Frequency response for COM1 at pressure of 68.9 atm calculated using $f_{ll,amp}$.

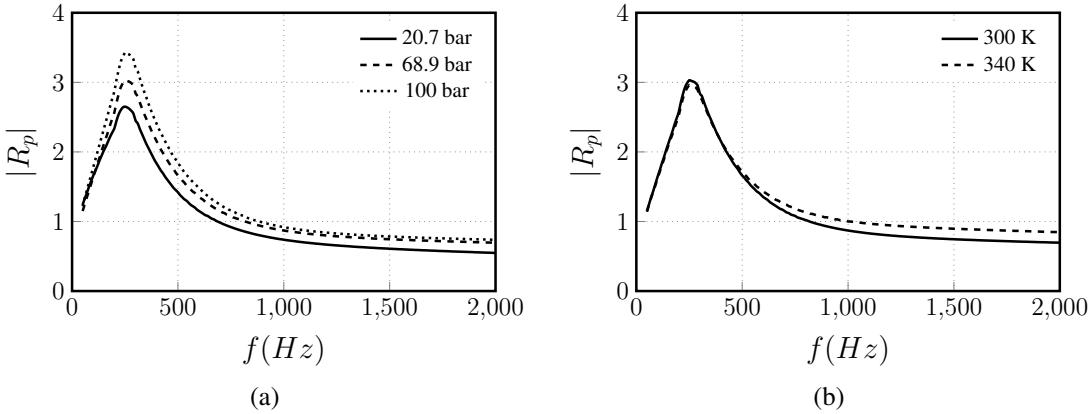

Figure 3.23: Frequency response for COM1 calculated using $f_{ll,amp}$ (a) at pressures of 20.7 and 68.9 atm (b) at initial temperatures of 300 and 340 K.

magnitude of frequency response with change in initial temperature.

3.3 Summary

The frequency response of conventional propellants and propellants with burn rate modifiers have been calculated and analysed using *UHeQu1-D* model. The frequency response of the conventional propellants is found to be of the same order of pressure index which is always less than one. Change in mean pressure, initial temperature, AP particle size distribution and solid loading have a marginal effect on the frequency response of the conventional propellants. This implies the use of conventional propellants will ensure stable motor operations. The predicted frequency response of propellant containing burn rate modifiers like carbon (catalyst) and TMO (inhibitor) were also found to be the same order of the pressure index. In case of propellant COM1, which contain

2.5% $SrCO_3$- an inhibitor, the experimentally measured frequency response is ten times the pressure index. The increased frequency response is explained by introducing fluctuations in binder melt coverage - a possible mechanism of enhancement in frequency response. This led to increase in response with an increase in mean pressure as opposed to the behaviour of conventional propellants. In next chapter, the frequency response is coupled to a simple CFD framework to study the phenomena of linear instability and DC shift in tactical missile SRMs.

CHAPTER 4

Linear Instability and DC shift- CFD study

In this chapter, a CFD framework is presented which simulates the unsteady flow through the port of a side-burning solid rocket motor to study the linear instability and DC shift - phenomena encountered in tactical missile SRMs. Combustion-acoustic coupling in the linear phase is accounted for by a response function formulation in which the burn rate fluctuations are calculated as a product of frequency response and corresponding pressure perturbation amplitude in the frequency domain. At high amplitude pressure oscillation when the propellant is subjected to critical de-pressurisation rate, burn rate fluctuations are calculated using extinction-re-ignition burn rate behaviour shown in Fig. 1.1. By coupling these two frameworks, the motor is shown to exhibit DC shift when a propellant with frequency response ten times the pressure index is used.

4.1 Numerical model

The motor geometry used for the numerical simulation is shown in Fig. 4.1 which can be considered a canonical configuration for studying instability.

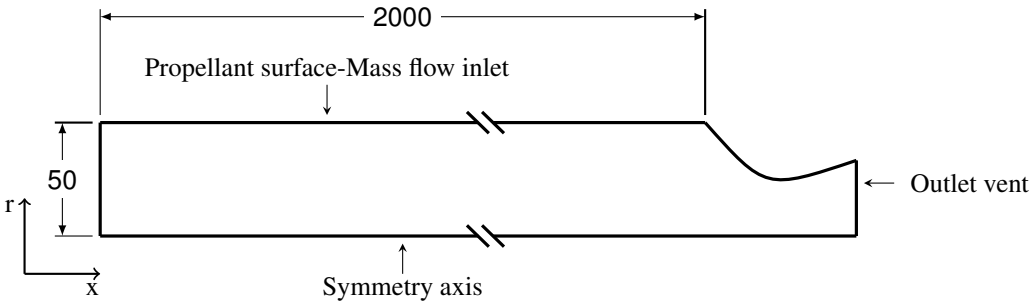

Figure 4.1: Geometry of SRM used in numerical simulations. All Dimensions given are in mm.

The first longitudinal mode ($f = a/2L$) observed in SRMs used in tactical missiles is generally in the range of 200 to 500 Hz corresponding to temperature of 3000 K

(chamber temperature) and a motor length in the range of 1-3 m. Based on this a length of 2 m was chosen here (Fig. 4.1). Simulations were performed for two mean pressures, 70 and 120 atm with a corresponding throat radii of 22.6 and 18.7 mm obtained from steady state mass-balance as given by Eq. 4.1 (assuming lumped burning),

$$\rho_p \dot{r} A_b = \frac{p_c A_t}{c^*} \tag{4.1}$$

where A_b is the propellant surface area, A_t is throat area, $\dot{r}$ is burn rate of propellant expressed as $a(p_c/p_{ref})^n$, p_c is chamber pressure at steady state. For propellant COM1 (see details in section 3.2.2), which is considered here for motor design - the density (ρ_p) is 1664 kg/m^3, burn rate constant (a) at p_{ref} of 70 atm is 7 mm/s, pressure index (n) is 0.3 and characteristic velocity (c^*) is 1535 m/s.

Propellant gasification processes are confined to a thin layer above the solid surface (< 50 μm) and its effect on the port flow dynamics can be accurately simulated by assuming the combustion zone to be infinitely thin. Hence a mass inlet boundary condition is used at the propellant surface, through which gases at 3000 K enter the port. The mass flux along this boundary has two components – a steady and a fluctuating component as shown in Eq. 4.2.

$$\dot{m}_b(x) = \bar{\dot{m}}_b(x) + \dot{m}_b^{'}(x) \tag{4.2}$$

Steady component of mass flux, $\bar{\dot{m}}_b(x)$ is given by,

$$\bar{\dot{m}}_b(x) = \rho_p \bar{\dot{r}}(x) \tag{4.3}$$

Fluctuating component of mass flux is obtained from fluctuating component of burn rate using following procedure. Fluctuating component of burn rate ($r'(x,t)$) can be calculated from the definition of frequency response (Eq. 1.3). Consider a position x on the propellant surface. The static pressure at this point varies with time and is denoted by $p(x,t)$. The mean burn rate is a function of the mean pressure, $\bar{p}(x)$ and given by Eq. 4.3. The fluctuation in pressure, $p^{'}(x,t)$ is decomposed into respective Fourier modes as follows,

$$p^{'}(x,t) = p_1^{'}(x,t) + p_2^{'}(x,t) + p_3^{'}(x,t) \tag{4.4}$$

Only first three modes were considered as amplitudes of higher modes were found to be negligible. Using the definition of frequency response, fluctuations in mass flux can be expressed as,

$$m^{'}(x,t) = \rho_p \frac{\bar{\dot{r}}}{\bar{p}} \sum_{i=1}^{3} R_{p,i} p_i^{'}(x,t) \tag{4.5}$$

The expression to calculate mass flux fluctuations (Eq. 4.5) is in the frequency domain and it is equivalent to convolution in time domain. In this expression, $R_{p,i}$ is the function of frequency and can be expressed in terms of magnitude and phase. The term $p_i^{'}(x,t)$ is the amplitude of the i^{th} modes. The amplitude of different modes are calculated from the Fourier transform of four pressure cycles earlier to the current instant of time. In general magnitude and phase of frequency response are different for different modes. While calculating fluctuating component of mass flux at a given instant of time, the phase difference between burn rate fluctuations and pressure fluctuations is introduced in the definition of $p^{'}(x,t)$. The term $p^{'}(x,t)$ also accounts for the spatial phase difference across the length of the motor chamber. Typical magnitude of frequency response known to cause large amplitude oscillations is 3 to 5 for first mode Arvind *et al.* (2013). The propellant has peak frequency response in the range of 200 to 300 Hz, corresponding to the conduction time scale ($\alpha/\bar{\dot{r}}^2$) of a few milliseconds. The response values for higher modes are lower as the trend follows an inverted bell curve typical forms of which are given in the previous chapter. For the chosen length of 2 m (see Fig. 4.1) and 1095 m/s sound speed, the first three longitudinal modes will have the following frequencies - 270 Hz (fundamental), 540 Hz (first harmonic) and 810 Hz (second harmonic). Two sets of frequency response, showing magnitude and phase corresponding to first three longitudinal modes of motor considered (mode I - 270 Hz, mode II - 540 Hz, mode III - 810 Hz), used in current work are listed in Table 4.1.

Table 4.1: Values of magnitude and phase of frequency response for I, II and III modes used in the calculations.

Case	Magnitude			Phase (^{o})		
	I (270 Hz)	II (540 Hz)	III (810 Hz)	I (270 Hz)	II (540 Hz)	III (810 Hz)
1	3	1.5	1	0	-15	0
2	5	3.3	3	0	-15	0

The flow of combustion products through the chamber is treated as inviscid, axisymmetric ideal gas flow. Although actual flow is viscid and turbulent, the effect of

turbulence on the longitudinal turbulent mode can be ignored as the length scales over which the turbulent flows interact with the mean flow are very small (less than the port diameter of motor) compared to the wavelength of the longitudinal wave acoustic waves (few meters). All calculations are performed using ANSYS Fluent® by axisymmetric Euler equation solver. Compatibility of the fluent solver to capture standing waves was tested by Varunkumar and Mukunda (2013). It is reported that at least second order accurate temporal and spatial discretisation is required to capture the standing waves without any numerical dissipation. Steady state solutions were obtained for different grid sizes for the motors designed at 70 and 120 atm (cases used in further analysis). Results for grid independent study carried out for steady state solution at 120 atm are shown in Fig. 4.2.

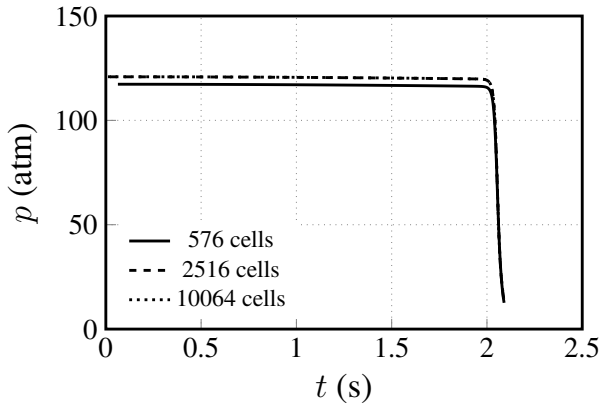

Figure 4.2: Steady state pressure along the axis of motor considered (Fig. 4.1) for different grid sizes.

Steady state solution from optimum grid size was used as an initial condition to carry out the unsteady analysis by introducing perturbations. Time step independence studies were carried out and a time step of 1×10^{-5} s was chosen such that it accurately captured the growth of fundamental and harmonics.

4.2 Decay rate

Nozzle damping and flow turning losses are the dominant decay mechanisms in an SRM using non-aluminized propellants. A detail description of damping mechanisms can be found in De Luca and Summerfield (1992); Guéry (2004); Williams (1965). Nozzle damping is a loss of acoustic energy because of partial reflection of the acoustic wave

at the nozzle end. It is most dominant damping mechanism for the longitudinal mode of oscillation. Apart from this, flow turning losses are important whenever acoustic velocity is parallel to the burning surface (De Luca and Summerfield, 1992). Flow turning loss is acoustic energy lost in doing work on the combustion product entering radially in the chamber to turn them into the axially oscillating flow. Analytical expression of nozzle damping and flow turning losses are reported in Guéry (2004) as,

$$\alpha_{ND} = \frac{2V_{inj}}{R}; \quad \alpha_{FT} = \frac{V_{inj}}{R} \tag{4.6}$$

where, V_{inj} is the velocity of injection of the gases from the propellant surface and R is the port radius. With the increase in motor mean pressure the V_{inj} decreases leading to a decrease in damping and hence the stability margin. Experimental results from Blomshield *et al.* (1997) are consistent with this expectation – motors are more prone to instability at higher pressures.

The framework used here is capable of capturing decay of the acoustic wave due to nozzle damping and flow-turning losses as these damping mechanisms are inviscid. To calculate the decay rate (α_{damp}) of the acoustic waves, the simulation was carried out assuming quasi-static propellant response, as in Eq. 4.3. With this, a decaying pressure fluctuations time traces obtained at the head end of the motor at mean pressures of 70 and 120 atm are shown in Fig. 4.3. The phase difference of 180^o was obtained between head and aft end pressure wave. Table 4.2 shows a comparison of decay rate obtained from CFD calculations at mean pressures of 70 and 120 atm with the decay rate calculated using analytical expressions (Eq. 4.6). Total decay rate obtained from CFD calculation matches with the sum of decay rate from nozzle damping and flow turning losses. This validates the use of CFD to solve flow through the port of SRM which is considered for current analysis.

Table 4.2: Total damping coefficient from CFD calculations and Analytical formula.

P	V_{inj}	$\alpha_{total}(s^{-1})$	
(MPa)	(m/s)	CFD	$3V_{inj}/R$
70	1.64	91	94
120	1.13	68	65

To see the effect of the amplitude of pressure oscillations on the decay rate, calcu-

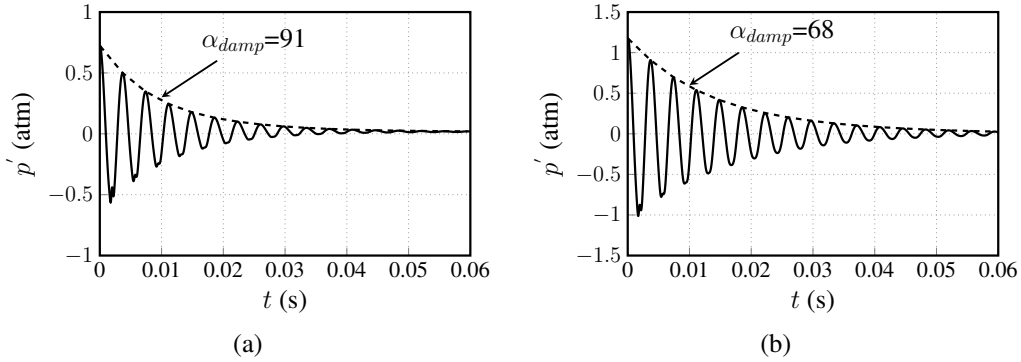

Figure 4.3: Pressure-time traces at the head end with exponential decay fit (a) at 70 atm (b) at 120 atm.

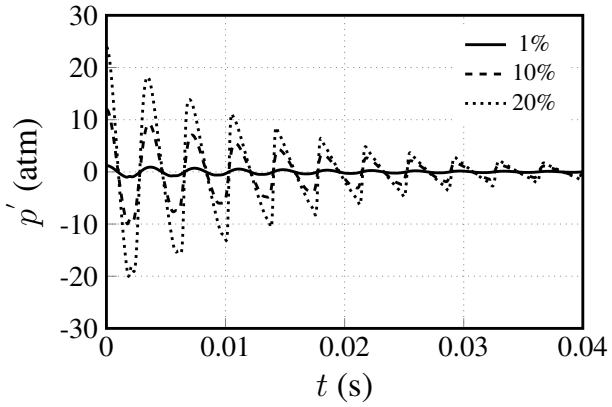

Figure 4.4: Pressure fluctuations time traces at the head end of the motor and mean pressure of 120 atm for initial perturbations of 1%, 10% and 20%.

lations are performed for the initial amplitudes of 1%, 10% and 20%. Pressure fluctuations time traces at the head end of the motor and mean pressure of 120 atm for all three cases are shown in Fig. 4.4. It can be observed that decay rate become amplitude dependent at an amplitude of as high as 20%. All the calculations showing linear instability and DC shift in subsequent sections are performed with initial perturbation of 1% in mean pressure.

4.3 Linear instability

Numerical simulation was carried out by adding combustion acoustic coupling in the form of fluctuations in mass flux as defined by Eq. 4.5 in the boundary condition to the motor chamber. Pressure time traces were obtained for the motor running at pressures of 70 and 120 atm. Figures 4.5 and 4.6 show exponential growth of acoustic wave at the head end of the motor for the frequency response values shown in Table 4.1 for case

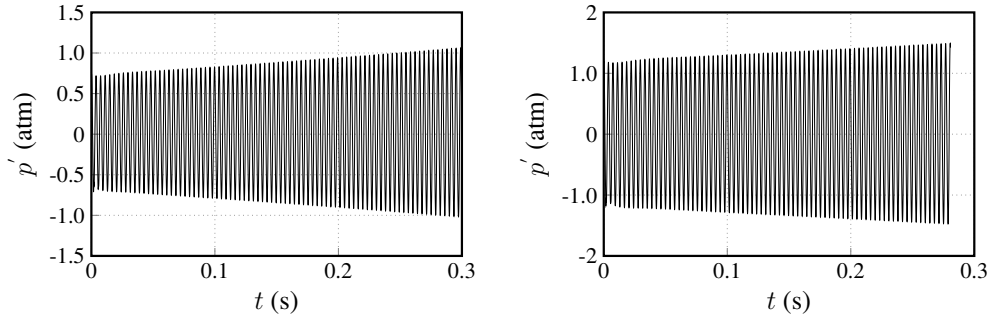

(a) (b)

Figure 4.5: Pressure fluctuations time traces at head end of the motor at mean pressures of (a) 70 and (b) 120 atm for case 1.

1 and case 2, respectively. Net growth rate, $\alpha_{net} = \alpha_{prop} - \alpha_{damp}$, calculated during initial exponential growth for both cases, is shown in Fig. 4.7. For case 1 (response of 3 at mode I) at 120 atm, α_{prop} slightly exceeded α_{damp} causing the net growth of the acoustic wave.

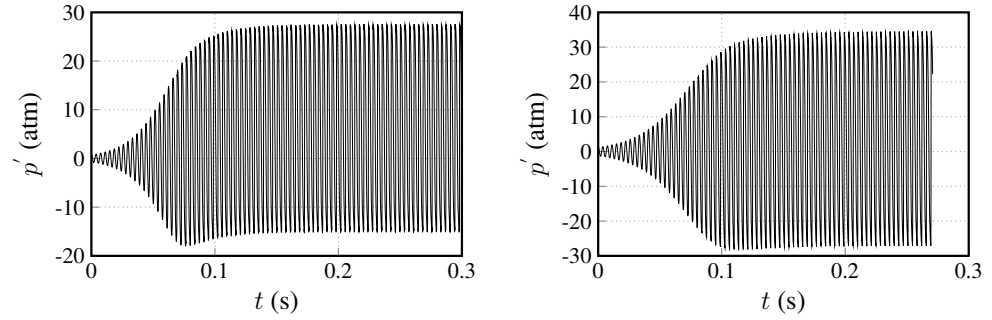

(a) (b)

Figure 4.6: Pressure fluctuations time traces at head end of the motor at mean pressures of (a)70 and (b) 120 atm for case 2.

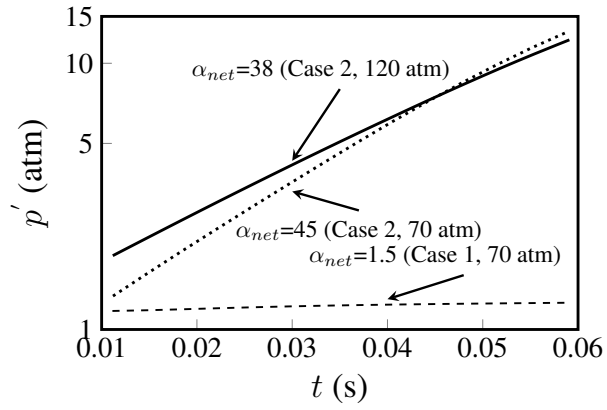

Figure 4.7: Growth rate of pressure wave shown in Figs. 4.5b, 4.6a and 4.6b.

The transition of exponential growth into the limit cycle is obtained for case 2 (re-

sponse of 5 at I mode) within 0.3 s (Fig. 4.6). It can be seen in Fig. 4.7 that net growth rate with the response of 5 is higher than that with the response of 3, as expected.

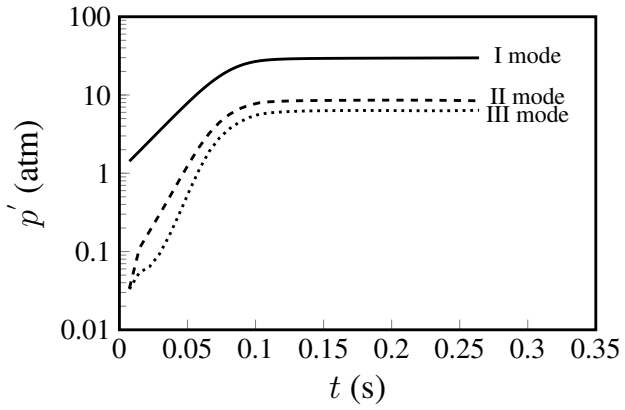

Figure 4.8: Modal analysis of pressure fluctuations time trace shown in Fig. 4.6b.

Modal analysis of pressure wave which is shown in Fig. 4.6b is presented in Fig. 4.8. All three modes can be seen to grow leading to typical N-shaped wave formed at the limit cycle. While growth mechanism is still linear, a limit cycle is obtained. This indicates that beyond a certain amplitude nonlinear gas-dynamic processes begin to play a role. This could be a combination of the following two mechanisms - 1) the damping rates could have become amplitude dependent and 2) coupling of the fundamental mode with higher harmonics leading beyond a certain amplitude leading to transfer of energy across modes (as can be seen from Fig 4.8). This is a general feature in the time evolution of self-excited unstable systems, see for instance work of Li and Zhao (2013).

4.4 DC shift

Pressure time traces obtained in the previous section using the response function approach (Figs. 4.6, 4.7 and 4.8) show exponential growth transitioning into limit cycle without any sign of DC shift. High amplitude de-pressurisation induced extinction-re-ignition cycle can be a possible cause of DC shift. As shown in Varunkumar and Mukunda (2013) this behaviour is connected to the extinction of propellant when subjected to a de-pressurisation rate exceeding the critical value resulting in burn rate behaviour shown in Fig. 1.1. To test this hypothesis, the following modified procedure was used to calculate burn rate fluctuation. Until the point when the de-pressurisation rate is greater than the critical value, the burn rate is calculated using frequency re-

sponse approach explained earlier. Once the de-pressurisation rates decrease below the critical value, the burn rate is assumed to follow the behaviour shown in Fig. 1.1. In the case presented in the previous section (Fig. 4.6) de-pressurisation rate as high as 20 atm/ms is achieved during the limit cycle. Critical de-pressurisation rates are usually in the range of 2 to 8 atm/ms (Strand *et al.*, 1972) which suggest the implementation of the effect of de-pressurisation on the propellant burning is essential. Quenching followed by rising of burn rate to 100 mm/s for the critical de-pressurisation rate of 8 atm/ms was implemented in the boundary condition. Pressure time trace using this modified procedure with a mean pressure of 120 atm is shown in Fig. 4.9 and clearly, shows a shift in mean, i.e. DC shift for the case with critical depressurisation rate of 8 atm/ms (Fig. 4.9a).

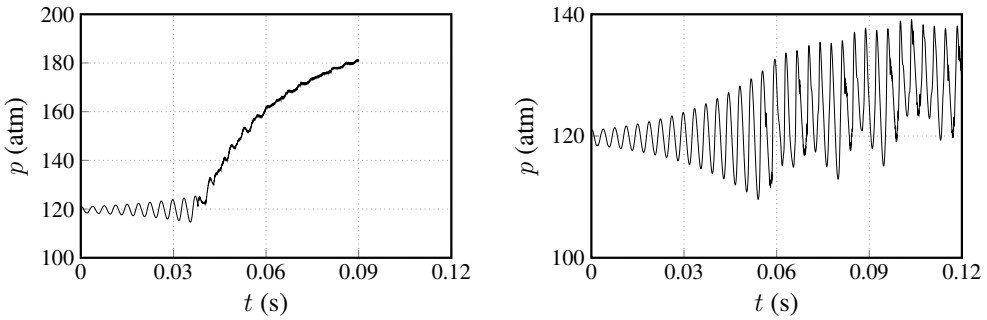

Figure 4.9: Pressure fluctuations time traces at head end of the motor at mean pressure of 120 atm for critical de-pressurisation rates of (a)8 atm/ms and (b) 15 atm/ms.

The current results are found to agree with the experimental results in Blomshield *et al.* (1997) qualitatively - for instance, increase in mean pressure by around 30% due to DC shift is captured. The quantitative comparison requires much more information on the propellant composition, etc. and frequency response values, which is generally not available.

As the standing wave forms in the motor chamber with a crest at the head end and trough at the aft end or vice versa (changes with time), one-half of the propellant grain burns under pressurisation while another half under de-pressurisation. The amplitude of oscillation varies as per spatial variation in standing wave. This creates different de-pressurisation rates in different sections of propellant at a particular instant of time. For accumulation of enough mass to cause DC shift a large section of the propellant

has to undergo extinction. This is indeed the case with a critical de-pressurisation rate of 8 atm/ms. With 15 atm/ms for instance (Fig. 4.9b) the magnitude of DC shift is not significant and the p-t trace is close to that of a limit cycle. These aspects require further exploration.

4.5 Summary

A CFD framework is developed to analyse the stability of solid rocket motor for a known frequency response of the propellant. The framework is validated by showing that numerically obtained decay rate closely matches with that calculated from analytical expression. The necessity to account for the effect of high amplitude pressure oscillations on propellant deflagration to capture DC shift is brought out. Implementation of extinction followed by very high burn rate after a critical de-pressurisation, which can be one of the possible causes of DC shift, is shown to cause a shift in mean pressure, i.e. DC shift. Further work is required to reproduce high amplitude oscillations post DC shift and effect of critical de-pressurisation rate on the extent of DC shift.

CHAPTER 5

Conclusion and Future Work

This thesis has presented a framework to study the combustion-acoustic coupling in tactical missile SRMs which uses AP/HTPB based composite propellants. It has opened up the possibility to obtain the stability margins for tactical missile SRMs with less computational efforts using (1) *UHeQu1-D* model which calculates the frequency response of the multi-modal composite propellants and (2) a computational framework which couples propellant combustion to the port flow of tactical missile SRMs.

The *UHeQu1-D* model was developed by extending the *HeQu1-D* framework to unsteady regime using linear perturbation analysis. The linear perturbation analysis of serial burning expression has resulted in the expression for the frequency response of the multi-modal propellant in terms of the frequency response of binder-matrix coated AP particles. The analytical expression of the frequency response of binder-matrix coated AP particle was obtained from the linear perturbation analysis of *quasi 1-D* burn rate model for binder-matrix coated AP particle. This expression contains consistent parameters such that it satisfies $R_p \to n$ as $f \to 0$. Derived expression of the frequency response looks similar to the expression of a well understood steady parameter, i.e., the pressure index. Except A_c and ϕ_c which appears in the expression of frequency response, all other terms appearing in both expressions are steady-state quantities. A_c and ϕ_c characterise the unsteadiness in condensed phase. Calculated frequency responses of the binder-matrix coated AP particles were found to have peak response of the same order as the burn rate index (n) and peak response occurs at frequency corresponding to the conduction time scale ($\alpha/\bar{\dot{r}}^2$), i.e., when expressed as R_p/n vs $f_s = f\alpha/\bar{\dot{r}}^2$, the peak magnitude will be $\mathcal{O}(1)$ and will occur close to $f_s = 1$. The frequency response of the convention propellant (only AP/HTPB) namely SD-III-18, SD-III-19, SD-III-21 and SD-III-25 was calculated using *UHeQu1-D* model and analysis was carried out to study the effect of mean pressure, initial temperature, AP particle distribution and solid loading on the frequency response. Following are the well-known results from the literature verified by the current theory:

1. The frequency response of conventional propellants is of the same order as the burn rate index, i.e. $R_p \sim n$.
2. In general, there is a marginal decrease in the magnitude of the peak frequency response with an increase in mean pressure and initial propellant temperature.
3. Particle size distribution affects magnitude, as well as the frequency of peak response and propellants containing a large fraction of coarse particles, burn with higher frequency response.
4. The decrease in solid loading which makes the propellants burn slower results in an increase in frequency response.

With the analysis carried out, it is concluded that conventional propellants are well behaved, that is, as they are having a frequency response of the order of the pressure index with respect to change in any parameter and pressure index less than one; tactical missile SRMs using these propellants will be stable.

The *UHeQu1-D* model was also extended to account for the effect of burn rate modifier which can be either catalyst or inhibitors. Similar response behaviour as that of conventional propellants has been observed in case of propellants containing carbon black (catalyst) and TMO (inhibitor), i.e. $R_p \sim n$. Propellant containing inhibitor like $SrCO_3$ is known to burn with the magnitude of response ten times the pressure index of the propellant from earlier experimental results. $SrCO_3$ is hypothesised to be the cause of the binder melt flow over the AP particle surface which lowers down the pressure index to 0.3. In this case, the *UHeQu1-D* model was extended to account for thermo-chemical and heat flux shielding effects of binder-melt flow. A fluctuation in binder melt coverage was introduced to explain the increase in R_p over the conventional propellants with the addition of 2.5% $SrCO_3$. The important result brought out with current modelling of binder melt flow is the increase in frequency response with an increase in mean pressure. This is in contrast with conventional propellant where response decreases with increase in pressure and is a likely explanation for some conflicting results for frequency response - mean pressure trend found in the literature. Indeed, in the absence of adequate experimental measurements, this was an attempt to model the additional fluctuations in heat flux feedback responsible for the increase in frequency response. A physics-based model to account for fluctuations in binder melt coverage on the basis of the mechanical behaviour of the binder melt with respect to oscillating pressure is left for future work. More experimental results are required to check the finer aspects of the developed framework.

While the general trends of frequency response with respect to different parameters agree with the experimental data available in the literature, the quantitative comparison of predicted response with experimental response shows poor agreement. The frequency response measured using T-burner is found to be always on the higher side of predicted response. There is lack of agreement at higher frequencies with frequency response measured using oscillatory burner by ultrasonic technique due to increased errors at higher frequencies. Given that there are known issues with T-burner and oscillatory burner techniques, there is a need for more accurate techniques for frequency response measurement to validate the theory. A possible alternative is outlined in Varunkumar and Mukunda (2017).

A CFD framework is developed to couple propellant response (from *UHeQu1-D* model) to port gas dynamics to analyse the stability of tactical missile SRMs. This framework is validated by showing that numerically obtained decay rate closely matches with that calculated from analytical expression. With linear combustion-acoustic coupling, exponential growth of pressure wave has been found to transform into a limit cycle with a typical N-shaped wave and no DC shift. This is attributed to a combination of two mechanisms at high amplitude pressure oscillation 1) amplitude-dependent damping and 2) coupling of the fundamental mode with higher harmonics leading to transfer of energy across modes. The necessity to account for the effect of high amplitude pressure oscillations on propellant deflagration to capture DC shift was brought out. Implementation of extinction followed by very high burn rate after a critical depressurisation has been shown to be a possible cause of the shift in mean pressure, i.e. DC shift. The magnitude of DC shift was higher in case of critical de-pressurisation of 8 amt/ms than 15 atm/ms. This aspect as well as to reproduce high amplitude oscillations post DC shift require further exploration. There are multiple perspectives on the origin of the DC shift in literature and the current work adds one more candidate based on depressurisation-quenched-re-ignition to this list. In reality, it is possible that some combination of these aspects could be responsible for DC shift.

The contributions of the thesis are best summarised in the following page.

Contributions of the thesis

$$R_{p,i} = \frac{2+\frac{h_d}{1-h_d}\frac{c_1\bar{p}}{g(B_{eff})\bar{f}_{nll}(\bar{H}_s+f_{SC}H_d)}+z_r\left[e_g+\frac{1}{g(B_{eff})}\frac{\bar{T}_{eff}}{\bar{T}_{eff}-\bar{T}_s}\right]+f_{ll,amp}\frac{\bar{f}_{ll}}{\bar{f}_{nll}}}{2+\frac{\bar{f}_{nll}\theta_{fs,eff}(1-h_d)+A_c sin(2\pi f_s\tau+\phi_c)-e_s h_d-\bar{f}_{nll}(1-h_d)e_s}{\bar{f}_{nll}g(B_{eff})(1-h_d)e_s}}$$

Frequency response of binder matrix coated AP particle

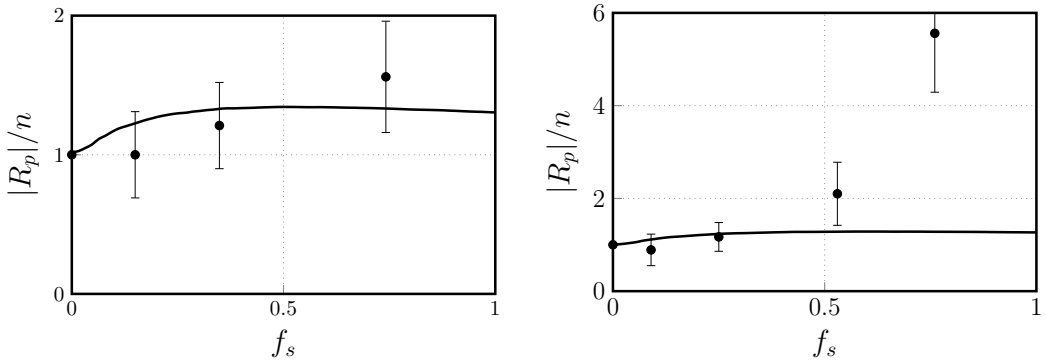

Thiokol #10 Thiokol #4

Comparison of calculated frequency response *UHeQu1-D* with experimentally measured frequency response

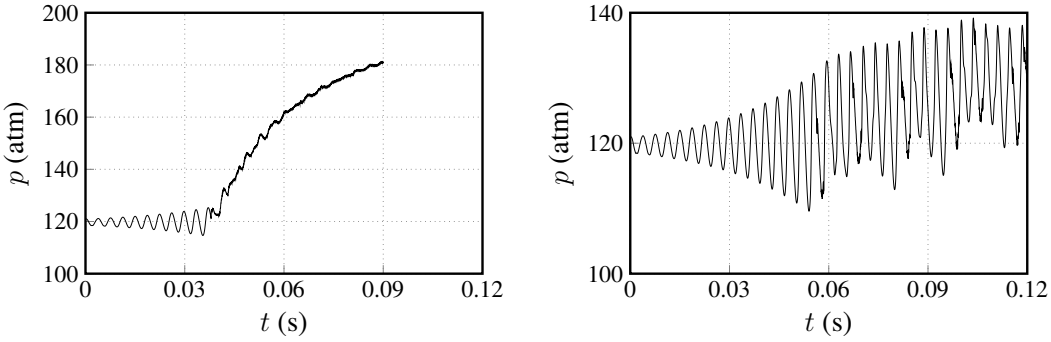

DC shift obtained for critical de-pressurisation rates of 8 atm/ms (left) and 15 atm/ms (right)

APPENDIX A

Perturbation Analysis

A.1 Derivation of Pressure index and Frequency response of Composite propellant

Pressure index for binder-matrix coated AP particle is given by Eq. A.1

$$n_i = \left(\frac{\partial ln(\dot{r}_i)}{\partial ln(p)} \right)_{T_0=c} \tag{A.1}$$

Burn rate of propellant is calculated from burn rate of each binder-matrix coated AP particle using serial burning approach as follow,

$$\dot{r} = \left[\sum_i \frac{l_i}{\dot{r}_i} \right]^{-1} \tag{A.2}$$

For differential change in pressure, dp, burn rate changes as

$$\dot{r} + d\dot{r},\ \dot{r}_i + d\dot{r}_i$$

and propellant burn rate can be expressed as,

$$\frac{1}{\dot{r} + d\dot{r}} = \sum_i \frac{l_i}{\dot{r}_i + d\dot{r}_i} \tag{A.3}$$

$$1 - \frac{d\dot{r}}{r} = r \sum_i \frac{l_i}{\dot{r}_i} \left(1 - \frac{d\dot{r}_i}{\dot{r}_i} \right) \tag{A.4}$$

$$1 - \frac{d\dot{r}}{r} = r \sum_i \frac{l_i}{\dot{r}_i} - r \sum_i \frac{l_i}{\dot{r}_i} \frac{d\dot{r}_i}{\dot{r}_i} \tag{A.5}$$

$$dln(\dot{r}) = \dot{r} \sum_i \frac{l_i}{\dot{r}_i} dln(\dot{r}_i) \tag{A.6}$$

Dividing both side by $dln(p)$,

$$\frac{dln(\dot{r})}{dln(p)} = \dot{r} \sum_i \frac{l_i}{\dot{r}_i} \frac{dln(\dot{r}_i)}{dln(p)} \tag{A.7}$$

or

$$\left(\frac{\partial ln(\dot{r})}{\partial ln(p)}\right)_{T_0=c} = \dot{r} \sum_i \frac{l_i}{\dot{r}_i} \left(\frac{\partial ln(\dot{r}_i)}{\partial ln(p)}\right)_{T_0=c} \tag{A.8}$$

Pressure index of propellant is given by,

$$n = \dot{r} \sum_i \frac{l_i}{\dot{r}_i} n_i \tag{A.9}$$

Frequency response for binder-matrix coated AP particle is given by Eq. A.10,

$$R_{p,i} = \frac{\dot{r}_i{}'/\bar{\dot{r}}_i}{p'/\bar{p}} \tag{A.10}$$

Introducing the decomposition,

$$\dot{r}_i = \bar{\dot{r}}_i + \dot{r}_i{}', \; \dot{r} = \bar{\dot{r}} + \dot{r}'$$

Eq. A.2 becomes,

$$\frac{1}{\bar{\dot{r}} + \dot{r}'} = \sum_i \frac{l_i}{\bar{\dot{r}}_i + \dot{r}_i'} \tag{A.11}$$

$$\frac{1}{1 + \dot{r}'/\bar{\dot{r}}} = \bar{\dot{r}} \sum_i \frac{l_i}{\bar{\dot{r}}_i} \frac{1}{1 + \dot{r}_i'/\bar{\dot{r}}_i} \tag{A.12}$$

$$c1 - \frac{\dot{r}'}{\bar{\dot{r}}} = \bar{\dot{r}} \sum_i \frac{l_i}{\bar{\dot{r}}_i} - \bar{\dot{r}} \sum \frac{l_i}{\bar{\dot{r}}_i} \frac{\dot{r}_i'}{\bar{\dot{r}}_i} \tag{A.13}$$

$$\frac{\dot{r}'}{\bar{\dot{r}}} = \bar{\dot{r}} \sum_i \frac{l_i}{\bar{\dot{r}}_i} \frac{\dot{r}_i}{\bar{\dot{r}}_i} \tag{A.14}$$

Using Eq. A.14 and the definition of frequency response ($R_{p,i}$) of binder-matrix coated AP particle of diameter, d_i (Eq. A.10), the frequency response of propellant can be expressed in terms of frequency response of binder-matrix coated AP particles as shown in Eq. A.15.

$$R_p = \frac{\dot{r}'/\bar{\dot{r}}}{p'/\bar{p}} = \bar{\dot{r}} \sum_i \frac{l_i}{\bar{\dot{r}}_i} R_{p,i} \tag{A.15}$$

A.2 Perturbation Analysis of AP/binder-matrix burn rate equations

Surface heat balance equation for pure AP or homogeneous propellant is given by Eq. A.16

$$\rho_p \bar{\dot{r}} c_p (\bar{T}_s - T_0)(1 + A_c \epsilon_T \sin(2\pi f_s \tau + \phi_c)) = \rho_p \dot{r} H_s + \frac{\rho_p \dot{r} c_p (T_f - T_s)}{\xi^* - 1} \tag{A.16}$$

Under steady conditions, Eq. A.16 takes the form given in Eq. A.17.

$$\rho_p \bar{\dot{r}} c_p (\bar{T}_s - T_0) = \rho_p \bar{\dot{r}} \bar{H}_s + \frac{\rho_p \bar{\dot{r}} c_p (T_f - \bar{T}_s)}{\bar{\xi}^* - 1} \tag{A.17}$$

Subtracting Eq. A.17 from Eq. A.16 and using linearized form of fluctuating quantities,

$$\begin{aligned} \rho_p \bar{\dot{r}} c_p (\bar{T}_s - T_0)(A_c \epsilon_T \sin(2\pi f_s \tau + \phi_c)) &= \rho_p (\bar{H}_s \dot{r}^{'} + \bar{\dot{r}} H_s^{'}) \\ &+ \frac{\rho_p \bar{\dot{r}} c_p (T_f - \bar{T}_s)}{\bar{\xi}^* - 1} \left(\frac{\left(1 + \frac{\dot{r}^{'}}{\bar{\dot{r}}}\right)\left(1 - \frac{T_s^{'}}{(T_f - \bar{T}_s)}\right)}{\frac{\xi^* - 1}{\bar{\xi}^* - 1}} - 1 \right) \end{aligned} \tag{A.18}$$

$$\begin{aligned} \rho_p \bar{\dot{r}} c_p (\bar{T}_s - T_0)(A_c \epsilon_T \sin(2\pi f_s \tau + \phi_c)) &= \rho_p \bar{\dot{r}} \bar{H}_s \left(\frac{\dot{r}^{'}}{\bar{\dot{r}}} + \frac{H_s^{'}}{\bar{H}_s} \right) \\ &+ \frac{\rho_p \bar{\dot{r}} c_p (T_f - \bar{T}_s)}{\bar{\xi}^* - 1} \left(\frac{\left(1 + \frac{\dot{r}^{'}}{\bar{\dot{r}}} - \frac{T_s^{'}}{(T_f - \bar{T}_s)}\right)}{\frac{\xi^* - 1}{\bar{\xi}^* - 1}} - 1 \right) \end{aligned} \tag{A.19}$$

Linearized form of non dimensional flame stand-off distance, ξ^* (Eq. A.20), only fluctuating quantity left to be linearized is obtained as follow,

$$\xi^* = exp\left(\frac{\rho_p \dot{r} c_p}{k_g}\right) \tag{A.20}$$

Using mass balance at propellant surface,

$$\rho_p \dot{r} = k_r p^2 x^*$$

$$\xi^* = exp\left(\frac{(\rho_p \dot{r})^2 c_p}{k_g k_r p^2}\right) \tag{A.21}$$

Dividing Eq. A.21 by $\bar{\xi}^*$ and using linearized form fluctuating quantities,

$$\begin{aligned}
\frac{\xi^*}{\bar{\xi}^*} &= exp\left(\frac{\rho_p^2(\bar{\dot{r}} + \dot{r}^{'})^2 c_p}{k_g k_r(\bar{p} + p^{'})^2} - \frac{\rho_p^2 \bar{\dot{r}}^2 c_p}{k_g k +_r \bar{p}^2}\right) \\
&= exp\left(\frac{\rho_p^2 \bar{\dot{r}}^2 c_p (1 + \frac{\dot{r}^{'}}{\bar{\dot{r}}})^2}{k_g k_r \bar{p}^2 (1 + \frac{p^{'}}{\bar{p}})^2} - \frac{\rho_p^2 \bar{\dot{r}}^2 c_p}{k_g k_r \bar{p}^2}\right) \\
&= exp\left(\frac{\rho_p^2 \bar{\dot{r}}^2 c_p}{k_g k_r \bar{p}^2}\left(\left(1 + 2\frac{\dot{r}^{'}}{\bar{\dot{r}}}\right)\left(1 - 2\frac{p^{'}}{\bar{p}}\right) - 1\right)\right) \\
&= exp\left(ln\bar{\xi}^*\left(2\frac{\dot{r}^{'}}{\bar{\dot{r}}} - 2\frac{p^{'}}{\bar{p}}\right)\right) \\
&= 1 + ln\bar{\xi}^*\left(2\frac{\dot{r}^{'}}{\bar{\dot{r}}} - 2\frac{p^{'}}{\bar{p}}\right)
\end{aligned} \tag{A.22}$$

Using $\bar{\xi}^* = 1 + B$, $B = \frac{T_f - \bar{T}_s}{\bar{T}_s - T_o - \bar{H}_s/c_p}$, $\xi^* - 1$ can be expressed as,

$$\begin{aligned}
\xi^* - 1 &= \bar{\xi}^* \frac{\xi^*}{\bar{\xi}^*} - 1 \\
&= (1 + B) + (1 + B) ln(1 + B)\left(2\frac{\dot{r}^{'}}{\bar{\dot{r}}} - 2\frac{p^{'}}{\bar{p}}\right) - 1 \\
&= B + (1 + B) ln(1 + B)\left(2\frac{\dot{r}^{'}}{\bar{\dot{r}}} - 2\frac{p^{'}}{\bar{p}}\right)
\end{aligned} \tag{A.23}$$

Substituting Eq. A.23 in Eq. A.19,

$$\begin{aligned}
\rho_p \bar{\dot{r}} c_p (\bar{T}_s - T_0)(A_c \epsilon_T \sin(2\pi f_s \tau + \phi_c)) &= \rho_p \bar{\dot{r}} \bar{H}_s \left(\frac{\dot{r}^{'}}{\bar{\dot{r}}} + \frac{H_s^{'}}{\bar{H}_s}\right) \\
&+ \frac{\rho_p \bar{\dot{r}} c_p (T_f - \bar{T}_s)}{\bar{\xi}^* - 1}\left(\frac{\left(1 + \frac{\dot{r}^{'}}{\bar{\dot{r}}} - \frac{T_s^{'}}{(T_f - \bar{T}_s)}\right) B}{B + (1 + B) ln(1 + B)\left(2\frac{\dot{r}^{'}}{\bar{\dot{r}}} - 2\frac{p^{'}}{\bar{p}}\right)} - 1\right)
\end{aligned} \tag{A.24}$$

$$\begin{aligned}
\rho_p \bar{\dot{r}} c_p (\bar{T}_s - T_0)(A_c \epsilon_T \sin(2\pi f_s \tau + \phi_c)) &= \rho_p \bar{\dot{r}} \bar{H}_s \left(\frac{\dot{r}^{'}}{\bar{\dot{r}}} + \frac{H_s^{'}}{\bar{H}_s}\right) \\
&+ \frac{\rho_p \bar{\dot{r}} c_p (T_f - \bar{T}_s)}{B}\left(\frac{\dot{r}^{'}}{\bar{\dot{r}}} - \frac{T_s^{'}}{(T_f - \bar{T}_s)} - \frac{(1 + B) ln(1 + B)}{B}\left(2\frac{\dot{r}^{'}}{\bar{\dot{r}}} - 2\frac{p^{'}}{\bar{p}}\right)\right)
\end{aligned} \tag{A.25}$$

$$\rho_p\bar{\dot{r}}c_p(\bar{T}_s - T_0)(A_c\epsilon_T \sin(2\pi f_s\tau + \phi_c)) = \rho_p\bar{\dot{r}}\bar{H}_s\left(\frac{\dot{r}^{'}}{\bar{\dot{r}}} + \frac{H_s^{'}}{\bar{H}_s}\right)$$
$$+ \rho_p\bar{\dot{r}}(c_p(\bar{T}_s - T_o) - \bar{H}_s)\left(\frac{\dot{r}^{'}}{\bar{\dot{r}}} - \frac{T_s^{'}}{(T_f - \bar{T}_s)} - \frac{(1+B)ln(1+B)}{B}\left(2\frac{\dot{r}^{'}}{\bar{\dot{r}}} - 2\frac{p^{'}}{\bar{p}}\right)\right)$$

(A.26)

$$\rho_p\bar{\dot{r}}c_p(\bar{T}_s - T_0)(A_c\epsilon_T \sin(2\pi f_s\tau + \phi_c)) = \rho_p\bar{\dot{r}}\bar{H}_s\left(\frac{\dot{r}^{'}}{\bar{\dot{r}}} + \frac{H_s^{'}}{\bar{H}_s}\right)$$
$$+ \rho_p\bar{\dot{r}}(c_p(\bar{T}_s - T_o) - \bar{H}_s)\left(\frac{\dot{r}^{'}}{\bar{\dot{r}}} - \frac{T_s^{'}}{(T_f - \bar{T}_s)} - \frac{(1+B)ln(1+B)}{B}\left(2\frac{\dot{r}^{'}}{\bar{\dot{r}}} - 2\frac{p^{'}}{\bar{p}}\right)\right)$$

(A.27)

$$\frac{1}{1-h_s}(A_c\epsilon_T \sin(2\pi f_s\tau + \phi_c)) = \frac{h_s}{1-h_s}\left(\frac{\dot{r}^{'}}{\bar{\dot{r}}} + \frac{H_s^{'}}{\bar{H}_s}\right)$$
$$+ \frac{\dot{r}^{'}}{\bar{\dot{r}}} - \frac{T_s^{'}}{(T_f - \bar{T}_s)} - \frac{(1+B)ln(1+B)}{B}\left(2\frac{\dot{r}^{'}}{\bar{\dot{r}}} - 2\frac{p^{'}}{\bar{p}}\right)$$

(A.28)

Perturbation of Arrhenius law gives fluctuations in surface temperature as,

$$\begin{aligned}\epsilon_T &= \frac{T_s^{'}}{\bar{T}_s} \\ &= \frac{1}{e_s}\frac{\dot{r}^{'}}{\bar{\dot{r}}}\end{aligned} \tag{A.29}$$

where,

$$e_s = \frac{-E_s}{R\bar{T}_s}$$

.

Perturbation of enthalpy of decomposition AP which is a function of pressure, $H_s = 0.6p + 448.65$ gives,

$$\frac{H_s^{'}}{\bar{H}_s} = \frac{0.6\bar{p}}{\bar{H}_s}\frac{p^{'}}{\bar{p}} \tag{A.30}$$

Substituting Eq. A.29 and Eq. A.30 in Eq. A.28 and rearranging terms,

$$\left[\frac{1}{1-h_s}\frac{A_c}{e_s}\sin(2\pi f_s\tau+\phi_c)-\frac{h_s}{1-h_s}+2g(B)+\frac{1}{e_s}\theta_{fs}-1\right]\frac{\dot{r}'}{\bar{\dot{r}}}=\left[2g(B)+\frac{h_s}{(1-h_s)}\frac{0.6\bar{p}}{\bar{H}_s}\right]\frac{p'}{\bar{p}} \tag{A.31}$$

In Eq. A.31,

$$g(B)=\frac{(1+B)ln(1+B)}{B}, \theta_s=\frac{\bar{T}_s}{T_f-\bar{T}_s}$$

From Eq. A.31, Pressure coupled frequency response, R_p is obtained as,

$$R_p=\frac{2+h_s/(1-h_s)(0.6\bar{p})/\bar{H}_s(1/g(B))}{2+(\theta_{fs}(1-h_s)+A_c\cos\phi_c-e_s)/(g(B)(1-h_s)e_s)} \tag{A.32}$$

A.3 Perturbation analysis of binder coated AP particle burn rate equations

Surface heat balance equation for binder-matrix coated AP particle is given by Eq. A.33,

$$\rho_p\bar{\dot{r}}_i c_p(\bar{T}_s-T_0)(1+A_c\epsilon_T\sin(2\pi f_s\tau+\phi_c))=\rho_p\dot{r}_i H_s+\frac{\rho_p\dot{r}_i c_p(T_{eff}-T_s)g_f}{\xi^*_{eff}-1} \tag{A.33}$$

Under steady conditions, Eq. A.33 takes the form given in Eq. A.34.

$$\rho_p\bar{\dot{r}}_i c_p(\bar{T}_s-T_0)=\rho_p\bar{\dot{r}}_i\bar{H}_s+\frac{\rho_p\bar{\dot{r}}_i c_p(\bar{T}_{eff}-\bar{T}_s)g_f}{\bar{\xi}^*_{eff}-1} \tag{A.34}$$

Subtracting Eq. A.34 from Eq. A.33 and using linearized form of fluctuating quantities,

$$\begin{aligned}\rho_p\bar{\dot{r}}_i c_p(\bar{T}_s-T_0)(A_c\epsilon_T\sin(2\pi f_s\tau+\phi_c))&=\rho_p(\bar{H}_s\dot{r}_i'+\bar{\dot{r}}_i H_s')\\&+\frac{\rho_p\bar{\dot{r}}_i c_p(\bar{T}_{eff}-\bar{T}_s)g_f}{\bar{\xi}^*_{eff}-1}\left(\frac{\left(1+\frac{\dot{r}_i'}{\bar{\dot{r}}_i}\right)\left(1+\frac{T'_{eff}}{(\bar{T}_{eff}-\bar{T}_s)}-\frac{T'_s}{(\bar{T}_{eff}-\bar{T}_s)}\right)}{\frac{\xi^*_{eff}-1}{\bar{\xi}^*_{eff}-1}}-1\right)\end{aligned} \tag{A.35}$$

$$\rho_p \bar{\dot{r}}_i c_p (\bar{T}_s - T_0)(A_c \epsilon_T \sin(2\pi f_s \tau + \phi_c)) = \rho_p \bar{\dot{r}}_i \bar{H}_s \left(\frac{\dot{r}_i^{'}}{\bar{\dot{r}}_i} + \frac{H_s^{'}}{\bar{H}_s} \right) + \frac{\rho_p \bar{\dot{r}}_i c_p (\bar{T}_{eff} - \bar{T}_s) g_f}{\bar{\xi}_{eff}^* - 1} \left(\frac{\left(1 + \frac{\dot{r}_i^{'}}{\bar{\dot{r}}_i} + \frac{T_{eff}^{'}}{(\bar{T}_{eff} - \bar{T}_s)} - \frac{T_s^{'}}{(T_f - \bar{T}_s)} \right)}{\frac{\xi_{eff}^* - 1}{\xi_{eff}^* - 1}} - 1 \right) \tag{A.36}$$

Effective temperature, T_{eff} is defined by,

$$\frac{T_{eff} - 1250}{T_{f,ad} - 1250} = \frac{1 - e^{-z}}{z}; \quad z = \frac{d_{AP}}{d_o} \tag{A.37}$$

where d_o is diffusion distance defined as,

$$d_0 = d_{0,ref}(1 - \phi) \left(\frac{20}{p} \right) \sqrt{\frac{30000}{K_r}} \tag{A.38}$$

Description of all the terms is given in section 2.3 Linearized form of effective flame temperature (T_{eff}) is obtained as follow,

$$\begin{aligned} \frac{T_{eff}^{'}}{\bar{T}_{eff}} &= \frac{T_{eff} - \bar{T}_{eff}}{\bar{T}_{eff}} \\ &= \frac{(T_{f,ad} - 1250)}{\bar{T}_{eff}} \left(\frac{1 - e^{-z}}{z} - \frac{1 - e^{-\bar{z}}}{\bar{z}} \right) \\ &= \frac{(T_{f,ad} - 1250)}{\bar{T}_{eff}} \left(\frac{1 - e^{-(\bar{z} + z^{'})}}{(\bar{z} + z^{'})} - \frac{1 - e^{-\bar{z}}}{\bar{z}} \right) \\ &= \frac{(T_{f,ad} - 1250)}{\bar{T}_{eff}} \left(\frac{1 - e^{-\bar{z}} e^{-z^{'}}}{\bar{z}(1 + \frac{z^{'}}{\bar{z}})} - \frac{1 - e^{-\bar{z}}}{\bar{z}} \right) \\ &= \frac{(T_{f,ad} - 1250)}{\bar{T}_{eff}} \frac{1 - e^{-\bar{z}}(1 - z^{'})}{\bar{z}} \left(1 - \frac{z^{'}}{\bar{z}} \right) - \frac{1 - e^{-\bar{z}}}{\bar{z}} \\ &= \frac{z^{'}}{\bar{z}} \left(\frac{e^{-\bar{z}}(1 + \bar{z}) - 1}{\bar{z}} \right) \end{aligned} \tag{A.39}$$

In Eq. A.39 $z^{'}$ is obtained by linearizing $z = \frac{d_{AP}}{d_0}$ and using the definition of d_0 given in Eq. A.38,

$$\begin{aligned}
\frac{z^{'}}{\bar{z}} &= \frac{d_{AP}\left(\frac{1}{d_0} - \frac{1}{\bar{d}_0}\right)}{\frac{d_{AP}}{d_0}} \\
&= \frac{(\bar{d}_0 - d_0)}{d_0} \\
&= -(1 - \frac{\bar{d}_0}{d_0}) \\
&= -(1 - \frac{1}{(1 + \frac{d_0^{'}}{\bar{d}_0})}) \\
&= -\frac{d_0^{'}}{\bar{d}_0} \\
&= -\frac{d_0 - \bar{d}_0}{\bar{d}_0} \\
&= -d_{ref}\sqrt{\frac{30000}{K_r}}(1-\phi)20\left(\frac{1}{p} - \frac{1}{\bar{p}}\right)\frac{1}{\bar{d}_0} \\
&= -d_{ref}\sqrt{\frac{30000}{K_r}}(1-\phi)20\left(\frac{1}{\bar{p} + p^{'}} - \frac{1}{\bar{p}}\right)\frac{1}{\bar{d}_0} \\
&= -d_{ref}\sqrt{\frac{30000}{K_r}}(1-\phi)\frac{20}{\bar{p}}\left(\frac{1}{1 + \frac{p^{'}}{\bar{p}}} - 1\right)\frac{1}{\bar{d}_0} \\
&= d_{ref}\sqrt{\frac{30000}{K_r}}(1-\phi)\frac{20}{\bar{p}}\left(\frac{p^{'}}{\bar{p}}\right) \\
&= \frac{\bar{d}_0 - 2t_{bm}}{\bar{d}_0}\frac{p^{'}}{\bar{p}}
\end{aligned} \tag{A.40}$$

Using Eq. A.39, Eq. A.40 is expressed as,

$$\frac{T_{eff}^{'}}{\bar{T}_{eff}} = z_r\frac{p^{'}}{\bar{p}} \tag{A.41}$$

where, z_r is,

$$z_r = \frac{\bar{d}_0 - 2t_{bm}}{\bar{d}_0}\left(\frac{e^{-\bar{z}}(1+\bar{z}) - 1}{\bar{z}}\right)$$

Effective flame stand-off (ξ_{eff}^{*}) distance given by,

$$\xi_{eff}^{*} = exp\left[\frac{\rho_p^2\dot{r}^2c_p}{k_gK_{r,eff}p^2}\right]; \quad K_{r,eff} = A_g exp\left[-\frac{E_g}{RT_{eff}}\right] \tag{A.42}$$

ξ^*_{eff} is linearized as,

$$\begin{aligned}
\frac{\xi^*_{eff}}{\bar{\xi}^*_{eff}} &= exp\left(\frac{\rho^2\dot{r}_i^2 c_p}{k_g K_{r,eff} p^2} - \frac{\rho^2\bar{\dot{r}}_i^2 c_p}{k_g \bar{k}_{r,eff}\bar{p}^2}\right) \\
&= exp\left(\frac{\rho^2(\bar{\dot{r}}_i + \dot{r}_i^{'})^2 c_p}{k_g(\bar{k}_{r,eff} + K^{'}_{r,eff})p^2} - \frac{\rho^2\bar{\dot{r}}_i^2 c_p}{k_g\bar{k}_{r,eff}\bar{p}^2}\right) \\
&= exp\left(\frac{\rho_p^2\bar{\dot{r}}_i^2 c_p(1+\frac{\dot{r}_i^{'}}{\bar{\dot{r}}_i})^2}{k_g\bar{k}_{r,eff}(1+\frac{K^{'}_{r,eff}}{\bar{k}_{r,eff}})\bar{p}^2(1+\frac{p^{'}}{\bar{p}})^2} - \frac{\rho_p^2\bar{\dot{r}}_i^2 c_p}{k_g\bar{k}_{r,eff}\bar{p}^2}\right) \\
&= exp\left(\frac{\rho_p^2\bar{\dot{r}}_i^2 c_p}{k_g\bar{k}_{r,eff}\bar{p}^2}\left(\left(1+2\frac{\dot{r}_i^{'}}{\bar{\dot{r}}_i}\right)\left(1-2\frac{p^{'}}{\bar{p}}\right)\left(1-\frac{K^{'}_{r,eff}}{\bar{k}_{r,eff}}\right)-1\right)\right) \\
&= exp\left(ln\bar{\xi}^*_{eff}\left(2\frac{\dot{r}_i^{'}}{\bar{\dot{r}}_i} - 2\frac{p^{'}}{\bar{p}} - \frac{K^{'}_{r,eff}}{\bar{k}_{r,eff}}\right)\right) \\
&= 1 + ln\bar{\xi}^*_{eff}\left(2\frac{\dot{r}_i^{'}}{\bar{\dot{r}}_i} - 2\frac{p^{'}}{\bar{p}} - \frac{K^{'}_{r,eff}}{\bar{k}_{r,eff}}\right)
\end{aligned} \tag{A.43}$$

Using expression for gas phase reaction rate, $K_{r,eff}$ from Eq. A.42 and linearizing it using Eq. A.39,

$$\frac{\xi^*_{eff}}{\bar{\xi}^*_{eff}} = 1 + ln\bar{\xi}^*_{eff}\left(2\frac{\dot{r}_i^{'}}{\bar{\dot{r}}_i} - 2\frac{p^{'}}{\bar{p}} - e_g z_r\frac{p^{'}}{\bar{p}}\right) \tag{A.44}$$

Using $\bar{\xi}^*_{eff} = 1 + B_{eff}$, $B_{eff} = \frac{\bar{T}_{eff}-\bar{T}_s}{\bar{T}_s - T_o - \bar{H}_s/c_p}$, $\xi^*_{eff} - 1$ can be expressed as,

$$\begin{aligned}
\xi^*_{eff} - 1 &= \bar{\xi}^*_{eff}\frac{\xi^*_{eff}}{\bar{\xi}^*_{eff}} - 1 \\
&= (1+B_{eff}) + (1+B_{eff})ln(1+B_{eff})\left(2\frac{\dot{r}_i^{'}}{\bar{\dot{r}}_i} - 2\frac{p^{'}}{\bar{p}} - e_g z_r\frac{p^{'}}{\bar{p}}\right) - 1 \\
&= B_{eff} + (1+B_{eff})ln(1+B_{eff})\left(2\frac{\dot{r}_i^{'}}{\bar{\dot{r}}_i} - 2\frac{p^{'}}{\bar{p}} - e_g z_r\frac{p^{'}}{\bar{p}}\right)
\end{aligned} \tag{A.45}$$

Substituting Eq. A.29,Eq. A.39 and Eq. A.45 in Eq. A.36,

$$\rho_p\bar{\dot{r}}_i c_p(\bar{T}_s - T_0)(A_c\epsilon_T \sin(2\pi f_s\tau + \phi_c)) = \rho_p\bar{\dot{r}}_i\bar{H}_s\left(\frac{\dot{r}_i^{'}}{\bar{\dot{r}}_i} + \frac{H_s^{'}}{\bar{H}_s}\right)$$
$$+\frac{\rho_p\bar{\dot{r}}_i c_p(\bar{T}_{eff} - \bar{T}_s)g_f}{\bar{\xi}^*_{eff} - 1}\left(\frac{\left(1 + \frac{\dot{r}_i^{'}}{\dot{r}_i} + \frac{\bar{T}_{eff}}{(\bar{T}_{eff}-\bar{T}_s)}z_r\frac{p^{'}}{\bar{p}} - \frac{\bar{T}_s}{(T_f-\bar{T}_s)}\frac{1}{e_s}\frac{\dot{r}_i^{'}}{\dot{r}_i}\right)}{\frac{1}{B_{eff}}\left(B_{eff} + (1+B_{eff})ln(1+B_{eff})\left(2\frac{\dot{r}_i^{'}}{\dot{r}_i} - 2\frac{p^{'}}{\bar{p}} - e_g z_r\frac{p^{'}}{\bar{p}}\right)\right)} - 1\right)$$

(A.46)

$$\rho_p\bar{\dot{r}}_i c_p(\bar{T}_s - T_0)(A_c\epsilon_T \sin(2\pi f_s\tau + \phi_c)) = \rho_p\bar{\dot{r}}_i\bar{H}_s\left(\frac{\dot{r}_i^{'}}{\bar{\dot{r}}_i} + \frac{H_s^{'}}{\bar{H}_s}\right) + \frac{\rho_p\bar{\dot{r}}_i c_p(\bar{T}_{eff} - \bar{T}_s)g_f}{B_{eff}}$$
$$\left(\frac{\dot{r}_i^{'}}{\bar{\dot{r}}_i} + \frac{\bar{T}_{eff}}{(\bar{T}_{eff} - \bar{T}_s)}z_r\frac{p^{'}}{\bar{p}} - \frac{\bar{T}_s}{(T_f - \bar{T}_s)}\frac{1}{e_s}\frac{\dot{r}_i^{'}}{\bar{\dot{r}}_i} - \frac{(1+B_{eff})ln(1+B_{eff})}{B_{eff}}\left(2\frac{\dot{r}_i^{'}}{\bar{\dot{r}}_i} - 2\frac{p^{'}}{\bar{p}} - e_g z_r\frac{p^{'}}{\bar{p}}\right)\right)$$

(A.47)

Linearized form of enthalpy of decomposition of AP/HTPB remains same as Eq. A.30 since there is negligible change in enthalpy of decomposition of HTPB with respect to pressure. Using linearized form of H_s and rearranging terms in Eq. A.47, frequency response for binder-matrix coated AP particle ($R_{p,i}$) is obtained as,

$$R_{p,i} = \frac{2 + h_s/(1-h_s)(0.6f_{AP}\bar{p})/(g_f\bar{H}_s)(1/g(B_{eff})) + z_r[e_g + (1/g(B_{eff}))\bar{T}_{eff}/(\bar{T}_{eff} - \bar{T}_s)]}{2 + (g_f\theta_{fs,eff}(1-h_s) + A_c cos(\phi_c) - e_s h_s - g_f e_s(1-h_s))/(g_f g(B_{eff})(1-h_s)e_s)}$$

(A.48)

REFERENCES

1. **Arvind, I.**, **S. Varunkumar**, and **H. S. Mukunda** (2013). Progress on solid propellant combustion instability studies at IISc. Technical report, Indian Institute of Science, Bangalore.

2. **Baum, J. D.** and **J. N. Levine** (1986). Modeling of nonlinear longitudinal instability in solid rocket motors. *Acta Astronautica*, **13**(6-7), 339–348.

3. **Beckstead, M.**, **T. Boggs**, and **R. Derr** (1970). Surface structure of ammonium perchlorate composite propellants. *AIAA Journal*, **8**(2), 370–372.

4. **Beckstead, M. W.**, **R. L. Derr**, and **C. F. Price** (1971). The combustion of solid monopropellants and composite propellants. *Symposium (International) on Combustion*, **13**, 1047–1056. ISSN 00820784.

5. **Beckstead, M. W.**, **K. Meredith**, and **F. S. Blomshield** (2002). Examples of unsteady combustion in non-metallized propellants. *International Journal of Energetic Materials and Chemical Propulsion*, **5**(1-6).

6. **Blomshield, F. S.** (2001). Historical perspective of combustion instability in motors: case studies. *AIAA Paper*, **3875**, 2001.

7. **Blomshield, F. S.**, *Lessons learned in solid rocket combustion instability*. Defense Technical Information Center, 2006.

8. **Blomshield, F. S.**, **C. Bicker**, and **R. A. Stalnaker**, High pressure pulsed motor firing combustion instability investigations. *In 1997 AIAA Joint Propulsion Meeting, Paper*, 97-3253. 1997.

9. **Boggs, T.**, **D. Zurn**, **H. Cordes**, and **J. Covino** (1988). Combustion of ammonium perchlorate and various inorganic additives. *Journal of Propulsion and Power*, **4**(1), 27–40.

10. **Buckmaster, J.**, **T. Jackson**, **L. Massa**, and **M. Ulrich** (2005). Response of a burning heterogeneous propellant to small pressure disturbances. *Proceedings of the Combustion Institute*, **30**(2), 2079–2086.

11. **Chakravarthy, S.**, **E. Price**, and **R. Sigman**, Binder melt flow effects in the combustion of ap-hc composite solid propellants. *In 31st Joint Propulsion Conference and Exhibit*. 1995.

12. **Cheng, S.-I.**, Unstable combustion in solid-propellant rocket motors. *In Symposium (International) on Combustion*, volume 8. Elsevier, 1961.

13. **Cohen, N. S.** (1980). Review of composite propellant burn rate modeling. *AIAA Journal*, **18**(3), 277–293.

14. **Crump, J.** (1977). Combustion instability in minimum smoke propellants, part 1. experimental techniques and results. *Naval Weapons Center*.

15. **Culick, F.** (1968). A review of calculations for unsteady burning of a solid propellant. *AIAA Journal*, **6**(12), 2241–2255.

16. **De Luca, L.** and **M. Summerfield**, *Nonsteady burning and combustion stability of solid propellants*, volume 143. AIAA, 1992.

17. **Finlinson, J.**, **R. Stalnaker**, and **F. Blomshield**, Ultra pure ammonium perchlorate T-burner pressure coupled response at 500, 1000 and 1800 psi. Joint Propulsion Conferences. American Institute of Aeronautics and Astronautics, 1998.

18. **Flandro, G. A.**, **S. R. Fischbach**, and **J. Majdalani** (2007). Nonlinear rocket motor stability prediction: Limit amplitude, triggering, and mean pressure shifta). *Physics of Fluids (1994-present)*, **19**(9), 094101.

19. **Flandro, G. A.** and **E. Jacob**, Irregular burning: on the origin of the dc shift. *In 43rd Joint Propulsion Conference*. 2007.

20. **Fredrick Jr, R. A.** (1988). Combustion Mechanisms of Wide Distribution Propellants. Technical Report AFAL-TR-88-008, DTIC Document.

21. **Glick, R. L.** (1974). On statistical analysis of composite solid propellant combustion. *AIAA Journal*, **12**(3), 384–385.

22. **Grad, H.** (1949). Resonance burning in rocket motors. *Communications on Pure and Applied Mathematics*, **2**(1), 79–102.

23. **Gross, M. L.** and **M. W. Beckstead** (2010). Diffusion flame calculations for composite propellants predicting particle-size effects. *Combustion and Flame*, **157**, 864–873. ISSN 00102180.

24. **Guéry, J.-F.** (2004). Numerical modeling of internal flow aerodynamics. part 2: Unsteady flows. Technical report, SNPE CENTRE DE RECHERCHES DU BOUCHET VERT-LE-PETIT FRANCE.

25. **Hafenrichter, T. J.**, **J. J. Murphy**, and **H. Krier** (2004). Ultrasonic measurement of the pressure-coupled response function for composite solid propellants. *Journal of propulsion and power*, **20**(1), 110–119.

26. **Handley, J. C.** (1976). *An experimental investigation of catalysis in the combustion of composite solid propellants*. Ph.D. thesis.

27. **Ibiricu, M.** (1969). Experimental studies on the oscillatory combustion of solid propellants. *Naval Weapons Center*.

28. **Ishitha, K.** and **P. Ramakrishna** (2014). Studies on the role of iron oxide and copper chromite in solid propellant combustion. *Combustion and Flame*, **161**(10), 2717–2728.

29. **Jackson, T.** and **J. Buckmaster** (2002). Heterogeneous propellant combustion. *AIAA journal*, **40**(6), 1122–1130.

30. **Li, S.** and **D. Zhao** (2013). Heat flux and acoustic power in a convection-driven t-shaped thermoacoustic system. *Energy conversion and management*, **75**, 336–347.

31. **Malhotra, S.**, **G. Flandro**, **S. Malhotra**, and **G. Flandro** (1997). On the origin of the dc shift. *AIAA paper*, (97-3249).

32. **Miller, R. R.** (1982). Effects of particle size on reduced smoke propellant ballistics. *AIAA paper*, **1096**.

33. **Murphy, J. J.** and **H. Krier**, Linear pressure coupled frequency response of heterogeneous solid propellants. *In Symposium (International) on Combustion*, volume 27. Elsevier, 1998.

34. **Novozhilov, B. V.** (1973). Nonstationary combustion of solid rocket fuels. Technical Report FTD-MT-24-317-74, DTIC Document.

35. **Perry, E. H.** (1970). *Investigations of the T-burner and its role in combustion instability studies*. Ph.D. thesis, California Institute of Technology.

36. **Shusser, M.**, **F. E. C. Culick**, and **N. S. Cohen** (2008). Analytical solution for pressure-coupled combustion response functions of composite solid propellants. *Journal of Propulsion and Power*, **24**(5), 1058–1067.

37. **Spurling, J.**, **F. Blomshield**, and **D. Pate**, Effects of temperature conditioned environment on a propellant's pressure-coupled response. *In 46th AIAA/ASME/SAE/ASEE Joint Propulsion Conference & Exhibit*. 2010.

38. **Spurling, J. A.**, Modeling effects of initial temperatures on a propellantâĂŹs pressure-coupled response using a pseudo propellant model. *In 50th AIAA/ASME/SAE/ASEE Joint Propulsion Conference*. 2014.

39. **Strand, L. D.**, **A. L. Schultz**, and **G. K. Reedy** (1972). Determination of solid-propellant transient regression rates using a microwave doppler shift technique.

40. **Varunkumar, S.** and **H. S. Mukunda** (2013). Progress report on solid rocket combustion instability modelling. Technical Report IITRPR-SMMEE-2013-001, IISc & IIT Ropar.

41. **Varunkumar, S.** and **H. S. Mukunda** (2017). Progress report on the DRDL project on combustion instability. Technical report, Indian Institute of Science, Bangalore.

42. **Varunkumar, S.**, **M. Zaved**, and **H. S. Mukunda** (2016). A novel approach to composite propellant combustion modeling with a new heterogeneous quasi one-dimensional (hequ1-d) framework. *Combustion and Flame*.

43. **Verma, S.** and **P. Ramakrishna** (2013). Investigations on activated charcoal, a burn-rate enhancer in composite solid propellant. *Journal of Propulsion and Power*.

44. **Vuillot, F.** and **G. Casalis** (2004). Motor flow instabilities-part 1. Technical Report RTO-EN-023, ONERA-MEUDON CENTRE (FRANCE).

45. **Williams, F. A.**, *Combustion Theory: the fundamental theory of chemical reacting flow systems*. Addison-Wesley, 1965.

46. **Zaved, M.** (2017). *Steady Heterogeneous Quasi 1-D Model for AP-HTPB based Composite Propellants*. Master's thesis, Indian Institute of Technology, Madras.

47. **Zel'dovich, Y. B.** (1942). On theory of burning of the gunpowder and explosives. *J. Exper. Theoret. Phys*, **12**, 498–524.

LIST OF PAPERS BASED ON THESIS

1. Vishal Wadhai, Varunkumar S, Linear Instability and DC Shift in Tactical Missile Solid Rocket Motors - a Computational Study, *11^th Asia Pacific Conference on Combustion*, (2017).